

The Hydrodynamics of Ferrofluid Aggregates

Alicia Marie Williams

Dissertation submitted to the faculty of the Virginia Polytechnic Institute and State
University in partial fulfillment of the requirements for the degree of

Doctor of Philosophy

In

Mechanical Engineering

Pavlos P. Vlachos, Committee Chair

Francine Battaglia, Committee Member

Mark Paul, Committee Member

Mark Stremmer, Committee Member

Ishwar Puri, Committee Member

August 1, 2008

Blacksburg, VA

Keywords: Ferrofluid, Ferrohydrodynamics, Kelvin-Helmholtz, Magnetic Drug Targeting,

DPIV

The Hydrodynamics of Ferrofluid Aggregates

Alicia M. Williams

Ferrofluids are comprised of subdomain particles of magnetite or iron oxide material that can become magnetized in the presence of a magnetic field. These unique liquids are being incorporated into many new applications due to the ability to control them at a distance using magnetic fields. However, although our understanding of the dynamics of ferrofluids has evolved, many aspects of ferrohydrodynamics remain largely unexplored, especially experimentally.

This study is the first to characterize the stability and internal dynamics of accumulating or dispersing ferrofluid aggregates spanning the stable, low Reynolds number behavior to unstable, higher Reynolds numbers. The dynamics of ferrofluid aggregates are governed by the interaction between the bulk flow shear stresses acting to wash away the aggregate and magnetic body forces acting to retain them at the magnet location. This interaction results in different aggregate dynamics, including the stretching and coagulation of the aggregate to Kelvin-Helmholtz shedding from the aggregate interface as identified by focused shadowgraphs.

Using TRDPIV, the first time-resolved flow field measurements conducted in ferrofluids reveal the presence of a three-stage process by which the ferrofluid interacts with a pulsatile bulk flow. An expanded parametric study of the effect of Reynolds number, magnetic field strength, and flow unsteadiness reveals that the increased field results can result in the lifting and wash away of the aggregate by means of vortex strengthening. In pulsatile flow, different forms of the three-stage interaction occur based on magnetic field, flow rate, and Reynolds number.

ACKNOWLEDGEMENTS

I know for a fact that I would not have reached this point without the encouragement and support of many different educators at all levels of my education. As I completed my undergraduate education, Professors Michael Alley and Karen Thole played a strong role in their encouragement of my pursuit of graduate study. Moreover, they steadfastly encouraged my application to the National Science Foundation Graduate Research Fellowship, which has provided funding for me to perform research over the past three years. To my advisor, Pavlos, I have learned a lot from you over the years that we have known each other, and I appreciate your considerable effort and interest in my education as well as your encouragement in my pursuit of the doctorate. Finally, and certainly not least, I'd like to thank all the members of my committee for their helpful input at all stages of this project.

To all the graduate students that I have had the honor to work with in Aether over the years including Adric, Weiland, Andy, Dave², Kelley, John, Karri and everyone else: it's been a wild ride, and I'm going to miss all you guys. Working with all of you has been a pleasure, and each of you has taught me something along the way and you are amazing people. Come see me in California!

I would be completely remiss if I did not acknowledge others' assistance and willingness to help me, especially the ladies in the ME office. Renee Shack, Brandy McCoy, and Lisa Stables have always assisted promptly and with a smile too! A special thank you also to Cathy Hill, who can always be counted on to get me out of the latest mess with my paperwork.

Lastly, but absolutely not least, I recognize my family for their indefatigable support and willingness to help me in any way possible. To my parents, I thank you for both your patience and hospitality as I slept in your basement for the last two weeks of this work and to Dad for all the 5 AM pickups after a long night in the office. I wouldn't have been able to do it without you.

CONTENTS

List of Figures.....	viii
List of Tables.....	xv
Nomenclature.....	xvi
1 Introduction and Background.....	1
1.1 Motivation	1
1.2 Structure of this Document	2
1.3 Digital Particle Image Velocimetry Facilities	4
1.4 Focused ShadowGraph Technique	6
1.5 References.....	7
2 A Review of Ferrohydrodynamics	8
2.1 Abstract	8
2.2 Introduction.....	8
2.3 Ferrohydrodynamics.....	10
2.3.1 Fundamental Ferrofluid Flows and Properties	10
2.3.2 Surface Waves	10
2.4 Instabilities in Ferrohydrodynamics	13
2.4.1 Labyrinthine instability	13
2.4.2 Normal field instability	15
2.4.3 Rayleigh-Taylor Instability	16
2.4.4 Kelvin Helmholtz Instability in ferrofluids	19
2.5 Ferrofluid applications.....	22
2.5.1 Drug Targeting and hyperthermia.....	22

2.6	Other Ferrofluid Applications	25
2.7	Conclusions	25
2.8	References	26
3	The Dispersion of Ferrofluid Aggregates in Steady and Pulsatile Flows	32
3.1	Abstract	32
3.2	Introduction	33
3.3	Experimental Methods	34
3.4	Proper Orthogonal Decomposition of Detected Interfaces	36
3.5	Effect of the Reynolds Number on Aggregate Stability	39
3.6	Effect of Pulsatility on Aggregate Stability	43
3.7	Discussion	46
3.8	Conclusions	50
3.9	References	51
4	The Effect of Orthogonal Magnetic Fields on Ferrofluid Aggregate Dynamics	53
4.1	Abstract	53
4.2	Introduction	53
4.3	Experimental Methods	55
4.4	Proper Orthogonal Decomposition of Detected Edges	57
4.5	Effect of the Magnetic Field Strength on Aggregate Stability	59
4.6	Discussion	66
4.7	Conclusions	67
4.8	References	68
5	The Dynamics of Accumulating Ferrofluid Aggregates	70
5.1	Abstract	70
5.2	Introduction	71

5.3	Focused Shadowgraph Methods	72
5.4	Proper Orthogonal Interface Decomposition.....	75
5.5	Effect of Bulk Flow Inertia and Unsteadiness.....	77
5.6	Top Injection of Ferrofluid Streakline.....	81
5.7	Effect of Magnetic Field Gradients on Accumulation Dynamics	86
5.8	Discussion	90
5.9	Conclusions.....	92
5.10	References.....	93
6	The Three-Stage Interaction of Ferrofluid Aggregates with Pulsatile Flows.....	94
6.1	Abstract	94
6.2	Introduction.....	94
6.3	Experimental Method.....	96
6.4	Results	97
6.5	Vortex Identification.....	101
6.6	Proper Orthogonal Decomposition	105
6.7	Conclusions.....	109
6.8	References.....	109
7	Spatiotemporally-Resolved Dynamics of Dispersing Ferrofluid Aggregates	112
7.1	Abstract	112
7.2	Introduction.....	113
7.3	Experimental Procedure.....	114
7.4	Results	117
7.5	Discussion	126
7.6	Conclusions.....	131
7.7	References.....	132

8	Conclusions and Future Work	133
8.1	Summary of Results	134
8.2	Future work and research directions	135
8.3	Acknowledgments	137
8.4	References	137

LIST OF FIGURES

Figure 1.1. A schematic of the magnetic drug targeting drug therapy delivery system.	2
Figure 1.2. A typical DPIV experimental set up with a laser plane illuminating flow tracer particles.	5
Figure 1.3. Experimental setup of the focus shadowgraph work showing the halogen light source, test section, and digital camera positions.	6
Figure 2.1. The Rayleigh-Taylor instability in a steady water flow with a miscible ferrofluid streakline entering at the bottom of the channel.	18
Figure 2.2. Kelvin-Helmholtz shedding from a ferrofluid aggregate in pulsatile flow with a Reynolds number based on the average flow rate of 600 shown over one period of flow. During the highest flow rates, rolls of ferrofluid are observed shedding from the main aggregate.	21
Figure 3.1. Schematic of focused shadowgraph experiment. A high-speed digital camera imaged the side profile of the aggregate.	35
Figure 3.2. The image processing used to transform a grayscale image to a region corresponding to the instantaneous aggregate size (C) and the detected edge of the aggregate (D).	37
Figure 3.3. Shadowgraph images for three time instants of 0, 25, and 50 seconds for steady flow with a Reynolds number of 600. Kelvin-Helmholtz shedding occurs in the later part of the time series, and degrades as the aggregate begins to wash away.	40
Figure 3.4. Plot of the apparent ferrofluid aggregate size as a function of time in steady flow conditions. Rapid aggregate decay occurs for Reynolds numbers 500 and greater, driven by the shedding resulting from the K-H instability.	41
Figure 3.5. Plot of the first five modes of the aggregate for a Reynolds number of 400 in steady flow.	42

Figure 3.6. POD dimension for 99.5% energy reconstruction as a function of the Reynolds number for steady flow. 43

Figure 3.7. A sequence of images for sinusoidal pulsatile flow with an average Reynolds number of 600..... 44

Figure 3.8. Plot of the decrease in apparent ferrofluid aggregate volume as a function of time for a sinusoidal pulsatile flow. 45

Figure 3.9. POD dimension to reconstruct 99.5% of the total energy in pulsatile flow..... 46

Figure 3.10. Normalized pressure versus dimensionless time for steady flow cases with bulk flow Reynolds numbers between 100 and 1000..... 48

Figure 3.11. Normalized pressure versus dimensionless time for pulsatile flow cases with bulk flow Reynolds numbers between 100 and 1000..... 48

Figure 3.12. Exponent (left) and constant (right) plotted for Reynolds numbers 100-1000 for the normalized pressure versus T^* . The gray line indicates the results of a polynomial fit of these constants and exponents based on the bulk flow Reynolds number. 50

Figure 4.1. Schematic of focused shadowgraph experiment. A diffuse light source created a background from which to image the ferrofluid aggregate..... 56

Figure 4.2. The image processing used to transform a grayscale image to a region corresponding to the instantaneous aggregate size (C) and the detected edge of the aggregate (D). 58

Figure 4.3. Contours of magnetic field induction in the z-direction in terms of Tesla. The highest field gradients are visualized near the magnet tip at $(x,y) = (0, 0)$ 60

Figure 4.4. A comparison of the ferrofluid aggregate dispersion for three different Reynolds numbers. The transition to instability for a 0.3 Tesla magnetic field moves to 300 compared to 400 for a weaker magnetic field..... 61

Figure 4.5. Aggregate size plots for Reynolds numbers of 500 and 600 for two different field strengths..... 62

Figure 4.6. The impact of magnetic field strength for two different magnetic fields of 0.15 and 0.3 Tesla. For the stronger magnetic field, the aggregate destabilizes and K-H shedding occurs from the aggregate at a time of 25 seconds after the start of flow. K-H shedding causes a reduction in aggregate size. 63

Figure 4.7. Four snapshots illustrating the transition to vortex shedding from the aggregate interface for A) a maximum field strength of 0.15 Tesla with bulk flow $Re_{av} = 500$ and B) a maximum field strength of 0.3 Tesla with a bulk flow $Re_{av} = 400$ 64

Figure 4.8. Aggregate sizing for Reynolds numbers of 900 and 1000. Convergence of size curves indicates inertia-dominated physics for these cases. 65

Figure 4.9. POD dimension for five different Reynolds numbers under the application of a 0.3 Tesla magnetic field compared to a 0.15 Tesla magnetic field. Convergence of the dimension occurs commensurate with behavior of aggregate sizing..... 66

Figure 5.1. Schematic of focused shadowgraph experiment. A digital camera imaged the ferrofluid aggregate accumulation and subsequent dispersion. 72

Figure 5.2. Schematic of ferrofluid aggregate and relative orientations of test section and permanent magnet..... 74

Figure 5.3. The image processing used to transform a grayscale image A) to a region corresponding to the instantaneous aggregate size (B and C) and the detected edge of the aggregate (D). 75

Figure 5.4. Ferrofluid accumulation and washaway for a Reynolds number of 300 at A) 50% of total injected volume B) 100% of total injected volume and C) at the end of the data set. 77

Figure 5.5. Plot of the intensity-weighted aggregate accumulation versus normalized time for accumulation in steady flow..... 79

Figure 5.6. Normalized accumulation plotted versus normalized time with respect to total injection timespan for pulsatile flow..... 79

Figure 5.7. Plot of the maximum size attained by the aggregate taken from the temporal aggregate measurements, normalized by the maximum aggregate size. 80

Figure 5.8. Plot of the number of modes required to reconstruct 99.5% of the energy of the interface for steady and pulsatile flows when the ferrofluid is injected from the bottom on the test section. 81

Figure 5.9. Ferrofluid accumulation and washaway for top injection at a Reynolds number of 300 at A) 50% of total injected volume B) 100% of total injected volume and C) at the end of the data set. 82

Figure 5.10. Steady flow, top injection of ferrofluid aggregate. Significant accumulation only occurs for low Reynolds numbers. 83

Figure 5.11. Pulsatile flow, top injection of the ferrofluid aggregate. Pulsatility assists accumulation for higher Reynolds numbers compared to the results for steady flow. 84

Figure 5.12. Plot of the maximum size attained by the aggregate taken from the temporal aggregate measurements, normalized by the maximum aggregate size for top injection. 85

Figure 5.13. Plot of the number of modes required to reconstruct 99.5% of the energy of the interface for steady and pulsatile flow for top injected ferrofluid. 85

Figure 5.14. Effect of five different field gradients on the normalized aggregate sizes. 87

Figure 5.15. Normalized aggregate size versus normalized time for steady flow Reynolds number of 300, illustrating the effect of field gradients. 87

Figure 5.16. Effect of field gradients for a Reynolds number of 400 in steady flow. 88

Figure 5.17. Effect of field gradients for a Reynolds number of 400 in pulsatile flow. 89

Figure 5.18. Effect of field gradients on ferrofluid aggregates for a Reynolds number of 400 in pulsatile flow. 89

Figure 5.19. The normalized pressure versus the Reynolds number for all Reynolds numbers and field strengths for steady flow cases. 91

Figure 6.1. Experimental schematic for TRDPIV data acquisition. 97

Figure 6.2. Raw TRDPIV images illustrating the ferrofluid (gray material) interacting with the bulk flow, seeded with tracer particles appearing as intensely illuminated pixels..... 99

Figure 6.3. Contours of vorticity illustrating the three-stage process for $Re_{av} = 400$. The large primary vortex develops during the suction phase, or the period of lowest bulk flow. 100

Figure 6.4. Raw frames showing the three-stage interaction in response to flow pulsatility for an average Reynolds number of 600..... 100

Figure 6.5. Contours of vorticity for an average flow-based Reynolds number of 600. 101

Figure 6.6. Plot of maximum circulation versus time for Re_{av} of 400 with flow rate plotted on right hand axis. Flow and circulation are out of phase. 103

Figure 6.7. Maximum circulation (blue) overlaid with flow rate (green) for Re_{av} of 600..... 103

Figure 6.8. Snapshots showing streamtraces with vortex centers identified by red dots for the three-stage interaction for a Reynolds number of 400 with circulation..... 104

Figure 6.9. Comparison of the relative aggregate sizes for $Re_{av} = 400$ and 600 at 15 seconds after flow startup. Qualitatively, much more of the aggregate has eroded for the higher flow rate although the overall circulation phase driven by the flow rate remains similar. 105

Figure 6.10. Vorticity contours of the three highest energy modes for Re_{av} of 400 corresponding to the three-stage interaction of the aggregate and bulk flow..... 106

Figure 6.11. Phase portrait for Modes 1, 2, and 3 for Reynolds number of 400..... 108

Figure 6.12. Phase portrait for Modes 1, 2, and 3 for an average Reynolds number of 600..... 108

Figure 7.1. Schematic of the laser, optical setup, and digital camera used to acquire TRDPIV data..... 114

Figure 7.2. Schematic illustrating the relative location of the magnet and ferrofluid aggregate. 115

Figure 7.3. Raw PIV frame illustrating visible flow tracers in the bulk flow as well as the high noise region within the aggregate..... 117

Figure 7.4. Vortex shedding of 2% concentration at a Reynolds number of 500 in steady flow and the development of the Kelvin-Helmholtz instability, with post-processed vector field illustrating limited measurement capacity within aggregate. 117

Figure 7.5. Instantaneous vorticity contours overlaid with streamlines for a Reynolds number of 200 at a maximum magnetic field strength of 0.375 Tesla; detected edges corresponding to aggregate interface with bulk flow overlaid onto contours..... 120

Figure 7.6. Instantaneous vorticity contours for a Reynolds number of 300 at a maximum magnetic field strength of 0.375 Tesla..... 121

Figure 7.7. Instantaneous vorticity contours for a Reynolds number of 400 at a maximum magnetic field strength of 0.375 Tesla..... 122

Figure 7.8. Instantaneous pulsatile flow velocity contours illustrating the aggregate behavior for a Reynolds number of 200 at 0.375 Tesla maximum field strength. 123

Figure 7.9. Instantaneous velocity contours for pulsatile flow with an average Reynolds number of 300 with a maximum field strength of 0.375 Tesla..... 124

Figure 7.10. Instantaneous frames illustrating flow behavior for a pulsatile flow with an average Reynolds number of 400 with a maximum magnetic field of 0.375 Tesla..... 125

Figure 7.11. Instantaneous vorticity contours illustrating flow behavior for pulsatile flow an average Reynolds number of 200 with a maximum magnetic field of 0.15 Tesla. 126

Figure 7.12. Shear velocity normalized with respect to the average freestream velocity for steady flows with a Reynolds number of 300. 128

Figure 7.13. Shear velocity normalized with respect to the average freestream velocity for pulsatile flows with an average Reynolds number of 300. 128

Figure 7.14. Normalized circulation versus time, t , for three magnetic field strengths retaining an aggregate in steady bulk flow with a Reynolds number of 300. 130

Figure 7.15. Normalized circulation versus time, t , for three magnetic field strengths retaining an aggregate in pulsatile bulk flow with Re_{av} of 300. 130

LIST OF TABLES

Table 5.1. Injection flow rates based on bulk flow inertia for all Reynolds numbers examined in experiment.	73
Table 7.1. Complete test matrix of all test cases for PIV experiment examining ferrohydrodynamics of ferrofluid aggregates across a parameter space.	116

NOMENCLATURE

α	Proper Orthogonal Decomposition projection coefficient, $f(t)$
Δ	Delta, positive for complex eigenvalues as a means to identify vortices
ϕ	Proper Orthogonal Decomposition mode amplitude, $f(x)$ or $f(x,y)$
ω	Pulsation frequency, radians per second
ν	Kinematic viscosity of water, m^2/s
λ	Eigenvalue of characteristic equation of interface
Γ_{max}	Maximum circulation calculated by comparing the strength of detected vortices at each snapshot, normalized by kinematic viscosity
μ	Magnetic permeability
ν	Kinematic viscosity of water, m^2/s
a_t/a_i	Ratio of apparent size at a time instance to initial apparent aggregate size
a_i	initial apparent aggregate size, corrected for aggregate intensity
a_{tmax}	Normalized apparent aggregate size at the time of its peak size
B	Magnetic field induction, Tesla
B_{max}	Maximum magnetic field strength at inside test section wall, Tesla
D	Channel diameter, 10 mm
D_h	Hydraulic diameter, 15 mm
h	Measured aggregate height, m
l_e	Entrance length needed for fully developed flow
P	Invariant of $\Delta \mathbf{u}$
Q	Invariant of $\Delta \mathbf{u}$
R	Invariant of $\Delta \mathbf{u}$
T^*	Dimensionless time
T	Period length of a pulsatile flow, s
t	Time, s
u	Velocity field for each time snapshot, $f(x,y)$
U_0	Freestream bulk flow velocity, m/s
U_s	Velocity amplified from bulk flow due to aggregate blockage, m/s
v	Component of velocity in the flow cross section in the y-direction

w	Component of velocity in the flow cross section in the z-direction
P_{norm}	Magnetic pressure, compares magnetic and dynamic pressures
Re_{av}	Reynolds number based on average flow
Wo	Womersly number, $D_h/2(\omega/\nu)^{0.5}$

1 INTRODUCTION AND BACKGROUND

1.1 MOTIVATION

Ferrofluids consist of a liquid in which particles, often nanoscale in size, are indefinitely suspended due to their surfactant coating and Brownian motion [1,2]. These particles are highly susceptible to magnetic fields becoming magnetized but remaining liquid. The development of ferrofluids has given rise to a new branch of fluid mechanics, known as ferrohydrodynamics. The field of ferrohydrodynamics spans many phenomena from ferrofluid mechanics and rheology to fluidic instabilities that may arise under appropriate conditions.

Ferrofluid instabilities have been the subject of many recent studies, which have focused on the normal field [3], labyrinthine [4], Rayleigh-Taylor [5], and Kelvin-Helmholtz [6] instabilities. However, due to experimental difficulties measuring the motion of the opaque ferrofluid, many of these studies focus purely on analytical descriptions or numerical simulations. This is particularly true of the Kelvin-Helmholtz instability, where to the author's knowledge, no experimental results have been published to date.

The impetus for undertaking this work is to address the limitation described above and contribute to the field of ferrohydrodynamics by providing insight into the mechanics of the interaction of ferrofluid aggregates with a carrying non-magnetic fluid, under steady and pulsatile flow conditions. A primary objective of this project is to experimentally analyze the development of Kelvin-Helmholtz instability in ferrofluid aggregates and describe its effect on the dispersion and accumulation process. This effort extends upon a previous work that studied the interaction of ferrofluid masses with an incident flow, wherein the periodic washaway of the ferrofluid from an aggregated mass was demonstrated at Reynolds numbers below 400 [7,8].

In addition, ferrofluids have demonstrated promise as part of a new and potentially more effective drug delivery method, known as Magnetic Drug Targeting (MDT), which capitalizes on ferrofluid particles that are functionalized with a drug. MDT involves the interactions of a ferrofluid aggregate with an incident blood flow, which haven't been adequately characterized to date. Therefore, another objective of this work is to provide a first characterization of this interaction in an *in vitro* environment.

The MDT technique has been studied extensively in clinical environments. A graphical depiction of the MDT technique for enhanced drug delivery is shown in Figure 1.1. Although for the most part, this work has been performed in animal trials, the initial results show that this technique has great promise [9]. A representative plot of results obtained in a clinical MDT experiment conducted on a tumor that was located in a rabbit limb is shown in Figure 7 from the original journal publication in the Journal of Magnetism and Magnetic Materials. After only a single hour of treatment, a remission of the tumor was observed between 18 and 54 days later.

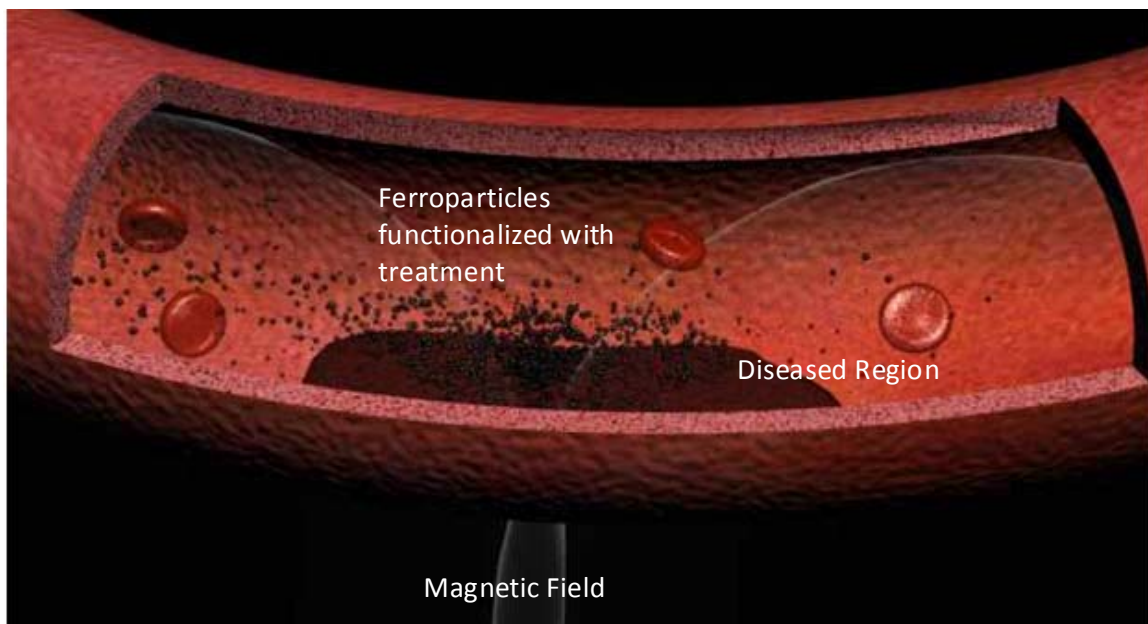


Figure 1.1. A schematic of the magnetic drug targeting drug therapy delivery system.

The present work presents studies the dynamics associated with accumulating or dispersing ferrofluid aggregates under the influence of a permanent magnet as well as how the aggregate stability affects accumulation and dispersion. The experiments and associated analysis will contribute to an improved understanding of the mechanics of ferrofluid aggregates. The results of this work may also aid in the development of improved drug delivery systems.

1.2 STRUCTURE OF THIS DOCUMENT

This document presents the complete studies conducted under the scope of ferrofluid aggregate research. The remainder of Chapter 1 will provide details on the experimental methods used in this project. The contents of the proceeding chapters are written in journal format and are summarized below.

Chapter 2 will provide a review of the state of the art in ferrohydrodynamics. A significant amount of work has been published on relevant mechanics of ferrofluids, focusing on ferrofluids in several different types of flows, including Hele-Shaw cells and surface waves. Within the past ten years, a large volume of work on ferrofluid instabilities has been published, focusing on normal field, labyrinthine, Rayleigh Taylor, and Kelvin-Helmholtz instabilities. This review addresses both the analytical and experimental work spanning all of these topics. Also, some of the newer applications of ferrofluids are presented, which have been centered within the medical field in much of the recent research.

Chapter 3 investigates the dynamics of ferrofluid aggregate dispersion as a function of Reynolds number and flow waveform. Using focused shadowgraphs digital images were obtained and image processing algorithms were applied to obtain the spatiotemporal variation of the interface between the ferrofluid and water. This interface was further analyzed using Proper Orthogonal Decomposition to quantify the interface dynamics. The regimes of stable and unstable interfaces and the transitional range in between were determined and corresponding scaling laws and dimensional parameters were developed.

Chapter 4 presents focused shadowgraph data of the dispersing ferrofluid aggregate with the objective of exploring the effect of normally oriented magnetic fields on ferrofluid aggregates. The primary contribution of this chapter is the demonstration of the orthogonally-oriented magnetic field as a destabilizing mechanism for ferrofluid aggregates. This effect is further revealed to be determined by the relative shearing flow as predicted by Kelvin-Helmholtz instability theory.

Chapter 5 extends the objectives of the preceding two chapters accumulating aggregates. The aggregate size and interface was measured using a combination of the focused shadowgraph technique as well as digital image post-processing. Using this information, more extensive observations about the effect of magnetic field gradients are made as well as the impact of different injection types on aggregate accumulation and retention. The contributions of this chapter are the identification of both pulsatility as well as magnetic field strength as

having dual impacts on the ferrofluid build up and retention based on the experimental parameters.

Chapter 6 presents the results of an initial Time Resolved Particle Image Velocimetry (TRDPIV) experiment studying the dynamics of ferrofluid aggregates in pulsatile flow for one magnetic field gradient. The contribution of this chapter is the identification of a three-stage interaction between the ferrofluid aggregate and bulk flow. This interaction is revealed from the post-processed vorticities, vortex identification, and Proper Orthogonal Decomposition.

Chapter 7 provides TRDPIV measurements of an experiment in which the objective was to study the mechanisms behind aggregate destabilization. Ferrofluid aggregate dynamics were examined over a parameter space that included steady and pulsatile flows and five different magnetic field strengths for three different Reynolds numbers. This chapter examines the interaction of the flow structures with the ferrofluid aggregate by combining the flow measurements with the detected aggregate interface locations. The primary contribution of this chapter is the identification of vortex strengthening as a precursor to the destabilization and subsequent wash away of ferrofluid aggregates.

Chapter 8 summarizes the overall conclusions developed from the experimental data obtained towards the study of ferrofluid aggregates. The conclusions from this project also provide a basis for many additional investigations, which will be outlined in detail and will include further mechanics-based efforts as well as how these mechanics studies can be translated to applications.

1.3 DIGITAL PARTICLE IMAGE VELOCIMETRY FACILITIES

The flow structures and velocity fields for both the bulk flow and internal to the ferrofluid aggregate are of interest in order to characterize the mechanics of the interaction between them. Digital Particle Image Velocimetry (DPIV) [10,11,12] is the most efficient and established method for obtaining a large number of temporally-resolved point velocity measurements simultaneously. DPIV is a non-invasive optical flow measurement method that combines a pulsing laser synchronized with a high-speed digital camera to measure planes of

velocity vectors, with possible sampling frequencies in excess of 1 kHz capable of fully resolving the temporal variations of the flow.

The pulsing laser used in DPIV experiments is opened to a plane of 1-2 mm thickness using a cylindrical lens in the region of interest and illuminates flow tracer particles. The particles are neutrally-buoyant and are selected to follow the flow without time delay. A Complementary Metal Oxide Semiconductor (CMOS) camera images the particles in the laser plane, and is synchronized with the laser pulses using a timing board. The displacement of the particles between successive frames and the pulse separation of the laser beam are used in conjunction with cross-correlation algorithms to calculate velocity vectors. An illustration of a generalized DPIV setup that can be used to spatiotemporally resolve flows is shown in Figure 1.2.

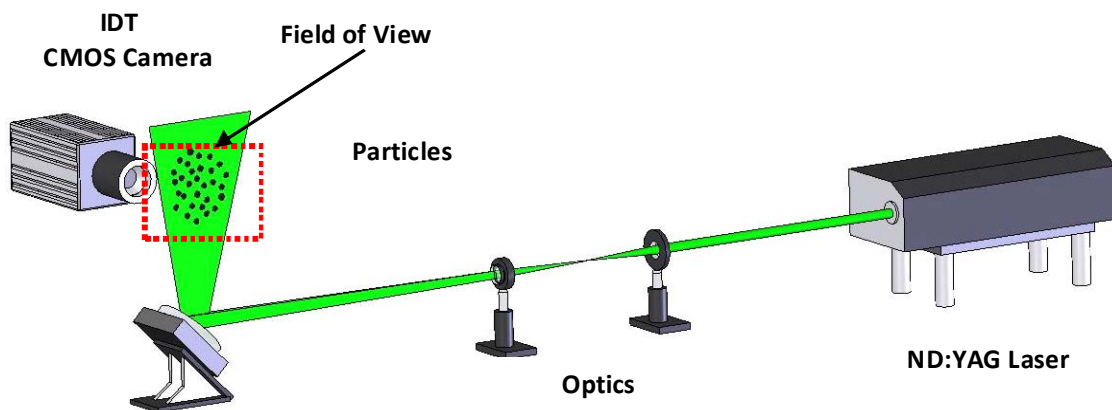


Figure 1.2. A typical DPIV experimental set up with a laser plane illuminating flow tracer particles.

Herein, DPIV is used in either clear channels or tubes to obtain planes of velocity fields spanning the flow as well as the ferrofluid aggregate. High frequency sampling of 100 to 200 Hz is employed to temporally resolve the flow field allowing a detailed view of the development of the flow structures.

The DPIV technique has not been used to any great extent in ferrohydrodynamics. A microscale proof of concept experiment was performed in a ferrofluid, showing steady ferrofluid flows mixed with flow tracer particles velocity vectors could be obtained from the flow [13]. The limiting factor that has contributed to a lack of studies of ferrohydrodynamics using DPIV is the opacity of ferrofluids, which impedes laser light and limits the observation of flow tracer

particles. As a result, most published experimental papers utilize an ultrasound measuring technique to obtain an internal velocity profile or surface measurement techniques [14]. In this work, the small ferrofluid concentrations of interest and the diffused character of the ferrofluid aggregate allows for a first look at its internal structures and the revelation of the mechanisms that drive aggregate dynamics.

1.4 FOCUSED SHADOWGRAPH TECHNIQUE

Focused shadowgraphy allows qualitative visualization of a flow when a significant contrast exists between two fluids or regions of interest. A coherent light source is directed through a spherical and ground glass lens to both focus and expand the beam of light to a region of uniform intensity. In this work, a 250 Watt halogen bulb was used to create a bright region approximately 20 mm by 150 mm, illuminating the contrasting ferrofluid aggregate and water bulk flow. This conventional technique has been used in many different experiments to visualize the surface of ferrofluids [15,16], and along with the ultrasound velocity profile measurements, represents the most popular method for obtaining data in ferrohydrodynamics experiments.

The setup of the shadowgraph experiments presented herein is shown in Figure 1.3. Two orthogonally-oriented cameras were used to image the side and top planes of the test section where the ferrofluid aggregate was oriented.

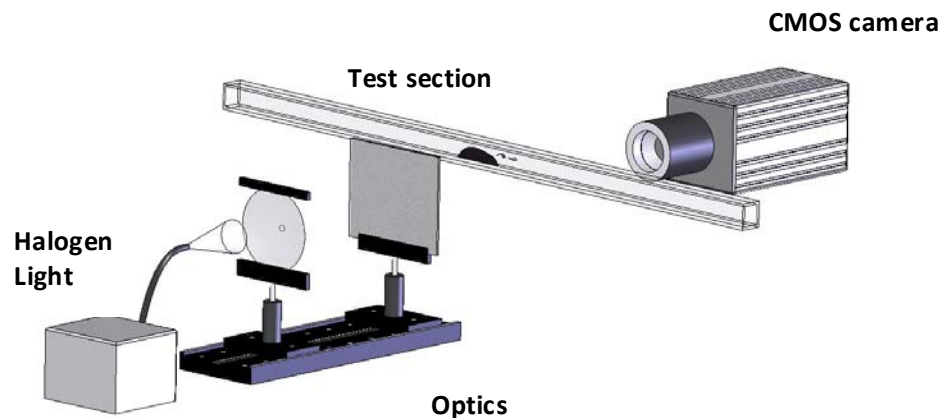


Figure 1.3. Experimental setup of the focus shadowgraph work showing the halogen light source, test section, and digital camera positions.

1.5 REFERENCES

1. Popplewell, J., *Technological applications of ferrofluids*. Physics in Technology, 1984. 15(3):p. 150-156.
2. Rosensweig, R., *Ferrohydrodynamics*. Cambridge University Press, Cambridge, 1985.
3. Abou, *The Normal Field Instability in Ferrofluids: hexagon-square transition mechanism and wavenumber selection*. Journal of Fluid Mechanics, 2000. 416: p. 217-237.
4. Igonin, M. and A. Cebers, *Labyrinthine instability of miscible magnetic fluids*. Journal of Magnetism and Magnetic Materials, 2002. 252: p. 293-295.
5. Pacitto, G., C. Flament, J.-C. Bacri, and M. Widom, *Rayleigh-Taylor instability with magnetic fluids: Experiment and theory*. Physical Review E, 2000. 62(6): p. 7941.
6. Miranda, J.A. and M. Widom, *Parallel flow in Hele-Shaw cells with ferrofluids*. Physical Review E, 2000. 61(2): p. 2114.
7. Ganguly, R., B. Zellmer, and I.K. Puri, *Field-induced self-assembled ferrofluid aggregation in pulsatile flow*. Physics of Fluids, 2005. 17(9): p. 097104-8.
8. Ganguly, R., et al., *Analyzing ferrofluid transport for magnetic drug targeting*. Journal of Magnetism and Magnetic Materials, 2005. 289: p. 331-334.
9. Alexiou, C., et al., *Magnetic Drug Targeting--Biodistribution of the Magnetic Carrier and the Chemotherapeutic agent Mitoxantrone after Locoregional Cancer Treatment*. Journal of Drug Targeting, 2003. 11: p. 139-149.
10. Adrian, R.J., *Dynamic ranges of velocity and spatial resolution of particle image velocimetry*. Measurement Science & Technology, 1997. 8: p. 1393-1398.
11. Adrian, R.J., *Twenty years of particle image velocimetry*. Experiments in Fluids, 2005. 39(2): p. 159-169.
12. Westerweel, J., *Fundamentals of digital particle image velocimetry*. Measurement Science & Technology, 1997. 8(12): p. 1379-1392.
13. Nguyen, N.T., et al., *The application of μ PIV technique in the study of magnetic flows in a micro-channel*. Journal of Magnetism and Magnetic Materials, 2005. 289: p. 396-398.
14. Kikura, H., Y. Takeda, and T. Sawada, *Velocity profile measurements of magnetic fluid flow using ultrasonic Doppler method*. Journal of Magnetism and Magnetic Materials, 1999. 201(1-3): p. 276-280.
15. Mahr, T. and I. Rehberg, *Parametrically Excited Surface Waves in Magnetic Fluids: Observation of Domain Structures*. Physical Review Letters, 1998. 81(1): p. 89.
16. Ohlsen, D.R., and Rhines, P.B., *Laboratory Studies of Equatorially Trapped Waves using Ferrofluid*. Journal of Fluid Mechanics, 1997. 338: p. 35-58.

2 A REVIEW OF FERROHYDRODYNAMICS

2.1 ABSTRACT

The creation of suspended sub-domain particles that react strongly to magnetic fields known as ferrofluids has fostered an ever-increasing body of literature describing the physics and applications of these unique liquids. In the first section of this paper, we review recent contributions of ferrohydrodynamics. In a second section, fluid instabilities involving magnetically-susceptible fluids are reviewed, including the labyrinthine, normal field, Rayleigh-Taylor, and Kelvin-Helmholtz instabilities.

In a final section, the new products that have resulted from the invention and development of ferrofluids for practical applications are reviewed. In the early years of ferrofluids research, many of the applications included seals and dampers made using ferrofluids, as these are lower maintenance and longer-lasting than their conventional counterparts. However, some of the most recent and proliferate applications of ferrofluids have come in the medical field. Ferrofluids have been part of an ongoing effort to find more effective and less invasive treatments for disease. One major research offshoot has focused on Magnetic Drug Targeting (MDT), wherein the ferrofluids are bound to therapeutic agents and then directed to target sites in the body using magnetic fields. Ferrohydrodynamics and especially its instabilities are strongly connected to the success of these applications. Recent results obtained relating to the mechanics of MDT will be presented in the context of ferrohydrodynamic consequences throughout this paper.

2.2 INTRODUCTION

Ferrofluids are a unique class of fluids which are comprised of subdomain particles in suspension that react strongly to magnetic fields. The particles suspended within the ferrofluid are typically composed of iron oxide or magnetite, which are nano to microscales in size [1,2].

They are coated with a surfactant that, due to Van der Waals forces and along with Brownian motion, keeps the particles in a stably suspended state [3]. Ferrofluids were first developed in the 1930s, but were largely unnoticed in physics research until the 1960s [4]. The creation of the particles themselves is an important field where different methods have been developed and new means to develop ferrofluids remain a subject of active study. At present, the most common way to create ferrofluids generally involves complex grinding procedures or chemical processing [5, 6]. The fluid dynamics and physics of ferrofluids have developed as an important branch in fluid mechanics, known as ferrohydrodynamics. This work presents an overview of the state of the art in ferrohydrodynamics. The research discussed herein focuses on ferrohydrodynamics developments in the last two decades, as other review works have been published previously that summarize research from earlier periods. Encompassing reviews of ferrohydrodynamics theory and research efforts up to 1985 have been published by Rosensweig [7, 8, 9, 10].

Hydrodynamic instabilities associated with ferrofluids, which have been a major area of recent research efforts, will be presented. The most prominent of these instabilities in ferrohydrodynamics research are the normal field, labyrinthine, Rayleigh-Taylor, and Kelvin-Helmholtz instabilities. Finally, some of the most recently developed applications of ferrofluids will be presented. Ferrofluids were originally applied to develop longer lasting and lower maintenance seals and dampers. They have been increasingly exploited as a means to develop more effective medical treatments, particularly through drug targeting and hyperthermia.

Instabilities in ferrofluids can have direct consequences in the development of their applications. One example underscoring the influence of instabilities occurs in drug targeting applications. Williams and Vlachos [11, 12] have recently been working to characterize how some of these instabilities may arise under flows encountered in the body, and have shown that at moderate Reynolds numbers in steady and pulsatile flows, the Kelvin-Helmholtz and Rayleigh-Taylor instabilities may arise under appropriate conditions. These instabilities can have significant influence on the behavior and residence time of the aggregates of ferrofluids that are used to target drug treatments, and hence, the effectiveness of the treatment.

2.3 FERROHYDRODYNAMICS

2.3.1 FUNDAMENTAL FERROFLUID FLOWS AND PROPERTIES

Many different ferrofluid flows have been studied to better describe their dynamics, including examinations the mechanisms of macroscale physics are revealed. Polevikov and Tobiska numerically studied the behavior of a ferrofluid droplet in a capillary under an orthogonally applied magnetic field [13]. They used the Young-Laplace equation to describe the shape of the droplet surface coupled with Maxwell's equations to describe the droplet behavior in the capillary. As the contact angle of the droplet increases with respect to the capillary wall, the critical field intensity to destabilize the droplet increases. This result is shown in Figure 1 of Polevikov and Tobiska's original work. Once the critical field is attained, the droplet breaks and spreads over the capillary walls. Finally, as the contact angle of the ferrofluid droplet exceeds 100 degrees, the behavior of the ferrofluid transitions and no longer spreads over the capillary walls. Instead, an elongated ellipse is formed at the critical magnetic field strength, which decreases in height with increasing contact angle of the droplet.

One study at the particle level to reveal larger-scale behaviors by Liu et al showed that a monodisperse collection of magnetically susceptible particles in a droplet will first form chains which break down into columns as the field strength increases [14]. An exponential relationship was determined that describes the column spacing of particles, d , which was

$$d = 1.33L^{0.37} \quad 2.1$$

where L is the cell thickness. The columns of particles were modeled as cylinders, and increasing the column spacing is energetically-favorable, as this minimizes the interactions between separate cylinders of particles.

2.3.2 SURFACE WAVES

Surface wave phenomena have been well-characterized in ordinary liquids [15]. Similar to non-magnetizable liquids and granular flows, ferrofluids exhibit many of the same

characteristics, with the exception that magnetic body forces can be used to delay the onset of instability. One example from ferrohydrodynamics that is readily analogous to granular flows is the jet ejection phenomenon, which occurs in granular media subjected to sufficiently high frequency vertical oscillations of a container. A small amount of ferrofluid retained by a permanent magnet is mechanically shaken at increasing amplitudes eventually reaches a critical amplitude that will result in the ejection of a droplet; further amplitude increases result in a jet of ferrofluid ejected from the free surface [16]. A previous paper by the same authors has also shown that for ejected jets of ferrofluid, applied magnetic fields distort their shape and especially affect the neck portion of the jet, resulting in significant elongation [17].

In addition to the jet phenomena, many other surface mechanics have been studied with magnetic fluids. Due to the opaque nature of ferrofluids, limited measurement techniques have been successfully applied to studies of this type, where most measurements are made by imaging the surface of the fluid or by measuring the internal velocity profiles using ultrasound [18] or other non-optical methods that provide point measurements.

An early work on surface behavior by Perry and Jones used the Langevin magnetization theory to study the application of periodically varying magnetic fields on a pool of ferrofluid containing superparamagnetic nanoparticles [19]. A corresponding experiment was performed, where a pool of ferrofluid was subjected to a magnetic field oscillating at rates between 60 and 140 Hz, generating surface waves. Agreement to within 10 percent of the modeled behavior was obtained for the standing wave pattern wavelength of the ferrofluid. The consideration of both inviscid and viscous effects on the surface phenomenon was included in a work by Brancher [20]. Viscosity was shown to act as a limit to the disturbances in the case of instability or, near transition, can increase or decrease the amplitude of the surface oscillations. In an additional work on the dispersion of waves, Browaeys et al [21] studied the shadowgraphs of a ferrofluid pool to test the dispersion relation originally suggested by Zelazo and Melcher for waves on the ferrofluid interface. The authors found that the monotonic portion of the dispersion equation for the surface waves on a ferrofluid proposed by Zelazo and Melcher agrees well with experimentally obtained data.

The forced wave dispersion relation was also studied analytically by Raitt and Riecke [22]. The Ginzburg-Landau equations were used to describe the driven waves on a ferrofluid surface for small wave amplitudes. Simulations carried out with the Ginzburg-Landau equations indicated that domain structures in the driven waves exist for up to three stable wavenumbers.

An experimental extension of the theoretical work by Raitt and Riecke was performed by Mahr and Rehberg [23]. In the experiment, the magnetic field strength was varied with a fixed driving frequency to study the physics of the parametrically-excited surface waves. Domains and with coexisting wave numbers are observed in the ferrofluid pool. Oscillating defects were also shown to be present, and are indicated by a time-varying set of wave numbers of fluid spikes. Phase oscillations were also observed, wherein the amplitude of the waves both peaks and decays throughout the ferrofluid pool in time. Both the oscillating defects and phase oscillations in the surface waves have not yet been described theoretically.

In an additional study of surface phenomena in ferrofluids, an experiment was performed where the sloshing of a cylinder partly filled with a magnetic fluid under applied magnetic fields was examined. A laterally excited rectangular container partly filled with a ferrofluid was subjected to a non-uniform magnetic field in a first study by Sawada, Kikura, and Tanahashi [24]. The velocity profile of the ferrofluid was measured using ultrasound point measurements. In Figure 5 of the original work by the authors, the normalized surface deflection compared to the driving frequency is plotted for several different magnetic field strengths. Here, the increasing magnetic field strength is responsible for increasing the resonance frequency of the free surface, which is equivalent to the stiffening of the fluid resulting from the increased field strength.

The characterization of the surface behavior was studied in a follow-up experiment to examine the lateral disturbance of a magnetic fluid contained within a cylinder, again using a non-uniform vertically applied magnetic field. Sawada et al [25] identified four main regimes for transverse actuation of 0.42 to 4.17 Hz. At the low end of this range, up to nearly 1.5Hz, transverse oscillation of the surface occurred. As the driving frequency was increased, the transverse oscillations give way to unstable swirling, where the direction of the swirl reverses after the fluid crest completes a rotation about the cylinder. As the driving frequency increases further, the unstable swirling transitions to stable swirling, where the direction of swirl remains constant. Finally, as the forcing is increased up to the maximum of 4.17 Hz, the fourth regime is obtained, wherein the surface displacements are close in amplitude to those at low driving frequencies, and the transverse oscillations are once again observed.

The stable and unstable swirling regimes correspond to the resonance of the free surface sloshing in this experiment. A theoretical comparison to compliment the experiment was performed on linearized potential flow equations, assuming small wave amplitudes. The model

and experiment both confirm a resonance region of the fluid surface that correlate with the unstable and stable swirling regimes.

2.4 INSTABILITIES IN FERROHYDRODYNAMICS

2.4.1 LABYRINTHINE INSTABILITY

The labyrinthine instability is one of the first fluid instabilities studied at length in ferrofluids. The labyrinthine instability develops when a ferrofluid drop is confined to a Hele-Shaw cell with a magnetic field application. Under the application of a magnetic field oriented normal to the surface of the cell at a sufficiently high strength, an initially quiescent drop of ferrofluid will deform to create a fingering pattern as the droplet stretches in all directions into ever decreasing branch sizes. An example illustrating the development of a labyrinthine instability is shown in Figure 1 of the published work by Dickstein et al [26]. Rosensweig, Zahn, and Shumovich [27] showed that the shape contours depend on both the intensity of the magnetic field as well as the spacing of field lines. In contrast, the stabilization of the surface by a tangentially-applied magnetic field of the ferrofluid fingering was shown by Zhan and Rosensweig [28].

Jackson and Goldstein examined these fingering instabilities using Darcy's law to describe the largest growth rate as a function of the Bond number, which relates the strength of dipolar forces with respect to the surface forces [29]. Igonin and Cebers [30] showed analytically and numerically the mechanics of the Labyrinthine instability for a magnetic fluid that is miscible with its surroundings. An analytical model of a step change in magnetic particle concentration and a numerical simulation of a smeared change in particle concentration were performed. A linear stability analysis shows that in both cases, the labyrinthine instability forms under the application of a perpendicularly acting magnetic field of sufficient strength. The numerical simulations show that for a two dimensional flow, viscosity has the important effect of limiting the range of unstable wavelengths. Another result of this work is that the most critical wavelength for instability tends to the height of the Hele-Shaw cell.

A related work is found in an experiment of ferrofluid droplet in a radial Hele-Shaw cell, which is displaced by the injection of air into the cell by Flament et al [31]. In this work, the

perpendicularly-oriented magnetic field induces the development of the labyrinthine instability, as has been demonstrated in previous analytical and numerical studies. Also, a linear stability analysis was used to develop an empirically-based expression for the number of fingers in the interface between the ferrofluid and air based on the air inflow rate, which is given by

$$P = f(n)2R_g \quad 2.2$$

where P is the length of the interface and R_g is the radius of gyration of the shape outlined by the interface. The expression for $f(n)$ is the master curve used to describe the overall relationship between the nature of the instability and its corresponding number of fingers. This equation was used to collapse data for several different field strengths onto the same line, which is described by $f(n)$.

The onset of the labyrinthine instability at the particle level in a Hele-Shaw cell was the subject of a theoretical study based on the Helmholtz free energy equation. Ytreberg and MacKay [32] showed that the energetically-favorable aggregate radius decreases as the magnetic field strength is increased, and increases as the cell height increases. The Helmholtz free energy was minimized to obtain these results for a hexagonal-shaped spacing. The authors speculated that the region described by large container thicknesses and low magnetic fields, or low container thicknesses and high magnetic fields leads to the labyrinthine instability. An experimental comparison by Hong et al shows agreement with the theory presented by Ytreberg and MacKay [33].

A description of the transition from the labyrinthine instability a more extreme instability in the form of spiral turbulence, or the appearance of helicoidal stripes of turbulence, was presented by Hagberg and Meron, where this transition may occur as a result of transverse perturbations [34], and occurs sometimes in other phenomena [35]. A transition to spiral turbulence from the labyrinthine state can be induced by instability to transverse perturbations, which results in the splitting of vortices. The nucleation of these vortices may ultimately foster the transition to a spiral turbulent flow.

2.4.2 NORMAL FIELD INSTABILITY

The normal field instability arises due to an interaction of the surface tension forces and magnetic forces acting on a ferrofluid free surface when the applied field is oriented orthogonally to that free surface. At a critical field strength, the normal field instability arises in the form of square-based peaks or spikes that protrude from the free surface of the ferrofluid, and is also referred to as the Rosensweig instability. One of the first studies of the normal field instability was published in 1967 by Crowley and Rosensweig [36]. Critical magnetic field strengths and spacing of the peaks in the normal field instability were described from experimental data. Crowley and Rosensweig first showed that the peaks take on a hexagonal-shaped base, and that the spacing of these peaks can be derived from the critical wavelength of the surface instability.

Recent studies indicate that the normal field instability has different states, shifting from hexagonal-shaped peaks to square peaks as the field strength is increased. Boudouvis demonstrated both experimentally and theoretically that this transition occurs, and that the transition is subject to hysteresis behavior with respect to the instability [37]. If a ferrofluid displaying the normal field instability is being driven by a magnetic field that is decreasing in intensity, once the field drops to a low enough strength, the instability will disappear. However, the decreasing field will have a greater field strength for the disappearance of the instability than for the appearance of the instability for an increasing magnetic field, and is shown in Figure 2 of the original work.

The transition between the square and hexagonal-shaped peaks of the normal field instability was visually shown in shadowgraphs by Abou [38], shown in Figures 1 and 2 of the originally published work. The transition between the two peak shapes occurs as the magnetic field intensity increases sufficiently beyond the initial appearance of the square-based peaks. The appearance of “Penta-Hepta” defects in the square peaked surface initiates the transition from the square to hexagon peaks. The transition also differs when the magnetic field is adjusted quasi-statically or in step changes, where slow transitions result in gradual appearance of more defects until a full transition occurs. Jumps in field intensity cause the growth of peaks at lower field strengths. Abou also showed that the presence of peak base defects in the normal field instability is a function of the ferrofluid container, where a container that takes the shape of the peak bases is less likely to present with defects. Reimann et al later showed that tilting

the magnetic field itself with respect to the free surface of the ferrofluid can disrupt the surface symmetry of a normal field instability, yielding different realizations of the instability based on the degree of tilt and magnetic field [39]. Examination of the nonlinear behavior of the normal field instability was completed by Gollwitzer, Rehberg, and Richter [40] by using x-rays to obtain a complete profile of the ferrofluid spikes, which can become unmeasurable with more conventional shadowgraph techniques as the peaks grow in size and develop nonlinear behaviors. By modeling the normal field instability with Maxwell's equations, Bashtovoi et al [41] showed that the peak of the surface spikes grows more rapidly in amplitude than does the elevation of the foot of these peaks.

The normal field instability also manifests in experiments with moving magnetic fields. A drop of ferrofluid was placed in the influence of a rotating magnetic field, and the ferrofluid drop deformed as the rotation frequency increased from the 4 Hz up to 4 KHz, and as the applied magnetic field increased [42]. With increasing magnetic field, the drop stretches into a star shape and finally, spikes appear on its surface, forming different starfish-like shapes based on the rotation frequency of the field and field strength. The authors also showed that the magnetic droplet will corotate in the direction of the magnetic field at a frequency on the order of Hertz based on a varying magnetic field on the order of a Kilohertz. An extension studying the normal field instability under varying magnetic fields was performed where an applied steady magnetic field was overlaid with an alternating magnetic field cycling between 2 to 12 Hz to generate harmonically appearing spikes in the ferrofluid [43]. An examination of the behavior of these peaks when the applied magnetic field is suddenly switched on was studied numerically by Matthies and Tobiska [44]. The rapid application of the magnetic field above the critical value to initiate the normal field instability showed damped oscillations of the surface profile that ceased after 1 second and thereafter maintained a stable peak height. The amplitude of the oscillations increases with increased field strength, and then dies out to attain the final steady state peak height, which grows as the field strength is amplified.

2.4.3 RAYLEIGH-TAYLOR INSTABILITY

The Rayleigh-Taylor instability arises from a system of two fluids of different densities when the lighter fluid is accelerated into the denser fluid. The Rayleigh-Taylor instability

develops as a result of the competition between surface tension and body forces acting on the interface between the two fluids [45,46]. When at least one of the two fluids is magnetically susceptible, the Rayleigh-Taylor instability can manifest itself as an initially planar interface that can be destabilized after the application of a perpendicularly-oriented magnetic field while the capillary forces at the interface of the two fluids provide stabilization.

The Rayleigh-Taylor instability may also develop without the magnetic field present, and is driven by density differences when the denser fluid is supported against gravity by a lighter fluid, but longer time scales are required to observe this behavior. When a magnetic field is present and the Rayleigh-Taylor instability occurs, ferrofluid fingers are drawn through a non-susceptible liquid towards the magnet. As the system nears equilibrium, the non-magnetic liquid is displaced opposite to the magnet location. As the dense fluid coalesces, the fingers are slowly reincorporated into a main mass of the ferrofluid as it reaches equilibrium on the side of the container nearest to the magnet.

The influence of the magnetic field on a system subject to the Rayleigh-Taylor instability was the subject of a numerical study by Malik [47]. A tangentially-oriented magnetic field was applied with respect to the interface between a magnetic fluid and a negligibly dense medium, while gravitational forces were applied orthogonally with respect to the interface. Considering the effect of a non-uniform magnetic field, it was shown that if the field is directed inwards towards the center of the interface, the destabilizing gravitational forces are assisted, resulting in decreased interface stability. Conversely, a magnetic field radiating outward from the interior of the magnetic fluid acts as a stabilization mechanism.

Pacitto et al. studied the Rayleigh-Taylor instability using a magnetic fluid placed above a layer of immiscible oil [48]. The authors predicted numerically and observed experimentally an increase in the wavelength of the instabilities as well as the growth rate of the unstable front as the magnetic field strength increased using Darcy's equation. Figure 7 from the authors' original publication shows an image from the experiment depicting the growth of fingering of the Rayleigh-Taylor instability. In image A, the development of the fingers is observed as the ferrofluid stretches down into the oil. In image B, the fingering has reached its final state in that it has stretched to the bottom of the container. Coalescence of ferrofluid then occurs, where the fingers collapse into the growing ferrofluid aggregate. As the interface between the magnetic fluid and oil destabilizes, an exponential growth rate of the finger length of the

ferrofluid was observed. As the applied magnetic field strength is increased, the growth rate of the instability increases.

The Rayleigh-Taylor instability also has implications in Magnetic Drug Targeting. A study of the interaction of ferrofluid aggregates with steady and pulsatile flows performed by the author shows that the location of the magnet draws the ferrofluid through the water, accelerating the streakline, resulting in the development of the Rayleigh-Taylor instability.

Figure 2.1 shows the development of the Rayleigh-Taylor instability in the form of characteristic spikes and bubbles as the incident flow is increased. In images A and B, a streakline of ferrofluid has reached the permanent magnet, located at the top of the test section in quiescent flow. The interaction between the magnetic field and the ferrofluid results in perturbations of the streakline. As flow is ramped up, in images C and D, the streakline is displaced downstream. However, it is also deformed by the magnetic field, and a series of expanding mushroom-shaped ferrofluid structures appear, translating downstream with the ferrofluid stream. Here, the bulk flow is at a Reynolds number of 400, so it is within the range of Reynolds that could occur in large human arteries. The Rayleigh-Taylor instability could result in diminished effectiveness of the targeting due to the increased interaction of the ferrofluid with the bulk flow.

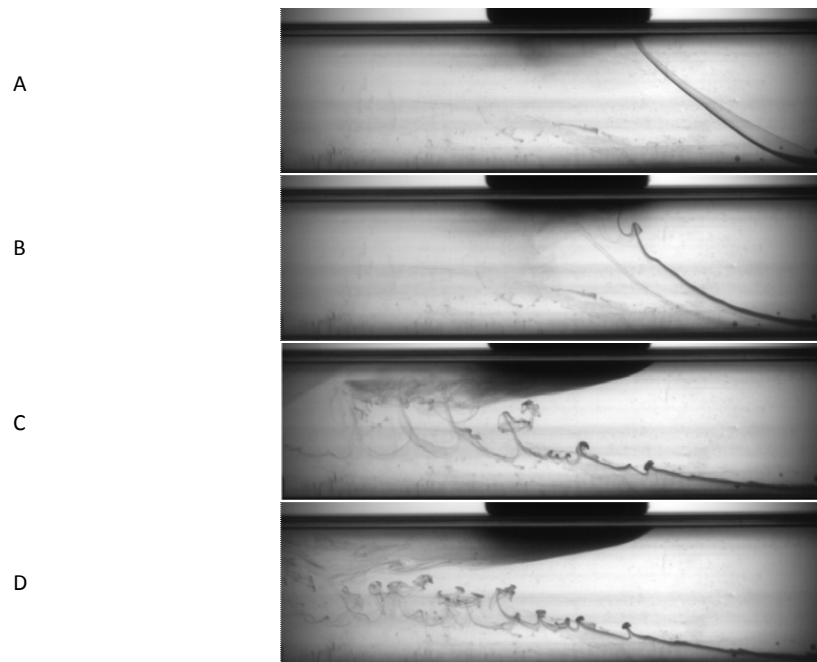


Figure 2.1. The Rayleigh-Taylor instability in a steady water flow with a miscible ferrofluid streakline entering at the bottom of the channel.

2.4.4 KELVIN HELMHOLTZ INSTABILITY IN FERROFLUIDS

In an ordinary system of two parallel-flowing non-magnetic fluids, the Kelvin-Helmholtz (K-H) instability results from shearing force acting on a plane interface. In the case of interfacial flows, surface tension acts to stabilize the interface, while buoyancy or gravitational forces destabilize the interface based on their orientation. In a system containing a ferrofluid, the magnetic forces can replace or augment both the surface tension and body force effects. Therefore, the instability may be controlled or fostered based on the orientation of an applied magnetic field. Under the application of an orthogonally-oriented magnetic force, the magnetic body force acts to destabilize the system and produce the characteristic Kelvin-Helmholtz waves, while the tangentially-applied field stabilizes the interface as observed in the instabilities presented in previous sections.

The Kelvin-Helmholtz instability in magnetically susceptible liquids has been the subject of several studies to date. However, many such studies have focused purely on analytical or numerical descriptions of Kelvin-Helmholtz instability. Malik and Singh examined the nonlinear instability of two parallel magnetic fluids with magnetic field gradients acting in a direction parallel to the interface of the two [49]. The bottom fluid set to be stationary, with the top fluid moving at a specified velocity. Based on linear theory and the dispersion equation first described by Rosensweig, Malik and Singh showed that the flow between two magnetic fluids may be amplified to a higher speed before the onset of instability. Similar to other instabilities, tangentially-applied fields with respect to an interface act to stabilize that interface. When the difference between the two velocities is less than the critical velocity difference, the interface is unstable against modulations. For velocity differences above the critical velocity difference, the amplitude is described by the non-linear Klein-Gordon equation.

Like the study of Malik and Singh, the shear flow of two ferrofluids in porous media under a tangentially-applied magnetic field was studied by Moatimid with both linear and nonlinear formations [50,51], but also taking into account linear and non-linear effects as well as the porosity of media and heat and mass transfer. For non-porous media, heat and mass transfer are destabilizing, while for porous media, these effects act as a stabilizing influence. A Ginzburg-Landau equation was obtained for the non-linear stability analysis of this flow, which has also been used to describe the waves appearing in the wake of a circular cylinder. As the velocity of one of either of the fluids is increased, the envelope of the unstable region is found to decrease

in size. This indicates that counter to the linear stability study, the nonlinear terms included in the Ginzburg-Landau equation show that the streaming velocity has a stabilizing influence.

Miranda and Widom numerically investigated ferrofluid flowing in parallel with a non-magnetic fluid in a Hele-Shaw cell [52]. Three different orientations of an applied magnetic field were studied numerically, with tangential, orthogonal, and perpendicular placement with respect to the major dimension of the Hele-Shaw cell. Deriving the Darcy equation for flow in a Hele-Shaw cell with a ferrofluid, Miranda and Widom showed that with no applied magnetic field, the interface between the ferrofluid and non-magnetic liquid is damped and stable. However, under the application of a magnetic field, the interface may be stabilized or destabilized depending on the direction of application. Similar to the findings of Malik and Moatimid, Miranda and Widom found that tangentially-applied magnetic fields act to stabilize the interface, as these fields act generally as an effective boost of surface tension and gravitational effects. Both normal and perpendicularly oriented fields, however, can foster destabilization.

The stability of a fluidized bed containing a magnetic fluid with an applied magnetic field parallel to the direction of the free stream velocity was numerically described by Sobral and Cunha [53]. A continuum model using averaged quantities that incorporated the additional magnetic stresses was developed. The magnetic pressure coefficient was recovered from the equations, which is the ratio of the magnetic pressure over the fluid dynamic pressure. As the magnetic pressure coefficient increases, the growth of disturbances in the fluidized bed becomes more damped and stable for tangentially-applied fields.

The effect of the K-H instability becomes important in some of the applications of ferrofluids. In drug targeting, ferroparticles injected intra-arterially are used to create aggregates with external magnetic fields, and interact with the blood flow. Studies of the interaction between the aggregate and flow by the authors indicate that for Reynolds numbers 300 or higher, the pulsatile of flow in arteries can lead to Kelvin-Helmholtz shedding from the aggregate. The Kelvin-Helmholtz shedding from a ferrofluid aggregate retained by a permanent magnet is shown over one period of pulsatility for an average Reynolds number of 500 in Figure 2.2 For low flow rates as in Images A and B, the aggregate has coalesced and is contained to a compact region near the magnet. Ramp up of the flow to peak levels as in Image C results in the appearance of small amplitude waves on the interface between the aggregate and water that give way to the Kelvin-Helmholtz instability. Kelvin-Helmholtz shedding has a significant

influence on the residence time of the aggregate, and ultimately, the effectiveness of the drug targeting technique.



Figure 2.2. Kelvin-Helmholtz shedding from a ferrofluid aggregate in pulsatile flow with a Reynolds number based on the average flow rate of 600 shown over one period of flow. During the highest flow rates, rolls of ferrofluid are observed shedding from the main aggregate.

2.5 FERROFLUID APPLICATIONS

2.5.1 DRUG TARGETING AND HYPERTHERMIA

Ferrofluids are used in a wide range of applications beyond studies of pure scientific interest. In the last 10 years, the use of ferrofluids in medical applications has been studied both medically and mechanistically. In particular, the applications of ferrofluids in Magnetic Drug Targeting (MDT) have shown great promise. MDT utilizes ferrofluids bound to medicinal treatments to direct these therapies to specific target sites within the patient. This improves the effectiveness of the treatment, while maintaining low toxicity to healthy organs. MDT stands in contrast to conventional drug delivery, where treatment is given systemically with no means to specify its direction. This method often leads to high toxicity in healthy systems in the patient, while the site of the tumor or other disease receives a small fraction of the total dosage.

Clinical studies in laboratory animals have shown that applying 50% of the typical systemic dose of a treatment coupled with drug targeting can result in tumor remission [54]. The effectiveness of targeting ferrofluid by Magnetic Resonance Images (MRI) was studied by Goodwin et al [55], wherein the ferrofluid was observed in targeted regions of the body, but only in limited quantities in the liver and other systems. Ferrofluids were directed to several different organs in a swine, and the MRI images showed that treatment can be directed to specific targets in the body.

A representative plot of the results obtained in several different studies is shown in Figure 7 of Alexiou et al [56], where a tumor on the leg of a rabbit was reduced using the targeted treatment in conjunction with half of the typical treatment dosage. Additional studies by the same group reveal specific targeting capabilities of magnetic targeted treatments [57, 58].

In these clinical trials, 20 to 50% of the systemic cancer treatment dose was injected intra-arterially to VX-2 Squamous cell carcinoma in rabbits [59]. A 1.7 Tesla electromagnet was applied to the tumor for 60 minutes, which was located on the hind leg of the rabbit. Tumor remission was attained after a period of up to 2 months following one treatment using the targeted ferrofluid. Slices of the tumor examined microscopically show the presence of the treatment bound to the ferrofluid on the tumor border.

One clinical study has been conducted on humans thus far, where patients with a variety of cancers were treated using the MDT method [60]. The patients' illnesses had reached an advanced stage, and they had been unsuccessfully treated using conventional drug delivery methods. A 0.5 Tesla permanent magnet was used to target 100 nm ferrofluid particles functionalized with the appropriate treatment for the tumors that were 0.5 cm or less away from the magnet. The volume of functionalized ferrofluid administered to the patients totaled 0.5% blood volume. In four of the fourteen patients participating in the study, four experienced a slight reduction in tumor size ten days after treatment. Moreover, there was no noticeable increase in toxicity to the patients resulting from the treatment with ferrofluid nanoparticles. Although the results shown in this study do not provide definitive evidence, the promise of the MDT technique was visible. However, the need for a better understanding of the mechanics behind MDT is underscored. Despite the exceptional promise of laboratory experiments, the translation from the promising results in mice has not yet met success in work with humans.

Medical applications of ferrofluids have been studied as well in the mechanics community, as clinical studies of MDT focus purely on whether the clinical treatment produces the desired tumor remission, but neglects the mechanics of the process. Currently, a major limitation of MDT is the inability to generate strong field gradients at locations away from the magnet's surface. The strength of a point dipole will drop as the cube of the radius, and therefore magnetic fields applied to a target far from the peak gradient location will be ineffective at magnetizing and attracting ferrofluid. Some mechanics-based research includes efforts as to the means of improved implementations. Physics-based studies of MDT have spanned biofluids as agents for magnetization to the use of implants that are susceptible to magnetic fields to improve the effectiveness of an MDT treatment. An experiment in which the retention of ferrofluid was tested in a model blood vessel made of rubber preliminarily described the exponential washaway of ferrofluid from the main aggregate in The authors also performed an in vivo experiment with the stomach of a rabbit and confirmed that the magnetic field gradients needed to retain a drop of ferrofluid are high, generally equivalent to those found at the tips of magnets.

Additional works that studied the retention of a ferrofluid aggregates towards their development of the Magnetic Drug Targeting application were performed by Ganguly et al [61]. The periodic washaway of an initially injected 3 micro liters of water-soluble ferrofluid for in a bulk flow with a Reynolds number of 250 was demonstrated. Numerical simulations performed

on such masses by finite difference methods that model also described the recirculation of ferrofluid within the aggregate itself. In pulsatile flow, the washaway of ferrofluid is magnified by flow pulsatility, and increases with increasing Reynolds number [62]. An additional paper presented relations for the dispersion of ferrofluid from the aggregate mass [63]. One important finding is the correlation of the washaway time to the -0.2 power of the Reynolds number of the bulk flow.

Since strong magnetic fields are required to perform effective MDT in the body, the use of magnetic or magnetizable implants is currently being explored. Two numerical studies by Chen et al have explored the possibility of using magnetizable implanted wires or stents to amplify the magnetic field gradients experienced by ferroparticles near target sites [64,65]. The results shown in these papers indicate that using magnetizable implants with field strengths up to 1 Tesla can improve the collection of magnetic particles by up to 60%.

Xu et al studied the retention of ferroparticles at different flow speeds and distances away from a permanent magnet [66]. The particle retention was found to be high when the magnet tip is close to the target site, as has been proven for ferrofluids. A family of exponentially decaying curves for different distances from the magnet tip describes the retention of ferrofluid as a function of bulk flow velocity. A numerical study of the MDT application in a biological flow was performed by Voltairas [67]. A ferrofluid aggregate was examined under the influence of an orthogonally-oriented magnetic field. Similar to the experimental study of Xu et al, Voltairas studied the blood flow velocity with its relationship to the applied magnetic field, and identified an upper bound for the flow velocity based on the applied field strength.

The application of magnetic fields has also been studied for red blood cells themselves as a means to manipulate them at a distance. The hemoglobin in red blood cells has a nonzero susceptibility, and the effect of the magnetic field on red blood cells has been studied in the context of biological flows. Under the application of sufficiently strong magnetic fields, the blood becomes magnetized, as it is paramagnetic or diamagnetic depending on its oxygenation. Loukopoulos and Tzirtzilakis studied the behavior of biomagnetic fluid flow under the influence of a point magnetic source located externally to one side of a tube [68,69]. The results of the numerical study showed that the biomagnetic fluid aggregates around the magnetic point source, causing a partial flow blockage on the side of the tube nearest to the magnetic field.

Khashan extended the study of biomagnetic fluid to flows downstream of stenoses, showing that the magnetic field can affect the reattachment point of the flow [70].

Other applications of ferrofluids in the medical field include using ferroparticles to induce local hyperthermia in the region of tumors [71,72] in order to induce necrosis. Hyperthermia has been shown to enhance the effectiveness of conventionally available treatments. The ability to create highly localized hyperthermia using ferrofluids can ensure, like MDT, that healthy organs and tissues are not harmed by the treatment. The hyperthermia is induced using an AC magnetic field cycling rapidly to create ferroparticle rotation. An *in vitro* evaluation of different types of ferrofluids with modulated hyperthermia was performed on peritoneal ascystic sarcoma MX11 cells [73]. After 6 hours, without hyperthermia, the survival rate was over 9.4%. However, after 40 minutes of radiofrequency field application at 0.88 MHz with a magnetic field intensity of 90 Oe, the survival rate dropped to just above 1%, similar to when the cells were placed in a hot water bath. Although this technique is not as mature as MDT, hyperthermia clearly has promise to produce increased efficacy in disease treatment.

2.6 OTHER FERROFLUID APPLICATIONS

The first applications that capitalized on ferrofluids were seals and dampers that use ferrofluids as a means to tune and vary their properties. Dampers with ferrofluids also have other characteristics that make them attractive choices, including long life span, strong sealing potential, and low maintenance compared to other seals [74]. Devices that have benefitted from ferrofluids include X-ray and CAT scan machines, which use dynamic process seals as a means to relieve heat build up on an anode where the machine focuses a high power electron beam [75]. The seal rotates the anode to a cooler spot rapidly so that continuous images may be obtained.

2.7 CONCLUSIONS

The creation of suspended sub-domain particles that react strongly to magnetic fields has fostered an ever-increasing breadth of literature describing ferrofluid physics and their

applications. In the first section of this paper, we reviewed the recent contributions towards a physical and theoretical understanding of ferrohydrodynamics. In a second section, fluid instabilities involving magnetic fluids were reviewed. In ferrohydrodynamics, the major instabilities that have been studied to date are the labyrinthine instability, normal field instability, Rayleigh-Taylor instability, and Kelvin-Helmholtz instability.

In a final section, the newer developments that have resulted from the invention and development of ferrofluids for practical applications are reviewed. In the early years of ferrofluids research, many of the applications included seals and dampers made using ferrofluids, as these are lower maintenance and longer-lasting than conventional seals. However, some of the most recent and proliferate applications of ferrofluids have come in the medical field. Ferrofluids have been part of an ongoing effort to discover more effective and less invasive treatments for disease. One major research offshoot has focused on Magnetic Drug Targeting, wherein the ferrofluids are bound to treatments and then directed to target sites in the body using magnetic fields. Moreover, using ferrofluids as a means to create localized hyperthermia has also been investigated as a means to destroy diseased tissue. Based on the ability to control ferrofluids and ferroparticles at a distance and their increasing prevalence in technology, a complete understanding of all aspects of ferrohydrodynamics will become a necessity.

2.8 REFERENCES

1. Gupta, A.K. and M. Gupta, *Synthesis and surface engineering of iron oxide nanoparticles for biomedical applications*. *Biomaterials*, 2005. 26(18): p. 3995-4021.
2. Wakamatsu, H., et al., *Preparation and characterization of temperature-responsive magnetite nanoparticles conjugated with N-isopropylacrylamide-based functional copolymer*. *Journal of Magnetism and Magnetic Materials*, 2006. 302(2): p. 327-333.
3. Popplewell, J., *Technological applications of ferrofluids*. *Physics in Technology*, 1984. 15(3): p. 150-156.
4. Papell, S.S., *Low viscosity magnetic fluid obtained by the colloidal suspension of magnetic particles*. US Patent Specification 3 215 572, 1964.
5. Kim, D. K., Y. Zhang, et al. "Synthesis and characterization of surfactant-coated superparamagnetic monodispersed iron oxide nanoparticles." *Journal of Magnetism and Magnetic Materials*, 2001. 225(1-2): 30-36.

-
6. Gupta, A. K. and M. Gupta. "Synthesis and surface engineering of iron oxide nanoparticles for biomedical applications." *Biomaterials*, 2005. 26(18): 3995-4021.
 7. Neuringer, J.L. and R.E. Rosensweig, *Ferrohydrodynamics*. *Physics of Fluids*, 1964. 7(12): p. 1927-1937.
 8. Rosensweig, R., *Ferrohydrodynamics*. Cambridge University Press, Cambridge, 1985.
 9. Rosensweig, R.E., *Directions in ferrohydrodynamics (invited)*. *Journal of Applied Physics*, 1985. 57(8): p. 4259-4264.
 10. Rosensweig, R.E., *Magnetic Fluids*. *Annual Review of Fluid Mechanics*, 1987. 19(1): p. 437-461.
 11. Williams, A.M, and P. Vlachos, August 2008, "Spatiotemporally-resolved Dynamics of Dispersing Ferrofluid Aggregates." ASME Fluids Engineering Division Summer Meeting, Paper Number FEDSM2008-55275.
 12. Williams, A.M. and P. P. Vlachos, August 2008, "The Dynamics of Accumulating Ferrofluid Aggregates." ASME Fluids Engineering Division Summer Meeting, Paper Number FEDSM2008-55101.
 13. Plevnikov, V. and L. Tobiska, *Instability of magnetic fluid in a narrow gap between plates*. *Journal of Magnetism and Magnetic Materials*, 2005. 289: p. 379-381.
 14. Liu, J., et al., *Field-Induced Structures in Ferrofluid Emulsions*. *Physical Review Letters*, 1995. 74(14): p. 2828.
 15. Haskell, N.A., *The dispersion of surface waves on multilayered media*. *Bulletin of the Seismological Society of America*, 1953. 43(1): p. 17-34.
 16. Sudo, S., K. Ise, and S. Kamiyama, *Jet formation of magnetic fluid with vibration of an annular magnet*. *Journal of Magnetism and Magnetic Materials*, 2002. 252: p. 162-165.
 17. Sudo, S., T. Ikohagi, et al. "Dynamic behavior of a magnetic fluid jet injected from a vibrating nozzle." *Journal of Magnetism and Magnetic Materials*, 1999. 201(1-3): 306-309.
 18. Kikura, H., Y. Takeda, and T. Sawada, *Velocity profile measurements of magnetic fluid flow using ultrasonic Doppler method*. *Journal of Magnetism and Magnetic Materials*, 1999. 201(1-3): p. 276-280.
 19. Perry, M.P. and T.B. Jones, *Interfacial parametric ferrohydrodynamics*. *Journal of Applied Physics*, 1975. 46(2): p. 756-760.
 20. Brancher, J., *Interfacial instability in viscous ferrofluids*. *Magnetics, IEEE Transactions on*, 1980. 16(5): p. 1331-1336.
 21. Browaeys, J., et al., *Surface waves in ferrofluids under vertical magnetic field*. *The European Physical Journal B - Condensed Matter and Complex Systems*, 1999. 9(2): p. 335-341.

-
22. Raitt, D. and H. Riecke, *Parametric forcing of waves with a nonmonotonic dispersion relation: Domain structures in ferrofluids*. Physical Review E, 1997. 55(5): p. 5448.
23. Mahr, T. and I. Rehberg, *Parametrically Excited Surface Waves in Magnetic Fluids: Observation of Domain Structures*. Physical Review Letters, 1998. 81(1): p. 89.
24. Sawada, T., H. Kikura, and T. Tanahashi, *Kinematic characteristics of magnetic fluid sloshing in a rectangular container subject to non-uniform magnetic fields*. Experiments in Fluids, 1999. 26(3): p. 215-221.
25. Sawada, T., Y. Ohira, and H. Houda, *Sloshing behavior of a magnetic fluid in a cylindrical container*. Experiments in Fluids, 2002. 32(2): p. 197-203.
26. Dickstein, A.J., et al., *Labyrinthine Pattern Formation in Magnetic Fluids*. Science, 1993. 261(5124): p. 1012-1015.
27. Rosensweig, R.E., M. Zahn, and R. Shumovich, *Labyrinthine instability in magnetic and dielectric fluids*. Journal of Magnetism and Magnetic Materials, 1983. 39(1-2): p. 127-132.
28. Zahn, M. and R. Rosensweig, *Stability of magnetic fluid penetration through a porous medium with uniform magnetic field oblique to the interface*. Magnetics, IEEE Transactions on, 1980. 16(2): p. 275-282.
29. Jackson, D.P., R.E. Goldstein, and A.O. Cebers, *Hydrodynamics of fingering instabilities in dipolar fluids*. Physical Review E, 1994. 50(1): p. 298.
30. Igonin, M. and A. Cebers, *Labyrinthine instability of miscible magnetic fluids*. Journal of Magnetism and Magnetic Materials, 2002. 252: p. 293-295.
31. Flament, C., et al., *Viscous fingering in a magnetic fluid. I. Radial Hele-Shaw flow*. Physics of Fluids, 1998. 10(10): p. 2464-2472.
32. Ytreberg, F.M. and S.R. McKay, *Calculated properties of field-induced aggregates in ferrofluids*. Physical Review E, 2000. 61(4): p. 4107.
33. Hong, C.-Y., et al. *Ordered structures in Fe₃O₄ kerosene-based ferrofluids*. in *The 41st annual conference on magnetism and magnetic materials*. 1997. Atlanta, Georgia (USA): AIP.
34. Hagberg, A. and E. Meron, *From labyrinthine patterns to spiral turbulence*. Physical Review Letters, 1994. 72(15): p. 2494.
35. Lee, K.J., et al., *Pattern Formation by Interacting Chemical Fronts*. Science, 1993. 261(5118): p. 192-194.
36. Crowley, M.D. and R.E. Rosensweig, *The interfacial stability of a ferromagnetic fluid*. Journal of Fluid Mechanics, 1967. 30(4): p. 671-688.
37. Boudouvis, A.G., et al., *Normal field instability and patterns in pools of ferrofluid*. Journal of Magnetism and Magnetic Materials, 1987. 65(2-3): p. 307-310.

-
38. Abou, *The Normal Field Instability in Ferrofluids: hexagon-square transition mechanism and wavenumber selection*. Journal of Fluid Mechanics, 2000. 416: p. 217-237.
39. Reimann, B., et al., *Hexagons become the secondary pattern if symmetry is broken*. Physical Review E (Statistical, Nonlinear, and Soft Matter Physics), 2005. 71(5): p. 055202-4.
40. Gollwitzer, C., I. Rehberg, et al. *Via hexagons to squares in ferrofluids: experiments on hysteretic surface transformations under variation of the normal magnetic field*. Journal of Physics: Condensed Matter, 2006. 18(38): S2643-S2656.
41. Bashtovoi, V.G., et al., *Computer modeling of the instability of a horizontal magnetic-fluid layer in a uniform magnetic field*. Journal of Magnetism and Magnetic Materials, 2002. 252: p. 299-301.
42. Bacri, J.C., A.O. Cebers, and R. Perzynski, *Behavior of a magnetic fluid microdrop in a rotating magnetic field*. Physical Review Letters, 1994. 72(17): p. 2705.
43. Bacri, J.C., U. Ortona, and D. Salin, *Magnetic-fluid oscillator: Observation of nonlinear period doubling*. Physical Review Letters, 1991. 67(1): p. 50.
44. Matthies, G. and L. Tobiska, *Numerical simulation of normal-field instability in the static and dynamic case*. Journal of Magnetism and Magnetic Materials, 2005. 289: p. 346-349.
45. Sharp, D.H., *An overview of Rayleigh-Taylor instability*. Physica D: Nonlinear Phenomena, 1984. 12(1-3): p. 3-10.
46. Ratafia, M., *Experimental investigation of Rayleigh-Taylor instability*. Physics of Fluids, 1973. 16(8): p. 1207-1210.
47. Malik, S.K. and M. Singh, *Bubble formation and nonlinear Rayleigh-Taylor instability in magnetic fluids*. Physical Review Letters, 1989. 62(15): p. 1753.
48. Pacitto, G., C. Flament, J.-C. Bacri, and M. Widom, *Rayleigh-Taylor instability with magnetic fluids: Experiment and theory*. Physical Review E, 2000. 62(6): p. 7941.
49. Malik, S.K. and M. Singh, *Finite amplitude Kelvin--Helmholtz instability in magnetic fluids*. Physics of Fluids, 1986. 29(9): p. 2853-2859.
50. Moatimid, G. M. *Stability Properties of Ferromagnetic Fluids in the Presence of an Oblique Field and Mass and Heat Transfer*. Physica Scripta, 2002. 65(6): 490-501.
51. Moatimid, G., *Nonlinear Kelvin-Helmholtz instability of two miscible ferrofluids in porous media*. Zeitschrift für Angewandte Mathematik und Physik (ZAMP), 2005. 57(1): p. 133-159.
52. Miranda, J.A. and M. Widom, *Parallel flow in Hele-Shaw cells with ferrofluids*. Physical Review E, 2000. 61(2): p. 2114.

-
53. Sobral, Y.D. and F.R. Cunha, *A stability analysis of a magnetic fluidized bed*. Journal of Magnetism and Magnetic Materials, 2003. 258-259: p. 464-467.
54. Alexiou, C., et al., *Locoregional Cancer Treatment with Magnetic Drug Targeting*. Cancer Research, 2000. 60(23): p. 6641-6648.
55. Goodwin, S., et al., *Targeting and retention of magnetic targeted carriers (MTCs) enhancing intra-arterial chemotherapy*. Journal of Magnetism and Magnetic Materials, 1999. 194(1-3): p. 132-139.
56. Alexiou, C., et al., *Magnetic mitoxantrone nanoparticle detection by histology, X-ray and MRI after magnetic tumor targeting*. Journal of Magnetism and Magnetic Materials, 2001. 225(1-2): p. 187-193.
57. Alexiou, C., et al., *Magnetic drug targeting: biodistribution and dependency on magnetic field strength*. Journal of Magnetism and Magnetic Materials, 2002. 252: p. 363-366.
58. Alexiou, C., et al., *In vitro and in vivo investigations of targeted chemotherapy with magnetic nanoparticles*. Journal of Magnetism and Magnetic Materials, 2005. 293(1): p. 389-393.
59. Alexiou, C., et al., *Magnetic Drug Targeting--Biodistribution of the Magnetic Carrier and the Chemotherapeutic agent Mitoxantrone after Locoregional Cancer Treatment*. Journal of Drug Targeting, 2003. 11: p. 139-149.
60. Lubbe, A.S., C. Alexiou, and C. Bergemann, *Clinical Applications of Magnetic Drug Targeting*. Journal of Surgical Research, 2001. 95(2): p. 200-206.
61. Ganguly, R., A.P. Gaind, and I.K. Puri, *A strategy for the assembly of three-dimensional mesoscopic structures using a ferrofluid*. Physics of Fluids, 2005. 17(5): p. 057103-9.
62. Ganguly, R., B. Zellmer, and I.K. Puri, *Field-induced self-assembled ferrofluid aggregation in pulsatile flow*. Physics of Fluids, 2005. 17(9): p. 097104-8.
63. Ganguly, R., et al., *Analyzing ferrofluid transport for magnetic drug targeting*. Journal of Magnetism and Magnetic Materials, 2005. 289: p. 331-334.
64. Chen, H., et al., *Analysis of magnetic drug carrier particle capture by a magnetizable Intravascular stent: 1. Parametric study with single wire correlation*. Journal of Magnetism and Magnetic Materials, 2004. 284: p. 181-194.
65. Chen, H., et al., *Analysis of magnetic drug carrier particle capture by a magnetizable intravascular stent--2: Parametric study with multi-wire two-dimensional model*. Journal of Magnetism and Magnetic Materials, 2005. 293(1): p. 616-632.
66. Xu, H., et al., *Site-directed research of magnetic nanoparticles in magnetic drug targeting*. Journal of Magnetism and Magnetic Materials, 2005. 293(1): p. 514-519.

-
67. Voltairas, P.A., D.I. Fotiadis, and L.K. Michalis, *Hydrodynamics of magnetic drug targeting*. Journal of Biomechanics, 2002. 35(6): p. 813-821.
68. Loukopoulos, V.C. and E.E. Tzirtzilakis, *Biomagnetic channel flow in spatially varying magnetic field*. International Journal of Engineering Science, 2004. 42(5-6): p. 571-590.
69. Tzirtzilakis, E.E. and V.C. Loukopoulos, *Biofluid flow in a channel under the action of a uniform localized magnetic field*. Computational Mechanics, 2005. 36(5): p. 360-374.
70. Khashan, S.A. and Y. Haik, *Numerical simulation of biomagnetic fluid downstream an eccentric stenotic orifice*. Physics of Fluids, 2006. 18(11): p. 113601-10.
71. Jordan, A., et al., *Presentation of a new magnetic field therapy system for the treatment of human solid tumors with magnetic fluid hyperthermia*. Journal of Magnetism and Magnetic Materials, 2001. 225(1-2): p. 118-126.
72. Rosensweig, R.E., *Heating magnetic fluid with alternating magnetic field*. Journal of Magnetism and Magnetic Materials, 2002. 252: p. 370-374.
73. Brusentsov, N.A., et al., *Evaluation of ferromagnetic fluids and suspensions for the site-specific radiofrequency-induced hyperthermia of MX11 sarcoma cells in vitro*. Journal of Magnetism and Magnetic Materials, 2001. 225(1-2): p. 113-117.
74. Raj, K. and R. Moskowitz, *A review of damping applications of ferrofluids*. Magnetics, IEEE Transactions on, 1980. 16(2): p. 358-363.
75. Raj, K. and R. Moskowitz, *Commercial applications of ferrofluids*. Journal of Magnetism and Magnetic Materials, 1990. 85(1-3): p. 233-245.

3 THE DISPERSION OF FERROFLUID AGGREGATES IN STEADY AND PULSATILE FLOWS

3.1 ABSTRACT

Using focused shadowgraphs, we investigate steady and sinusoidal flows of low magnetic susceptibility fluids interacting with ferrofluid aggregates comprised of superparamagnetic nanoparticles. The ferrofluid aggregate is retained at a specific site within the flow channel using a permanent 0.5 Tesla magnet. The bulk flow induces shear stresses on the aggregate, which gives rise to the development of interfacial waves that lead to Kelvin-Helmholtz (K-H) instability. Herein, the effect of Reynolds number and pulsatility are discussed in the context of their impact on the aggregate dispersion.

The study of the ferrofluid aggregate interacting with steady and pulsatile bulk flows reveals three regimes of aggregate stability. Additionally, pulsatility in the flow alters the transition points between the regimes. For steady flows, the first, stable regime is characterized by slight aggregate stretching for Reynolds numbers 100 to 300. At a Reynolds number of 400, the aggregate is in transition between stable and unstable states. Here, significant stretching occurs initially, which gives way to small amplitude Kelvin-Helmholtz waves. Reynolds numbers spanning 600 to 1000 result in large vortical structures that are shed from the main aggregate, and the aggregate decays precipitously. Pulsatility lowers the transitional stability regime to a Reynolds number of 300, and fully unstable aggregates are present at a Reynolds number of 400.

In the final step of this study, the aggregate behavior is characterized by comparing the change in dimensionless parameters relating to aggregate size and properties. For the first time, dimensionless aggregate-based magnetic pressure and time parameters reveal the collapse of aggregate characteristics for unstable aggregates.

3.2 INTRODUCTION

Ferrofluids are stable suspensions of subdomain particles that are strongly magnetized in the presence of a magnetic field. The interaction of ferrofluids with magnetic fields adds a dimension of physics beyond those of conventional fluids and is the basis of the field of ferrohydrodynamics. Some studies of ferrofluids have included those focusing on the apparent change in viscosity of a ferrofluid under a magnetic field [1], or the behavior of these magnetically-susceptible fluids due to changes in magnetic field strength [2]. Moreover, fluid instabilities have been the subject of significant scientific works, including the spike-like protrusions from a ferrofluid free surface known as the normal field instability [3,4], the labyrinthine instability [5], and the Rayleigh-Taylor instability [6]. The Kelvin-Helmholtz instability in ferrofluids has also been studied in a few papers analytically, but has been largely neglected experimentally [7,8].

Ferrofluids have been at the center of many new inventions since the advent of ferrofluid research in the 1960s, including improved dampers and seals [9]. Some of the newest ferrofluid applications have been focused on their integration in a new technique for targeting disease treatment in the human body [10]. Magnetic Drug Targeting (MDT) involves magnetically guiding droplets of a biocompatible ferrofluid bonded reversibly to specific chemotherapeutic agents, which are injected into the blood or lymphatic circulation system [11]. Some trials performed on lab animals have shown that 50% of the typical systemic dose applied to treat cancerous tumors can result in remission of the tumor after only one treatment of anticancer drugs with MDT [12,13,14]. However, in spite of some successes in animal trials, certain MDT studies have yielded inconclusive medical results in clinical trials [15]. Though these studies have provided proof that the MDT application has promise as a clinical modality, only a few physics-based works have examined the interaction of the ferrofluid aggregate with an incident non-magnetic flow to support of the clinical studies. The initial contributions towards the study of ferrofluid-fluid interactions have been published by Ganguly et al [16,17], wherein shadowgraphs were used as a means to analyze the behavior of ferrofluid aggregates as ferrofluid is injected into the test section. One of the primary results obtained from these studies is the periodic shedding or washaway of a ferrofluid aggregate accumulated by a permanent magnet at Reynolds numbers below 400 over several minutes of data acquisition.

Herein, we examine the interaction of a ferrofluid aggregate with a non-magnetic fluid under steady and pulsatile flows for Reynolds numbers ranging between 100 and 1000 using focused shadowgraphs and quantitative flow visualization analysis. The hemispherical-shaped aggregate interacts with the bulk flow similar to a bluff-body inducing shear-layers and generating a wake and vortex shedding. However, since the bluff-body is comprised of a fluid, it deforms dynamically and according to the shear and normal stresses induced by the bulk flow and the magnetic field. The shearing stresses acting on the ferrofluid result in vortex shedding; this in turn affects the stability and retention time of the aggregate. The focused shadowgraphs obtained for all cases were analyzed in terms of the apparent aggregate size and interface positions in time, and the aggregate interface dynamics were further analyzed by means of Proper Orthogonal Decomposition.

This paper will first present the experimental method for collecting the focused shadowgraphs as well as the algorithm for post-processing the raw frames. The aggregate dynamics will be presented separately for steady and pulsatile flows in terms of the evolution of the aggregate over time and Proper Orthogonal Decomposition results obtained for each set of data. Finally, dimensionless parameters used to delineate aggregate behavior will be presented.

3.3 EXPERIMENTAL METHODS

The data were obtained in this experiment by means of focused shadowgraphs, which is a means to qualitatively visualize a flow and is particularly effective when viewing phenomena that involve fluids with distinct density gradients or index of refraction changes, generating a high contrast interface such as that of ferrofluid and water. Illumination for the shadowgraph background was provided by a halogen light source that was directed through spherical and ground glass lenses to illuminate a region of interest with uniform intensity. A 250 Watt bulb was used to create an evenly lit region approximately 20 mm by 150 mm in size, where the experiment was performed in a square channel with a hydraulic diameter, $D_h = 15$ mm. A schematic depicting the setup for the shadowgraph experiments is shown in Figure 3.1.

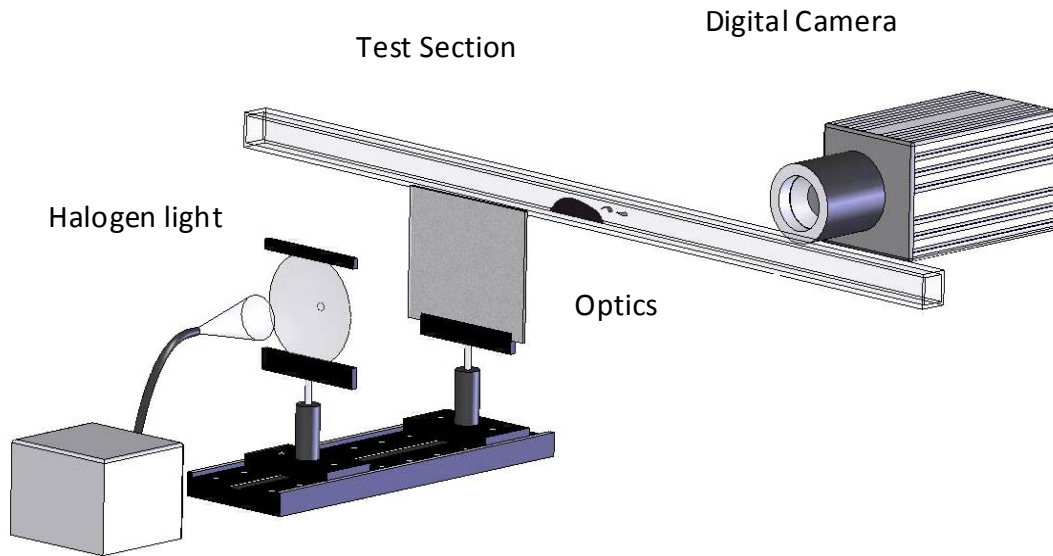


Figure 3.1. Schematic of focused shadowgraph experiment. A high-speed digital camera imaged the side profile of the aggregate.

A digital camera was used to image the side plane of the test section where the ferrofluid aggregate was retained. The image magnification was 63 microns per pixel with an image size of 1020 by 500 pixels. This interrogation region encompassed the channel height as well as $4 D_h$ streamwise. Digital images were sampled at 50 Hz with 3000 total images for each case, corresponding to a real time sampling of 60 seconds. This experiment compares differently to those of Ganguly and colleagues in that herein, the focus was placed on the acute behavior of the aggregate and its interfacial dynamics, whereas previous work has focused on long-term residence time of ferrofluid aggregates.

In each case, a 2 ml volume of ferrofluid (EMG 705, Ferrotec, Inc.) was injected $4 D_h$ upstream of the region of interest before each test in quiescent conditions at a rate of 1 ml per minute. The ferrofluid was diluted to 2% of its original concentration by mixing with water. Injection was facilitated by a needle aligned parallel to the test section walls and mounted flush to the bottom wall of the channel. A KD Scientific 230 syringe pump was utilized for all injection, and its accuracy was estimated to 1% of full-scale volumetric flow. The ferrofluid was captured and retained by a 0.5 Tesla permanent magnet that was obliquely oriented with one of its vertices closest to the test section, resulting in a magnetic field induction of 0.15 Tesla at the inner test section wall. The test section was 1 m long to provide a fully-developed flow for all Reynolds numbers examined in this work. The bulk flow of water was switched on after the

ferrofluid was accumulated and settled, and the flow rate was measured using a Transonic Systems ultrasonic flow meter accurate to 10% of the flow rate for all flow rates. To ensure quasisteady flow conditions, the flow time scale was compared to the time scale of flow acceleration for each test case. The flow time scale is calculated as

$$\tau = \frac{\nu}{U_0^2} \tag{3.1}$$

where ν is the kinematic viscosity, and U_0 is the bulk flow velocity. Using standard properties of water, the time scales range between 0.02 to 2×10^{-4} seconds. Flow was ramped up over 0.1 seconds, which ensured quasisteady acceleration.

Aggregate dynamics were studied in both steady and pulsatile bulk flows. Pulsatile flow in the form of a sine wave with an offset such that its lowest point passes through zero flow was tested. The sine wave pulsation frequency was selected to be 0.3 Hz to visualize the structure development of the shedding aggregate. Based on this pulsation frequency, the Womersly number for this experiment is 9.6. The average flow velocity for steady flows is used as the basis for the Reynolds number along with D_h . The pulsatile flows were created such that they have the same average flow rate and as a result, the same average Reynolds number, Re_{av} , as steady flows. Both steady and pulsatile flows were examined over a range of Reynolds numbers spanning between 100 and 1000.

3.4 PROPER ORTHOGONAL DECOMPOSITION OF DETECTED INTERFACES

The raw frames obtained by the focused shadowgraph technique were post-processed to determine the aggregate evolution in time as well as to detect the time-varying interface between the ferrofluid aggregate and bulk flow. A sample image showing the transformation from the original grayscale frame to the detected interface is shown in Figure 3.2. The interface between the ferrofluid and water was sampled for each snapshot of the flow using software written in-house in conjunction with the MATLAB Image Processing Toolbox. The grayscale images were converted to black and white using Otsu’s grayscale thresholding algorithm [18].

Otsu's method assumes uniform image illumination and a bimodal image histogram, which separates foreground and background. The result of this thresholding is utilized to create a binary image. Regions of connected pixels in the binary images were identified and sorted by size for each frame, which generally represent the ferrofluid aggregate or vortex shedding. The size of the aggregate was obtained using this method by selecting the largest region, which was confirmed through an output of a binary image. The aggregate size, measured from the binary images, was corrected by weighting with the grayscale intensity of the pixels in the region of the aggregate. The intensities account for the local ferrofluid concentration and correct the aggregate size by up to 10%. Pixel intensities are a factor when calculating the time-rate of dispersion, particularly as the aggregate stretches. The variation in initial aggregate size is 5% across all cases. In addition, the random error in the aggregate size is +/- 0.5%, measured between two successive frames for an aggregate of ferrofluid retained in quiescent flow.

The binary images were then used to obtain a line representing the detected interface between the aggregate and bulk flow. The edge obtained from the binarized aggregate is zero-padded to obtain a set of arrays of the same length. These arrays were compiled for each case over all time snapshots and become the input for the Proper Orthogonal Decomposition (POD).

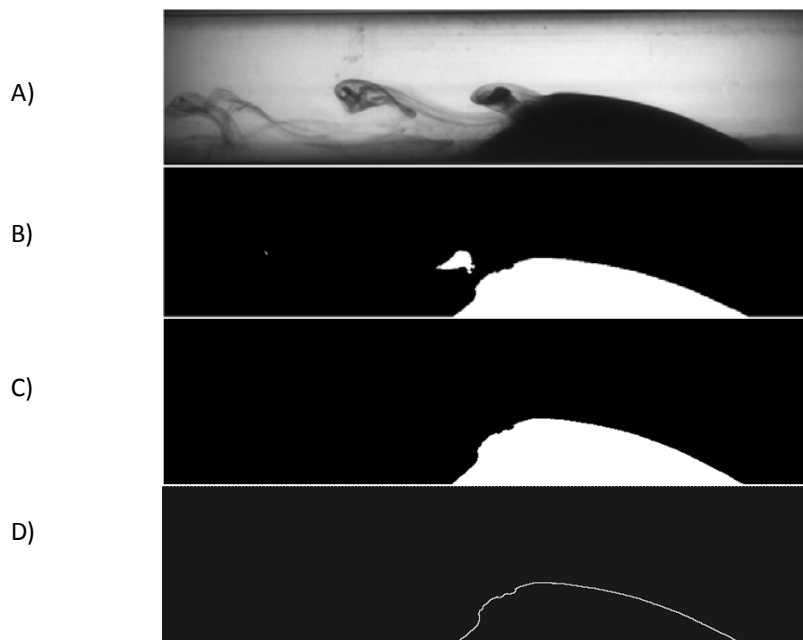


Figure 3.2. The image processing used to transform a grayscale image to a region corresponding to the instantaneous aggregate size (C) and the detected edge of the aggregate (D).

The Proper Orthogonal Decomposition or Karhunen Lo'ève Decomposition is a means to decompose a flow field or, in this experiment, interface, into its fundamental components using orthonormal basis functions. The basis functions are mathematically selected based on the degree to which they efficiently describe the data. The modes are ordered from highest energy in the first mode to lowest in the last mode, and based on the energy captured by the lower modes, reduced-order models can be developed to describe complex systems.

The detected edges $Y(x,t)$ are decomposed into modes with corresponding coefficients, which, when recombined, have the form

$$y(x,t) = \sum_{i=1}^N \alpha_i(t) \phi_i(x) \quad 3.2$$

where α_i are the projection coefficients which describe the time history of the mode shapes, ϕ_i . POD has been used as tool for studying turbulence [19,20], performing image analysis [21], and even for studies of MEMS [22]. A comprehensive review of the POD technique and applications is given by Berkooz et al [23]. POD results are useful to describe the flow energetics or interactions between the different modes. Calculating the number of modes required to reconstruct the interface indicates the organization of the system and it will be referred to from hereon as the dimension. This reconstruction is determined by comparing the summation of a specific number of modes, m , to the cumulative sum of all modes, N , written as

$$E_m = \frac{\sum_1^m \lambda_n}{\sum_1^N \lambda_n} \quad 3.3$$

where λ_n is the expected absolute value of the squared POD reconstruction. Herein, a separate way to calculate the energy reconstruction is used to reveal additional dynamics that would otherwise not be evident. As we will show in later sections, the first POD mode for all cases contains most of the energy. Therefore, additional physics may be revealed by removing the first mode from the summation and examining the remaining energy less the first mode. Then, the energy is based on all remaining modes and the result of this energy ratio will be referred to as E_m^* , which is written as

$$E_m = \frac{\sum_2^m \lambda_n}{\sum_2^N \lambda_n}$$

3.4

3.5 EFFECT OF THE REYNOLDS NUMBER ON AGGREGATE STABILITY

The large-scale changes of the aggregate for steady flows are characterized by three primary regimes: stable, transitional, and unstable. These regimes will first be described qualitatively, and will then be described quantitatively using aggregate sizing information. Based on the authors observations, in steady flows for Reynolds numbers below 400, slight aggregate stretching occurs, and the aggregate shears downstream. For a Reynolds number of 400, stretching occurs initially, but the stretching overcomes the magnetic body forces, since the aggregate expands beyond regions of high magnetic field gradients wherein it can be controlled by the magnet. The stretching leads to the destabilization of the aggregate, and ferrofluid is shed. As the Reynolds number is increased to 500 or greater, the Kelvin-Helmholtz instability occurs and the aggregate decays rapidly as vortices containing ferrofluid are shed from the aggregate. A representative set of shadowgraph images corresponding to flow at a Reynolds number of 600 is shown in Figure 3.3. In Figure 3.3 at $t = 0$ seconds, the aggregate is initially at rest, giving way to vortex shedding in Figure 3.3 at $t = 25$ seconds. Finally, Figure 3.3 at $t = 50$ seconds shows the reduction in intensity of the shedding as the aggregate size decreases.

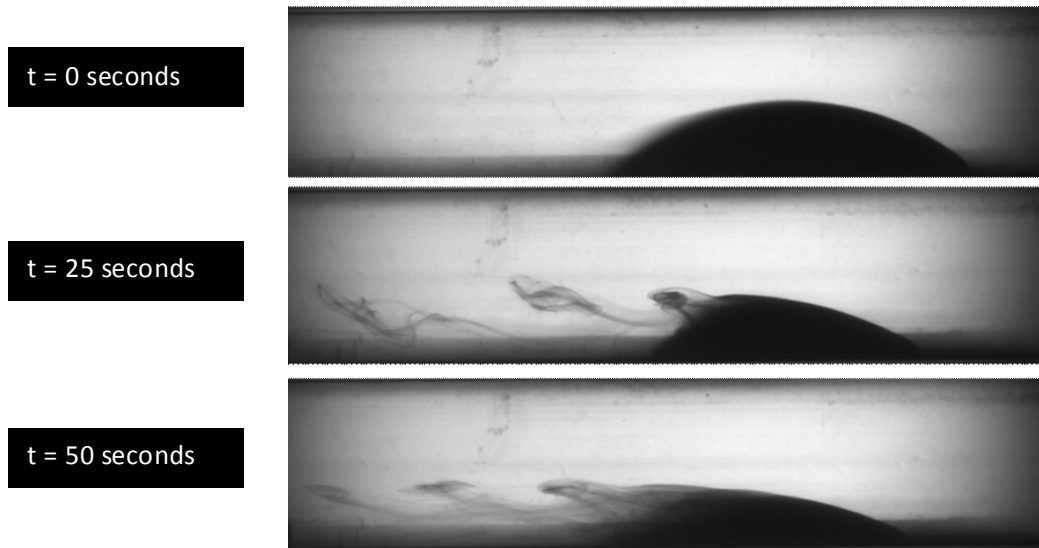


Figure 3.3. Shadowgraph images for three time instants of 0, 25, and 50 seconds for steady flow with a Reynolds number of 600. Kelvin-Helmholtz shedding occurs in the later part of the time series, and degrades as the aggregate begins to wash away.

For all ten cases in steady flow, the relative size of the aggregate is plotted versus time in Figure 3.4. The dispersion was calculated as the normalized sum of the number of pixels in the edge-detected aggregate with respect to the initial aggregate size, a_i . The normalization using the initial aggregate size takes into account the slight discrepancies in the initial volume of ferrofluid retained by the magnet and provides an indication of the relative change in aggregate size over time. When the Reynolds numbers are lower than 400, a slightly upward sloping line indicates aggregate stretching due to shearing stresses. The total percent stretching increases from 3.8 to 6.3, and finally 8% for Reynolds numbers between 100 and 300. For a Reynolds number of 400, a conspicuous increase in the aggregate size occurs initially, stretching up to 14% at 25 seconds. After this point, wisps of ferrofluid are shed from the aggregate, and the aggregate begins dispersing so that at the end of data acquisition the apparent size ratio reduces to only 1% more than its starting value. As the Reynolds number is increased to 500 or greater, the initial stretching of the aggregate occurs rapidly, within the first seconds of flow ramp-up. After the initial stretching, the aggregate destabilizes and decays exponentially for the remainder of the acquisition time as vortex shedding occurs at the interface between the aggregate and bulk flow.

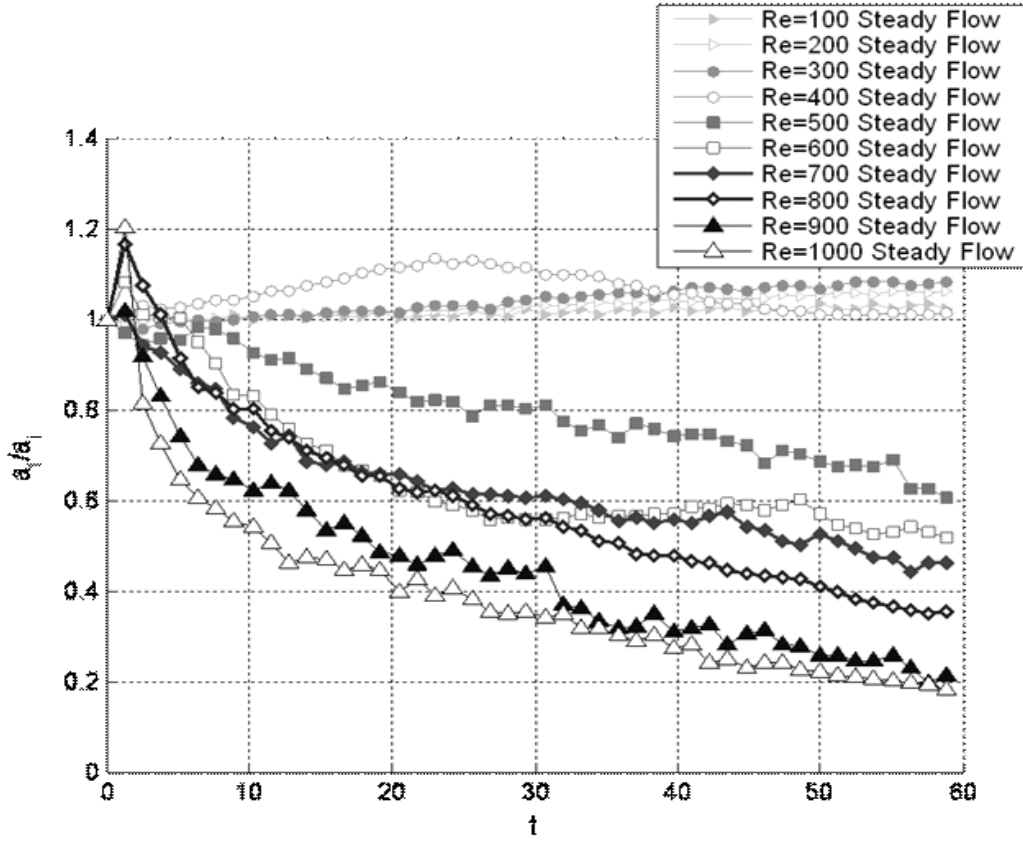


Figure 3.4. Plot of the apparent ferrofluid aggregate size as a function of time in steady flow conditions. Rapid aggregate decay occurs for Reynolds numbers 500 and greater, driven by the shedding resulting from the K-H instability.

The POD spatial mode shapes of the interface are shown for the first five modes for a Reynolds number of 400 in Figure 3.5. The first mode represents the stable, hemispherical outline of the aggregate. Higher modes show perturbations of the interface between the aggregate and water that correspond to the waves that develop on the interface as a precursor to the Kelvin-Helmholtz instability.

The number of modes to obtain the dimension of the POD results, or the threshold to reach 99.5% of the energy, was calculated two ways as described in Equations 3.2 and 3.3. The result of E_m (fundamental mode included) and E_m^* (fundamental mode neglected) calculations for steady flow cases are shown as a function of the Reynolds number in Figure 3.6. The black squares indicate the number of modes needed for reconstruction considering the entire set of eigenmodes, E_m . Examining the dimension of these interfaces when including all modes, an increase in the number of modes required to attain the energy threshold occurs as the Reynolds

number increases. The increase indicates that the interface is less organized and stable as the Reynolds number increases, which was observed in the flow visualization. At the transition point of 400, the jump in the number of modes for E_m shows the spreading of the energy to higher order modes and also indicates interface destabilization. In all cases, the first mode is dominant, representing 80% or more of the total energy of the interface. Therefore, by removing it, the effect of the higher order modes can be observed readily.

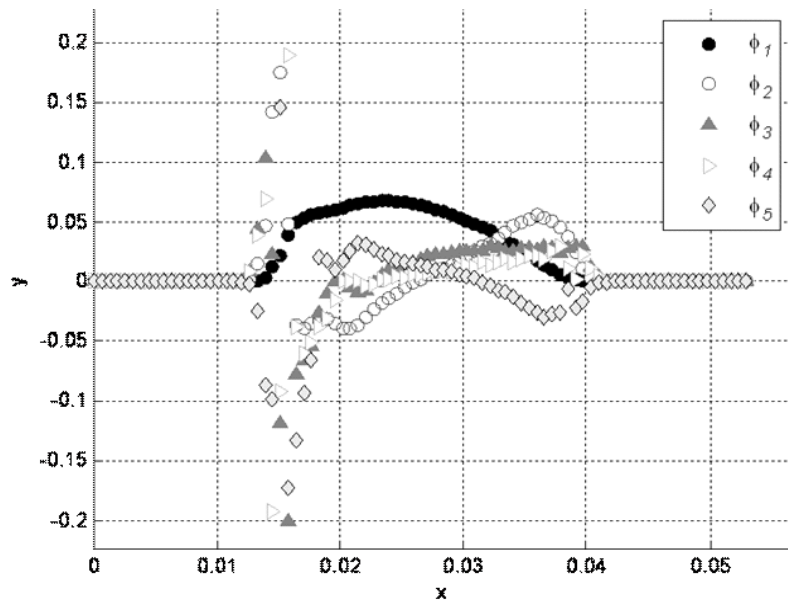


Figure 3.5. Plot of the first five modes of the aggregate for a Reynolds number of 400 in steady flow.

In Figure 3.6, the gray circles show the number of modes needed to reconstruct 99.5% of the energy when the first mode is removed from the summation, E_m^* . When the first mode is removed, the distinct appearance of stable and unstable aggregate regimes can be observed. For Reynolds numbers 100 to 300, the number of modes required to reconstruct 99.5% of the remaining energy increases to nearly 300 for these three cases compared to one mode for E_m . The significant increase in modes required reiterates that at these Reynolds numbers, the aggregate is stable and the fundamental mode is the most dominant. For a Reynolds number of 400 with E_m^* , a drop in the number of modes to describe the interface occurs, confirming that the energy is being transferred to higher modes.

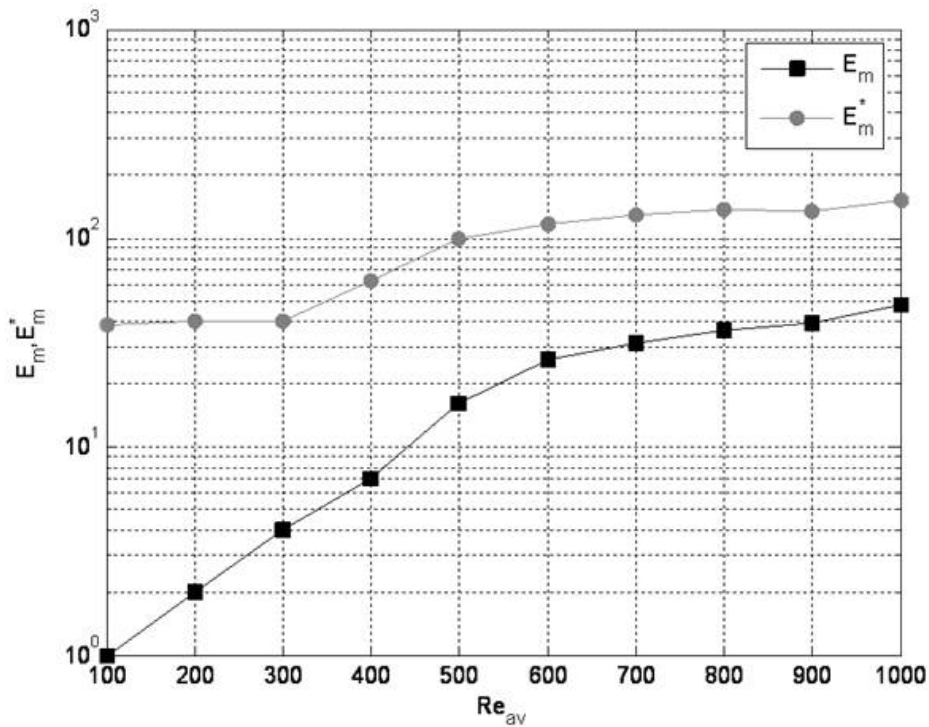


Figure 3.6. POD dimension for 99.5% energy reconstruction as a function of the Reynolds number for steady flow.

3.6 EFFECT OF PULSATILITY ON AGGREGATE STABILITY

For pulsatile flow, the three-regime behavior is present as in steady flows, but the pulsatile flow induces additional periodic deformations of the aggregate that modify its overall dynamics. Qualitatively, at Reynolds numbers below 300, the aggregate is observed to oscillate about the magnet location, but the aggregate remains stable. One key difference between pulsatile flows and steady flows is that the average Reynolds number where the transition between stable and unstable aggregates occurs is lower, dropping to 300 from 400. At Reynolds numbers of 400 or higher, the aggregate is unstable and K-H shedding occurs. A representative sequence showing a period of pulsatile flow for Re_{av} of 600 is shown in Figure 3.7. The bulk flow rate is zero at time $t = t_0$. As the flow increases, a visible wave disturbance develops that result in K-H rolls as the flow rate increases to its highest level. For decreasing flow rates, the aggregate restabilizes at the end of one period.

Quantitative results are obtained by examining the apparent aggregate size ratio, which is plotted for all pulsatile Reynolds numbers in Figure 3.8. For average Reynolds numbers between 100 and 200, the time-averaged aggregate size is nearly constant at a value of 1 through each of these cases. This correlates to the aggregate responding only slightly to the changes in flow rate. Once Re_{av} reaches 300, the aggregate begins to transition to K-H shedding. The lower transition point is due to the pulsatility of the flow acting to displace the ferrofluid away from regions of strong magnetic field strength. The shedding strengthens as the Reynolds number is increased further, and is evidenced by the high stretching observed in the first part of the time series. As the average Reynolds number is increased to 800 and above, the slope of the curve flattens to near zero at the end of the case, and the oscillations in a/a_i are damped out. The flattening of the curve describes how the high shearing of flows with Re_{av} between 800 and 1000 erode the aggregate to the point where its height is insufficient to interact significantly with the pulsatile flow.

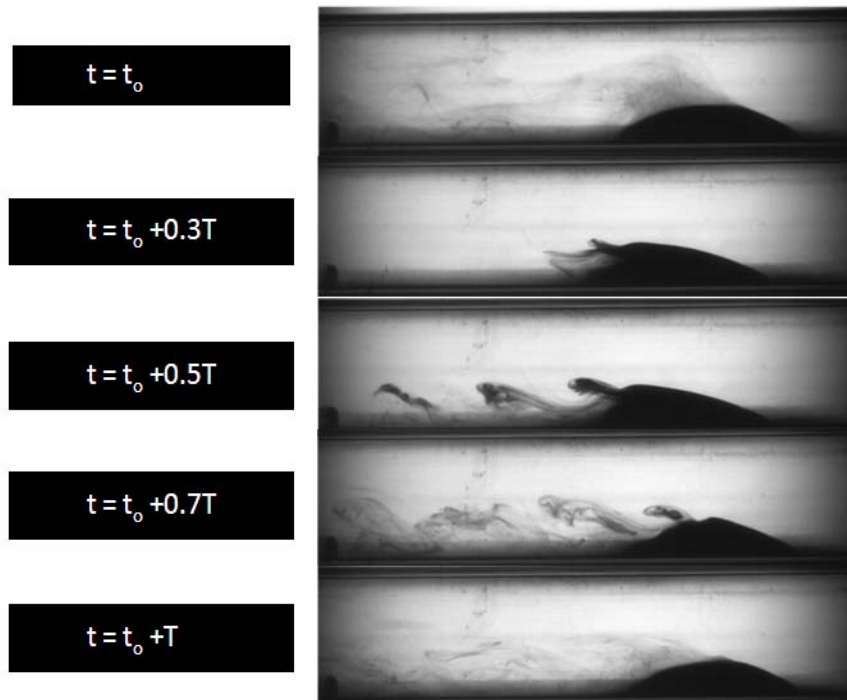


Figure 3.7. A sequence of images for sinusoidal pulsatile flow with an average Reynolds number of 600.

The POD results for pulsatile flow illustrate some of the same physics that were observed using this decomposition in steady flow, including similar mode shapes. The dimensions of the

POD modes are shown in Figure 3.9 for all sinusoidal pulsatile cases. The black squares, showing the calculated energy E_m , indicate that more modes are needed to reconstruct the interface as the Reynolds number is increased, as was observed in steady flow. The results for E_m^* show that at 300 and below, a constant number of modes are needed to describe the interface. At Re_{av} of 400, the induced K-H shedding causes an increase in the number of modes needed to reconstruct the interface. A change in slope of the dimension for E_m and E_m^* occurs as the Reynolds number is increased beyond 600. These Reynolds numbers show similar responses to pulsatility in terms of the decay rate of the aggregate; therefore it is not counterintuitive that a similar dimension would be obtained. Increases for both E_m and E_m^* , however, is indicative that once the aggregate is unstable, further growth of the instabilities at the interface is dependent on Re_{av} , although the instability growth is limited as the Re_{av} is increased far past the point of transition.

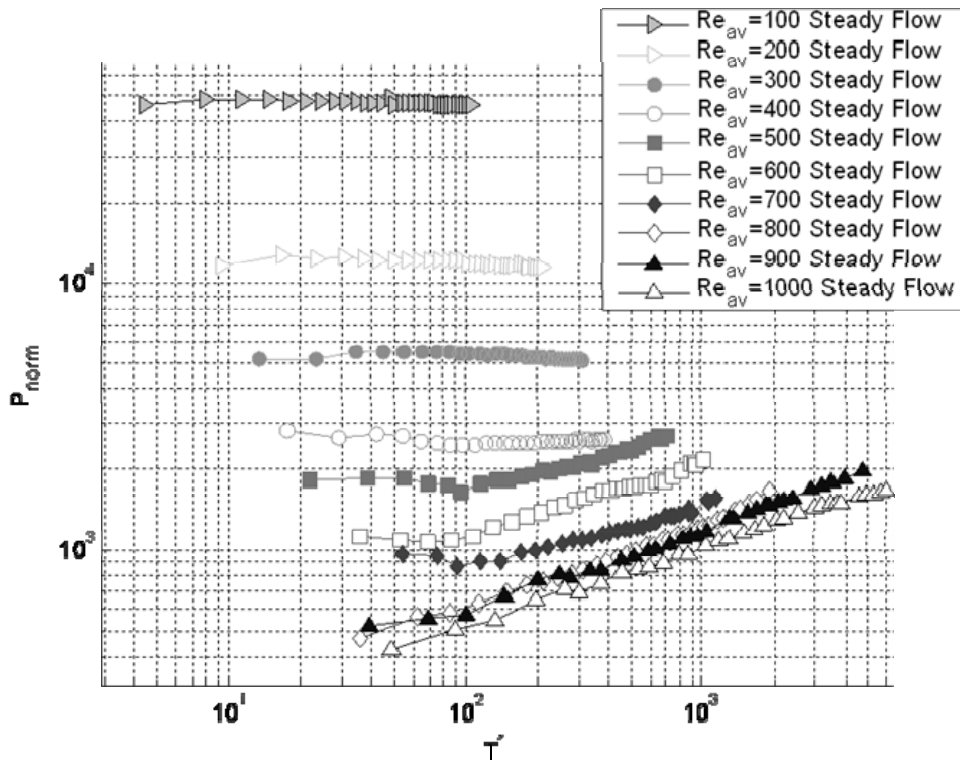


Figure 3.8. Plot of the decrease in apparent ferrofluid aggregate volume as a function of time for a sinusoidal pulsatile flow.

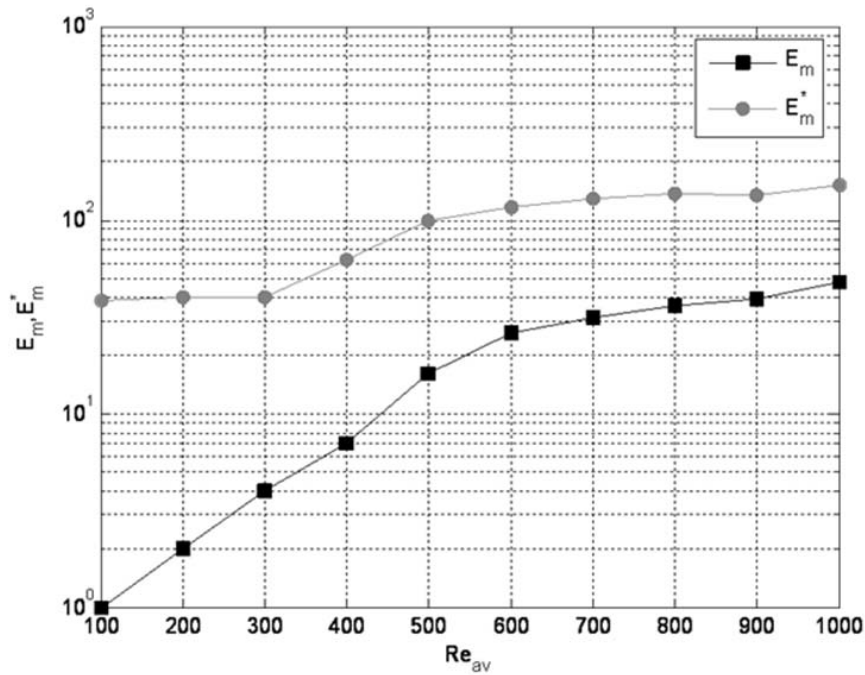


Figure 3.9. POD dimension to reconstruct 99.5% of the total energy in pulsatile flow.

3.7 DISCUSSION

Dimensional analysis using the Pi-theorem was performed with the parameters t , h , U , B , and ρ . The density and magnetic permeability of this system can be considered constant since the ferrofluid is a 2% dilution in water, and the specific gravity of pure ferrofluid is 1.19. Therefore, we can assume that the apparent properties of the mixture would be very close to those of water. From this analysis, we derive aggregate-based Reynolds numbers, as well as a magnetic pressure ratio that compares magnetic to dynamic pressures and two dimensionless time scaling parameters. Plotting the data using these dimensionless parameters, and performing power law curve fits allows for consolidating the data and revealing any underlying physical scaling relationships. Error bars are applied to the curve fit coefficients using the method of Kline and McClintock, which was performed on the parameters plotted for each curve fit.

The normalized pressure versus dimensionless time plots are shown for steady and pulsatile flow in Figure 3.10 and Figure 3.11, respectively. The normalized pressure term is written as

$$P_{norm} = \frac{B_z^2}{\rho\mu U_s^2} \quad 3.5$$

where B_z refers to the magnetic field induction calculated at the aggregate interface with the bulk flow. This quantity is calculated by characterizing the magnetic field with a Gauss meter and using the edge detection analysis to obtain the changing aggregate height in time. The shear velocity, U_s , is calculated using continuity and comparing the velocities of the incoming bulk flow before the aggregate blockage, U_o , with the shear velocity flowing over the aggregate at height h . The shear velocity and aggregate height also factor into a dimensionless time parameter, T^* , which is defined as

$$T^* = \frac{U_s t}{H} \quad 3.6$$

where t is the time in seconds. In Figure 3.10 and Figure 3.11, distinct separations between stable and unstable aggregates are indicated. For stable aggregates at bulk flow Reynolds numbers from 100-300 in steady flow and 100-200 in pulsatile flow, the relationship between the normalized pressure and T^* plots as a straight line, as the aggregate does not change height, and therefore the magnetic field at the interface remains constant. As the aggregate destabilizes, a nonlinear relationship arises between the magnetic pressure and dimensionless time. The increase in normalized pressure is a result of the aggregate height decaying, which in turn causes the magnetic field induction to increase at the aggregate interface location. The destabilized aggregates follow similar slopes as they drop off, and the similarity of the curves increase as the Reynolds number is increased up to 1000 for both steady and pulsatile flows. Plotting other dimensionless parameters including the aggregate-based Reynolds number illustrate similar qualitative patterns for steady and pulsatile flows.

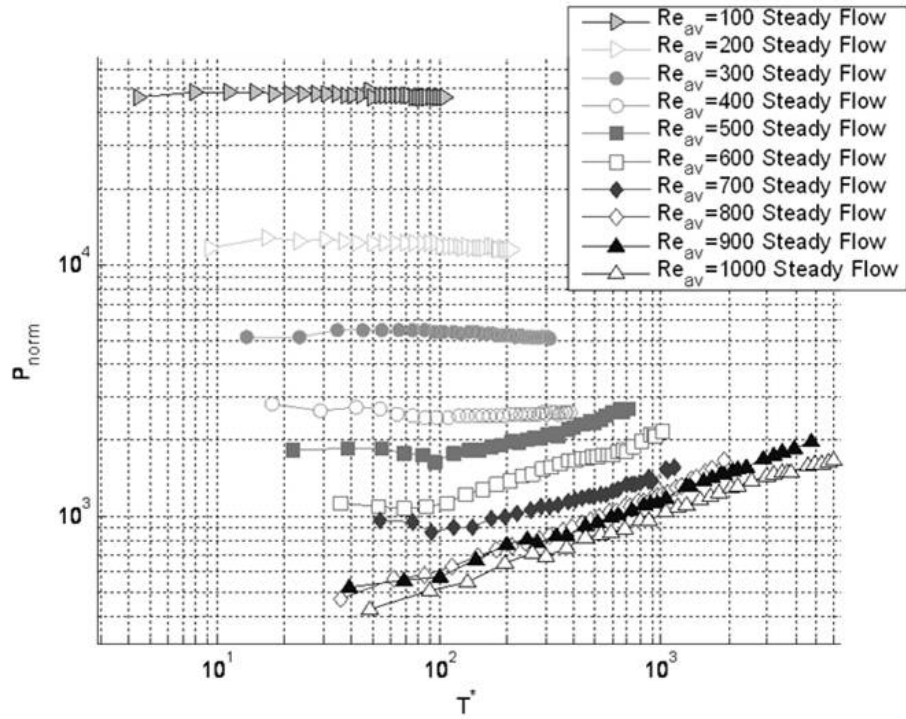


Figure 3.10. Normalized pressure versus dimensionless time for steady flow cases with bulk flow Reynolds numbers between 100 and 1000.

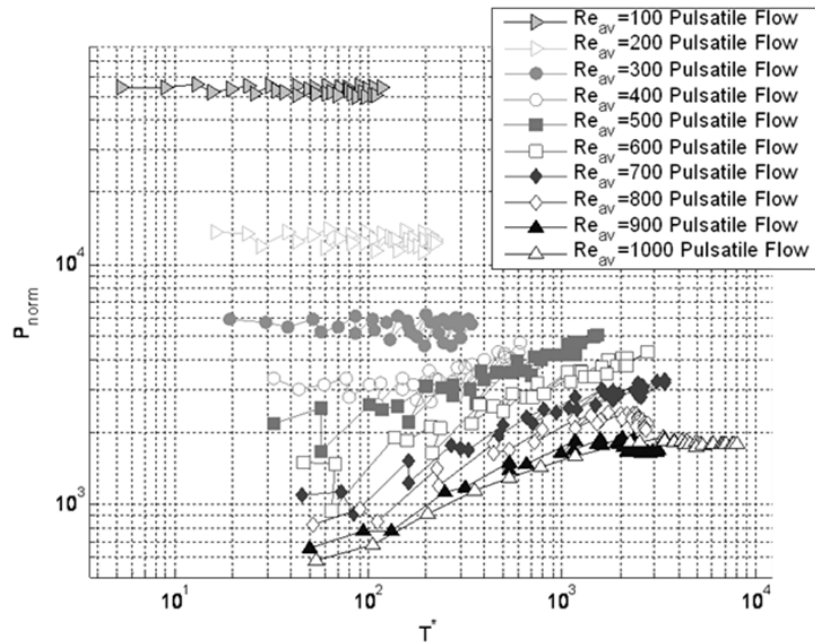


Figure 3.11. Normalized pressure versus dimensionless time for pulsatile flow cases with bulk flow Reynolds numbers between 100 and 1000.

A first order power law curve fit was performed on the plots in Figure 3.10 and Figure 3.11 to characterize the decay rate in time based on the Reynolds number. The results of this curve fit plotted as a function of the bulk flow Reynolds number are shown in Figure 3.12 and each curve fit has an R^2 value of 0.90 or higher. The exponent is very small for the stable cases, since aggregates in these cases do not decay significantly. An increase in the exponent for Reynolds numbers above 300 in pulsatile flow and 400 in steady flow indicate an increase in P_{norm} corresponding to incipient instability of the aggregate. The exponent increases in both steady and pulsatile flows as the aggregate erodes. Once high Reynolds numbers of 700 or greater are reached, however, a divergence in the qualitative behavior of steady and pulsatile flows occurs. Referencing back to the aggregate size graphs in Figure 3.4 and Figure 3.11, the highest Reynolds numbers in steady flows produce an aggregate that follows a clear exponential decay, similar to that of the lower Reynolds numbers of 500-900. However, these high Reynolds numbers are also accompanied by a steeper initial decay of the aggregate, corresponding to the increase in exponent for the pulsatile flow cases. However, for pulsatile flow, the higher Reynolds numbers of 700 and larger result in dramatic decay of the aggregate as flow ramps up to its highest levels, much more so than for steady flow due to the high peak velocities encountered in pulsatile flow. Therefore, the exponent values decrease, and the constants increase. The results illustrate that different Reynolds numbers are described by different rates of decay based on the aggregate regime, as well as the overall complexity of the aggregate behavior.

The power law relationship for aggregate behavior was first introduced by Ganguly, Zellmer, and Puri [24] in an experiment where a ferrofluid aggregate accumulated and dispersed under pulsatile flows. The maximum aggregate size, time to maximum aggregate size, and half life were written as functions of the bulk flow Reynolds number, where the mean Reynolds number was varied between 170 and 382. Overall, the aggregate half-life that they predicted estimates that the aggregates will remain in residence at the magnet for a shorter period than observed herein in cases where at least 50% of the aggregate decays over 60 seconds of acquisition. However, the Reynolds numbers during which we observe such decays are much higher than those studied previously, and these introduce the K-H instability. The results obtained in the present effort hardly invalidate those of the previous investigation, as different magnetic field gradients, channel cross-section, aggregate heights, and acquisition times were employed.

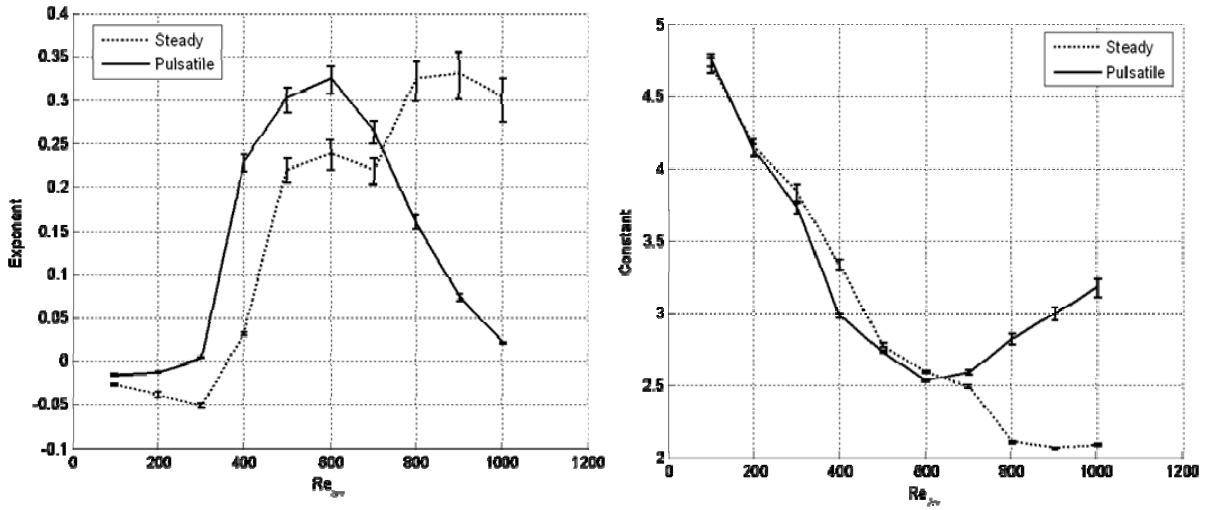


Figure 3.12. Exponent (left) and constant (right) plotted for Reynolds numbers 100-1000 for the normalized pressure versus T^* . The gray line indicates the results of a polynomial fit of these constants and exponents based on the bulk flow Reynolds number.

3.8 CONCLUSIONS

The behavior of ferrofluid aggregates were studied herein for steady and pulsatile flow conditions over a range of Reynolds numbers spanning 100 to 1000. Several conclusions about the stability and residence time of ferrofluid aggregates can be drawn from the results. First, in steady flow, three regimes appear for flows of Re_{av} between 100 and 1000. Reynolds numbers between 100 and 300 result in a stable aggregate that stretches by up to 8%. At 400, the aggregate stretches significantly, causing the aggregate to lose coherence as it expands away from the magnet. The decreased magnet influence results in destabilization of the aggregate. Further increase of the Reynolds number results in Kelvin-Helmholtz shedding from the main aggregate and aggregate erosion of up to 80 percent over 60 second data acquisition.

In pulsatile flow, the transition to Kelvin-Helmholtz shedding drops to an average Reynolds number of 300 from 400 in steady flow due to flow peaking. The flow pulsatility also causes a more rapid initial dispersion of the aggregate, decaying the aggregate to a size where it interacts to a lesser degree with the bulk flow. Aggregates in steady flow do not decay as rapidly initially and therefore interact with higher shearing forces in the freestream for a longer period of time. This causes the gap between the total decay of the aggregate for steady and pulsatile flows to

increase for higher Reynolds numbers where dispersion is significant. An examination of relevant nondimensional parameters indicates that power law relationship governs the aggregate dynamics for the Reynolds numbers investigated herein, and the power law coefficients vary widely based on the Reynolds number of the bulk flow, and as a result the widely varying behavior of the aggregate.

3.9 REFERENCES

1. Bacri, J.C., et al., *Negative-Viscosity Effect in a Magnetic Fluid*. Physical Review Letters, 1995. 75(11): p. 2128.
2. Shliomis, M.I., *Ferrohydrodynamics: Testing a third magnetization equation*. Physical Review E, 2001. 64(6): p. 060501.
3. Boudouvis, A.G., et al., *Normal field instability and patterns in pools of ferrofluid*. Journal of Magnetism and Magnetic Materials, 1987. 65(2-3): p. 307-310.
4. Abou, *The Normal Field Instability in Ferrofluids: hexagon-square transition mechanism and wavenumber selection*. Journal of Fluid Mechanics, 2000. 416: p. 217-237.
5. Zahn, M. and R. Rosensweig, *Stability of magnetic fluid penetration through a porous medium with uniform magnetic field oblique to the interface*. Magnetics, IEEE Transactions on, 1980. 16(2): p. 275-282.
6. Pacitto, G., et al., *Rayleigh-Taylor instability with magnetic fluids: Experiment and theory*. Physical Review E, 2000. 62(6): p. 7941.
7. Moatimid, G., *Nonlinear Kelvin-Helmholtz instability of two miscible ferrofluids in porous media*. Zeitschrift für Angewandte Mathematik und Physik (ZAMP), 2005. 57(1): p. 133-159.
8. Malik, S.K. and M. Singh, *Finite amplitude Kelvin--Helmholtz instability in magnetic fluids*. Physics of Fluids, 1986. 29(9): p. 2853-2859.
9. Raj, K. and R. Moskowitz, *A review of damping applications of ferrofluids*. Magnetics, IEEE Transactions on, 1980. 16(2): p. 358-363.
10. Alexiou, C., et al., *Locoregional Cancer Treatment with Magnetic Drug Targeting*. Cancer Research, 2000. 60(23): p. 6641-6648.
12. Alexiou, C., et al., *Magnetic drug targeting: biodistribution and dependency on magnetic field strength*. Journal of Magnetism and Magnetic Materials, 2002. 252: p. 363-366.
13. Lubbe, A.S., C. Alexiou, and C. Bergemann, *Clinical Applications of Magnetic Drug Targeting*. Journal of Surgical Research, 2001. 95(2): p. 200-206.

-
14. Alexiou, C., et al., *Magnetic mitoxantrone nanoparticle detection by histology, X-ray and MRI after magnetic tumor targeting*. Journal of Magnetism and Magnetic Materials, 2001. 225(1-2): p. 187-193.
 15. Lubbe, A.S., et al., *Clinical Experiences with Magnetic Drug Targeting: A Phase I Study with 4'-Epidoxorubicin in 14 Patients with Advanced Solid Tumors*. Cancer Research, 1996. 56(20): p. 4686-4693.
 16. Ganguly, R., et al., *Analyzing ferrofluid transport for magnetic drug targeting*. Journal of Magnetism and Magnetic Materials, 2005. 289: p. 331-334.
 17. Ganguly, R., A.P. Gaiind, and I.K. Puri, *A strategy for the assembly of three-dimensional mesoscopic structures using a ferrofluid*. Physics of Fluids, 2005. 17(5): p. 057103-9.
 18. Otsu, N., *A Threshold Selection Method from Gray-Level Histograms*. IEEE Transactions on Systems, Man, and Cybernetics, Vol. 9, No. 1, 1979, pp. 62-66.
 19. R. E. A. Arndt, D. F. Long, and M. N. Glauser, *The proper orthogonal decomposition of pressure fluctuations surrounding a turbulent jet*. Journal of Fluid Mechanics, 1997. 340: pp 1-33.
 20. Sirovich, L., K.S. Ball, and L.R. Keefe, *Plane waves and structures in turbulent channel flow*. Physics of Fluids A: Fluid Dynamics, 1990. 2(12): p. 2217-2226.
 21. Kirby, M. and L. Sirovich, *Application of the Karhunen-Loeve procedure for the characterization of human faces*. Transactions on Pattern Analysis and Machine Intelligence, 1990. 12(1): p. 103-108.
 22. Hung, E. S. and S. D. Senturia, *Generating efficient dynamical models for microelectromechanical systems from a few finite-element simulation runs*. Journal of Microelectromechanical Systems, 1999. 8(3): 280-289.
 23. Berkooz, G., P. Holmes, and J.L. Lumley, *The Proper Orthogonal Decomposition in the Analysis of Turbulent Flows*. Annual Review of Fluid Mechanics, 1993. 25(1): p. 539-575.
 24. Ganguly, R., B. Zellmer, et al. *Field-induced self-assembled ferrofluid aggregation in pulsatile flow*. Physics of Fluids, 2005. 17(9): 097104-8.

4 THE EFFECT OF ORTHOGONAL MAGNETIC FIELDS ON FERROFLUID AGGREGATE DYNAMICS

4.1 ABSTRACT

Ferrohydrodynamics studies have spanned many of the physical phenomena associated with ferrofluids, including the normal field instability, labyrinthine instability, and the Kelvin-Helmholtz (K-H) instability. Such works have primarily examined how magnetic fields applied tangentially with respect to the interface of the ferrofluid with another, usually non-susceptible fluid, can act as a mechanism to prevent the development of instabilities. Although many investigations both experimentally and analytically addressed most of these instabilities, the K-H instability in ferrofluids has been examined largely to date from an analytical perspective. The objective of the work presented herein is to experimentally investigate the behavior of an aggregate of ferrofluid under the shear flow of a low susceptibility liquid that is subjected to the application of orthogonally-oriented magnetic field gradients.

Focused shadowgraph experiments are undertaken in which the side profile of a volume of ferrofluid retained by a 0.5 Tesla permanent magnet is captured for test cases in which the Reynolds number was varied from 200 to 1000. At certain bulk flow Reynolds numbers, the aggregate shearing reaches a point to which the magnetic body forces can no longer maintain a cohesive aggregate, and Kelvin-Helmholtz shedding occurs, resulting in exponential aggregate wash away. We experimentally show that increasing the magnetic field gradients effectively lowers the bulk flow Reynolds number at which the transition to K-H shedding is observed. This is in agreement with previous works of stability analysis previously performed for ferrofluids.

4.2 INTRODUCTION

Ferrohydrodynamics consists of studies of the mechanics and instabilities associated with ferrofluids. Ferrofluids are stable colloids comprised of suspended subdomain particles that can be strongly magnetized in the presence of a magnetic field, while remaining stably suspended.

Instabilities in ferrofluids have been the subject of significant scientific work over the past 40 years, including examinations of the spike-shaped protrusions that develop in ferrofluid free surfaces under the application of a magnetic field known as the normal field instability. The normal field instability arises due to an interaction between surface tension forces and magnetic forces acting on a ferrofluid when the applied field is oriented orthogonally to its free surface. One of the first studies of the normal field instability described critical magnetic field strengths for instability onset and spacing of such peaks [1]. Recent studies indicate that the normal field instability has different states based on experimental conditions, shifting from hexagonal-shaped peaks to square peaks [2].

The labyrinthine instability in ferrofluids is found in Hele-Shaw cell configurations, wherein an initially quiescent droplet of ferrofluid confined within two plates deforms, with ferrofluid fingers radiating outward from the primary droplet. Rosensweig, Zahn, and Shumovich showed that the shape contours depend on both the intensity of the magnetic field as well as the spacing of field lines [3]. The stabilization of the droplet by a tangentially-applied magnetic field acting parallel to the span of the Hele-Shaw plates was shown both experimentally and analytically by Zhan and Rosensweig [4].

The Kelvin-Helmholtz (K-H) instability in ferrofluids has also been studied analytically, but few related experiments have been undertaken. In an ordinary system of two parallel-flowing non-magnetic fluids, the K-H instability results from shearing that acts on a plane interface. When that system includes a ferrofluid, the instability may be mediated or agitated based on the orientation of an applied magnetic field, as previously observed for other fluid instabilities. Malik and Singh examined the instability of two parallel-flowing magnetic fluids with a magnetic field acting parallel to the interface of the two [5]. Based on linear theory and the dispersion equation described by Rosensweig, Malik and Singh showed that the flow between two magnetic fluids may be amplified to a higher speed before the onset of instability due to the stabilizing effect of the tangentially-applied field.

Miranda and Widom numerically investigated ferrofluid flowing in parallel with a non-magnetic fluid [6]. Three different orientations of an applied magnetic field were studied numerically, with tangential, orthogonal, and perpendicular placement with respect to the major dimension of the Hele-Shaw cell. The authors showed that with no applied magnetic field, the interface between the ferrofluid and non-magnetic liquid is damped and stable. However, under the application of a magnetic field, the interface may be stabilized or

destabilized depending on the direction of application. Similar to the findings of Malik and Moatimid, Miranda and Widom found that tangentially-applied magnetic fields act to stabilize the interface against the K-H instability, as these fields act as an effective boost of surface tension and gravitational effects. Both normal and perpendicularly oriented fields, however, foster destabilization.

Recently, the authors have been working to develop understanding of the physics of ferrofluid aggregates under a wide range of conditions [7,8]. Using both the focused shadowgraph and Time Resolved Particle Image Velocimetry (TRDPIV) techniques, ferrofluid aggregate dynamics have been characterized in both steady and unsteady flows in dispersing conditions. This work seeks to discuss the physics that arise under the application of different magnetic field strengths directed orthogonally to retain an aggregate of ferrofluid under shear by an incident bulk flow. Focused shadowgraphs that were obtained for several different steady bulk flows were analyzed in terms of the apparent aggregate size in time. Moreover, the interface between the aggregate and water was decomposed using the Proper Orthogonal Decomposition (POD) to couple the bulk aggregate dynamics with those of the interface itself.

4.3 EXPERIMENTAL METHODS

The data in this work was obtained by means of focused shadowgraphs, which is effective when viewing phenomena with a high contrast interface, as is the case with water flowing past aggregates of opaque ferrofluid. A diffuse light source that illuminated the region of interest within the test section was created by directing a halogen light through spherical and ground glass lenses. A schematic showing the setup for the shadowgraph experiments is shown in Figure 4.1. The test section was an acrylic square duct with a hydraulic diameter, D_h , of 15 mm. An orthogonally-oriented X-Stream XS-5 digital camera was used to capture the side plane of the test section where the ferrofluid aggregate was located. The magnification of the camera was 63 microns per pixel with an image size of 500 (height) by 1020 (width) pixels, corresponding to the channel hydraulic diameter height of $D_h = 15$ mm and $4 D_h$ in the streamwise direction. Digital images were sampled at 50 Hz and a total of 3000 images were acquired for each data set, corresponding to a real time sampling of 60 seconds.

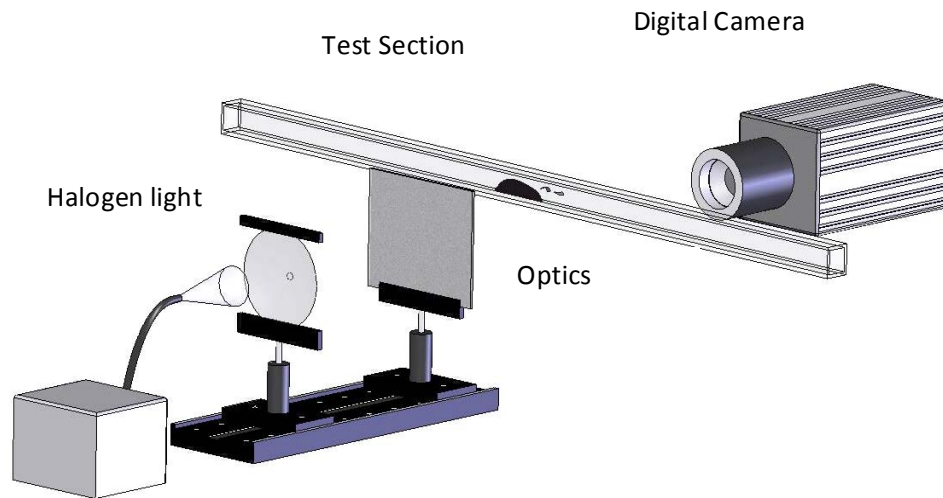


Figure 4.1. Schematic of focused shadowgraph experiment. A diffuse light source created a background from which to image the ferfluid aggregate.

In each case, a 2 ml volume of ferrofluid (EMG 705, Ferrotec, Inc.) was injected 4 diameters upstream of the region of interrogation before the start of each test in quiescent conditions at a rate of 1 ml per minute. A KD Scientific 230 syringe pump was utilized to introduce the ferrofluid supply streakline into the test section, and is accurate to 1% of full scale volumetric flow. The ferrofluid utilized in this experiment was diluted to 2% of its original concentration by mixing with water. The ferrofluid was captured and retained by a 0.5 Tesla permanent magnet that was obliquely oriented with one of its vertices located closest to the test section. This orientation results in a nearly two-dimensional magnetic field profile originating from the magnet, and has gradients predominantly orthogonal with respect to the planar wall of the test section. The magnet tip was located at a vertical distance of 3.5 and 4.5 mm from the test section wall, corresponding to 0.3 and 0.15 Tesla magnetic field strengths, B_{max} , at the inner test section wall, which is the maximum magnetic field induction experienced by the aggregate. The test section used in this experiment was 1 meter long to provide a fully-developed flow for all Reynolds numbers examined in this work. Reynolds numbers were varied from 200 up to 1000 for both B_{max} , and water was used for the bulk flow for all cases.

The bulk flow was switched on after all 2 ml of ferrofluid was accumulated and settled, and measured using a Transonic Systems ultrasonic flow meter with an absolute measurement uncertainty of 10% to verify the correct bulk flow conditions for each case. To ensure

quasisteady flow conditions, the flow time scale was compared the flow time scale, based on the specified Reynolds number for each test case. The flow time scale is calculated as the ratio of the viscosity, ν , to the squared average freestream velocity, U_o . Using standard properties of water, the time scales for the Reynolds numbers tested herein ranged between 0.005 to $2 \cdot 10^{-4}$ seconds. Flow was ramped up over 0.01 seconds to assure quasisteady flow.

4.4 PROPER ORTHOGONAL DECOMPOSITION OF DETECTED EDGES

A sample image showing the process by which the acquired grayscale frames are transformed into the detected interface between the ferrofluid aggregate and water is shown in

Figure 4.2. The interface was sampled for each snapshot of the flow using software written in-house in conjunction with the MATLAB image processing toolbox. The grayscale images were converted to black and white using Otsu's grayscale thresholding method [9], which assumes that the image is uniformly illuminated and a bimodal image histogram. Once the image is binarized, the regions of connected pixels in the images were identified and sorted by size for each frame. The size of the aggregate was obtained using this method by selecting the largest connected region, which was confirmed through an output of the binary image showing only the outline of the aggregate.

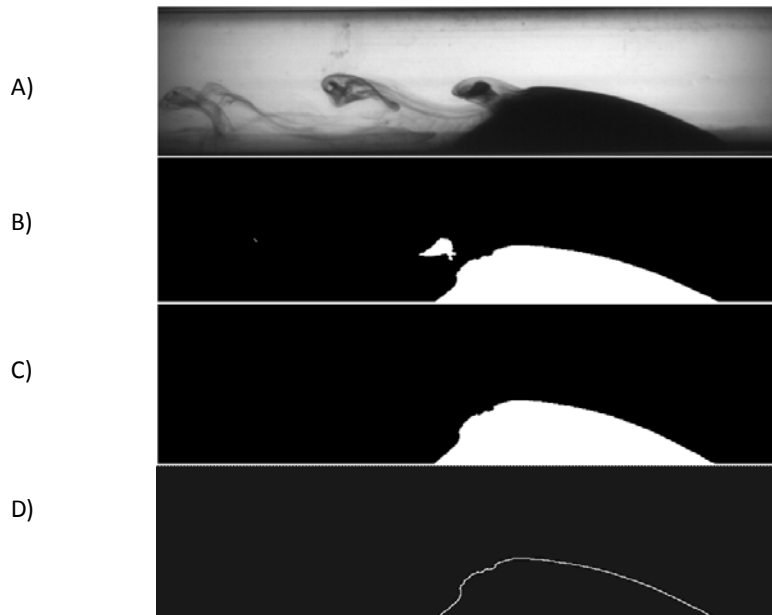


Figure 4.2. The image processing used to transform a grayscale image to a region corresponding to the instantaneous aggregate size (C) and the detected edge of the aggregate (D).

The aggregate sizes found with the binary images were weighted with the intensity in the aggregate region of the grayscale images which accounts for the local ferrofluid concentration and corrects the aggregate ratio by up to 10%. Moreover, the variance of all aggregates before flow startup is found to be within five percent of an overall mean aggregate size. The random error between two frames at quiescent flow was calculated to be +/- 0.5% in terms of the discrepancies in the calculated aggregate size.

The binary images were used to obtain a line representing the detected interface between the aggregate and bulk flow. Each edge obtained from the binarized aggregate is zero-padded to obtain a set of arrays of the same length for the length of the test case. The matrix of the space-time interface is then used to describe its nature using the Proper Orthogonal Decomposition. Proper Orthogonal Decomposition (POD) is a means to decompose the detected interface into its fundamental components using orthogonal basis functions. The advantage of POD is that the basis functions are not known *a priori* as with other decompositions, and the basis functions are selected mathematically to be the most energetically-efficient for each case.

The detected edges from the shadowgraphs, $y(x,t)$, are made up of POD modes with corresponding temporal coefficients of the form

$$y(x,t) = \sum_{i=1}^N \alpha_i(t) \phi_i(x) \tag{4.1}$$

where α_i are the projection coefficients which describe the time development of the mode shapes, ϕ_i , that describe the interface and its perturbations. POD has been used to study turbulence [10], image analysis [11], and many other topics. A comprehensive review of the POD technique and applications is given by Berkooz et al [12]. The results obtained using POD are useful to quantify the energetics of the aggregate interface as well as the interactions between the different modes over time. Calculating the number of modes required to reconstruct the interface defined by a certain energy threshold indicates its degree of stability and organization, and is known as the dimension. This reconstruction is determined by

comparing the summation of a specific number of modes, m , to the cumulative sum of all modes, N , written as

$$E_m = \frac{\sum_1^m \lambda_n}{\sum_1^N \lambda_n} \quad 4.2$$

where λ_n is the expected absolute value of the squared reconstruction calculated using Equation 4.1.

4.5 EFFECT OF THE MAGNETIC FIELD STRENGTH ON AGGREGATE STABILITY

As a first step to study the behavior of the aggregate under different flow conditions, the magnetic field was characterized. Since the strength of a dipole falls off rapidly, the local strength of the field is an important parameter in driving the aggregate behavior. The magnetic field was separately characterized using a traverse-mounted Gaussmeter. The primary component of the magnetic field, which is in the z-direction due to the magnet orientation, is perpendicular to the direction of bulk flow and is shown in a contour plot in Figure 4.3. An increased magnetic field strength of 0.3 Tesla compared to a baseline case of 0.15 Tesla was obtained by increasing the magnet's proximity to the test section wall using a precision traverse.

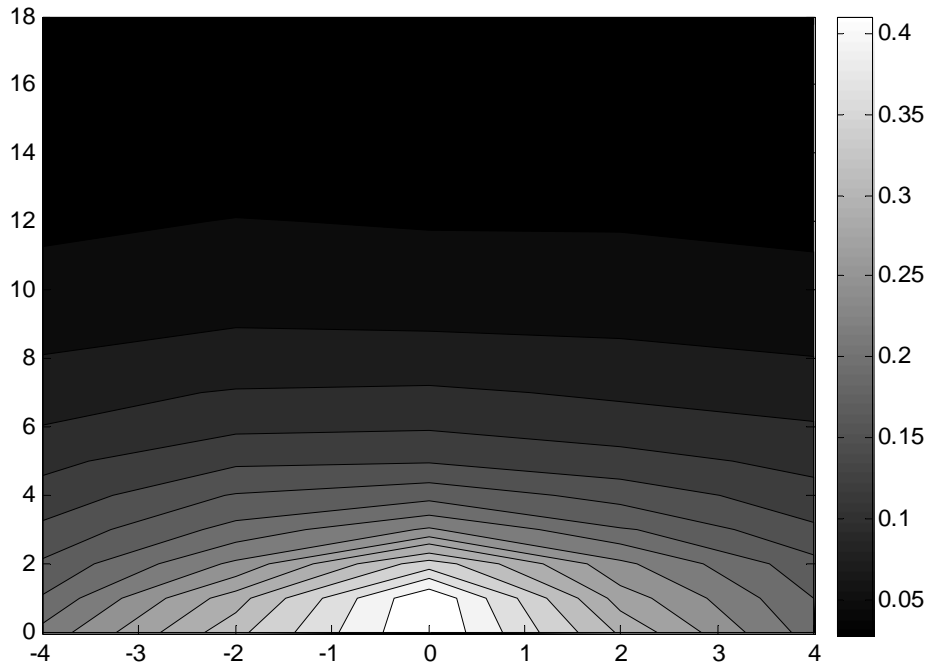


Figure 4.3. Contours of magnetic field induction in the z-direction in terms of Tesla. The highest field gradients are visualized near the magnet tip at $(x,y) = (0, 0)$.

A comparison of the change in apparent aggregate size for the two field strengths for Reynolds numbers spanning 200 to 400 in steady flow is shown in Figure 4.4. This plot shows the normalized aggregate size versus time, where the aggregate size in pixels is normalized with respect to the initial aggregate size. For Reynolds numbers of 200 and 300 for an applied field of 0.15 Tesla, no dispersion of the aggregate occurs. Both aggregates for these two Reynolds numbers experience slight stretching over time due to shearing, as evidenced by the slight increase in the normalized aggregate size as time increases. As the Reynolds number reaches 400 with maximum field strength, B_{max} , of 0.15 Tesla, the aggregate enters a transitional regime where initial stretching followed by slight aggregate erosion occurs. For higher Reynolds numbers of 500 and 600, the K-H instability results in exponential aggregate dispersion for a 0.15 Tesla applied field, shown in Figure 4.5.

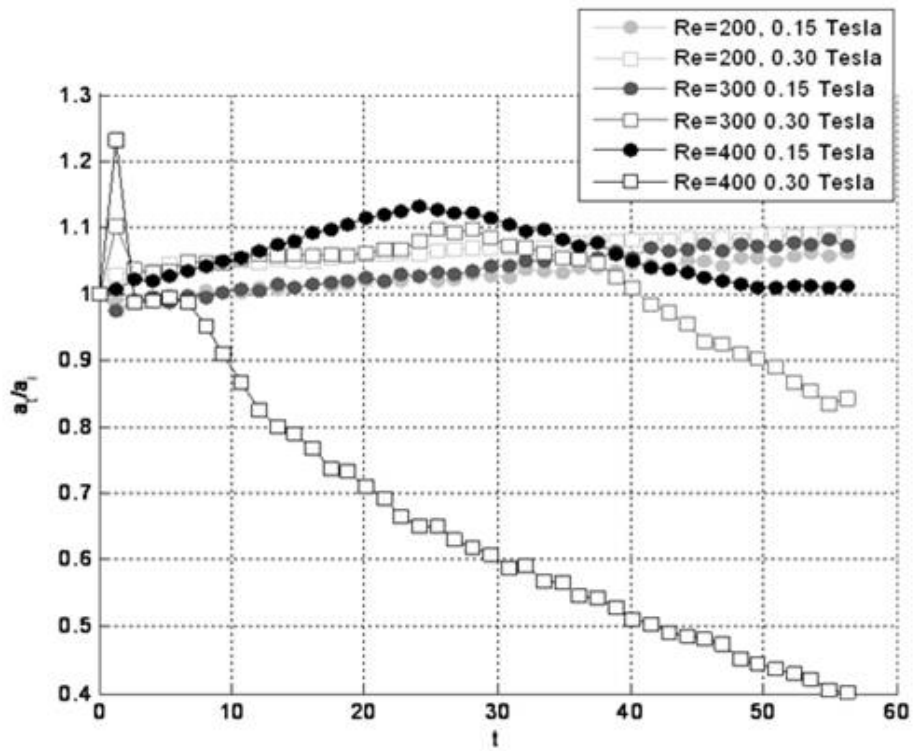


Figure 4.4. A comparison of the ferrofluid aggregate dispersion for three different Reynolds numbers. The transition to instability for a 0.3 Tesla magnetic field moves to 300 compared to 400 for a weaker magnetic field.

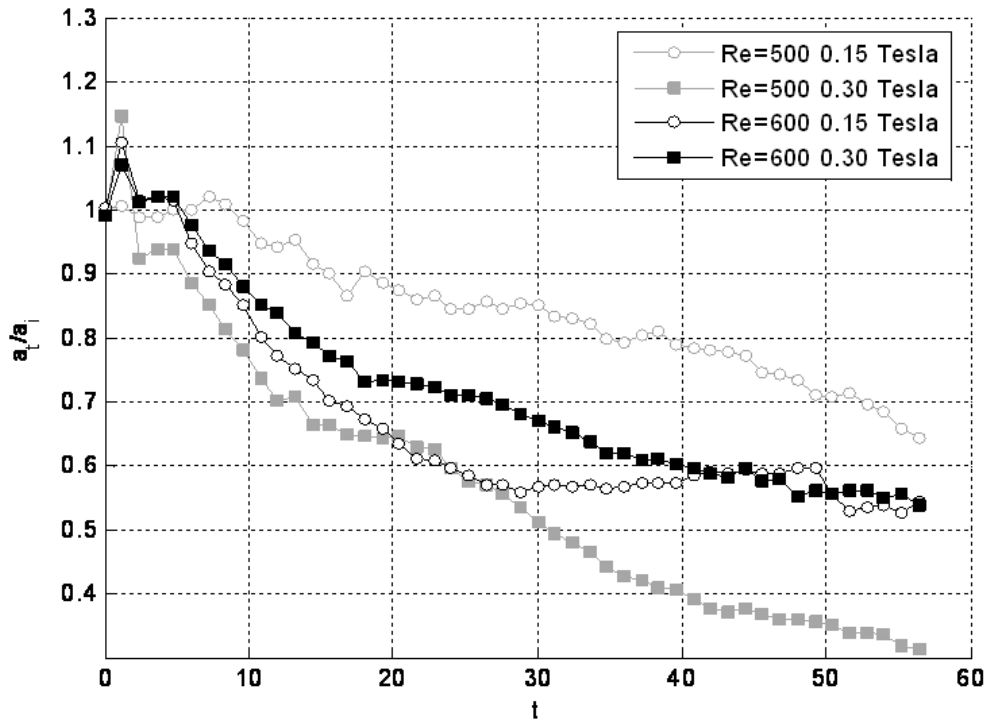


Figure 4.5. Aggregate size plots for Reynolds numbers of 500 and 600 for two different field strengths.

When the applied magnetic field is increased to 0.30 Tesla, no obvious effect occurs at the lowest Reynolds number of 200 when compared to lower field strength. However, at Re_{av} of 300, the transition between a stable and unstable aggregate occurs, where initial stretching of the aggregate of 10% gives way to tendrils of ferrofluid being convected from the aggregate, ultimately evolving into the K-H instability. Shadowgraphs of Re_{av} of 300 for the two field strengths are shown in Figure 4.6 at a time of 25 seconds. B_{max} of 0.15 Tesla remains stable while B_{max} of 0.30 is unstable, and K-H rolls are observed downstream of the aggregate. As the Reynolds number increases past 400, the fully unstable aggregate remains affected by the increased magnetic field strength. However, the effect of the increased field is diminished, as the increased inertia of the bulk flow is now dominates the aggregate. Therefore, K-H shedding and exponential aggregate erosion occurs for both field strengths at Reynolds numbers of 500 and 600.

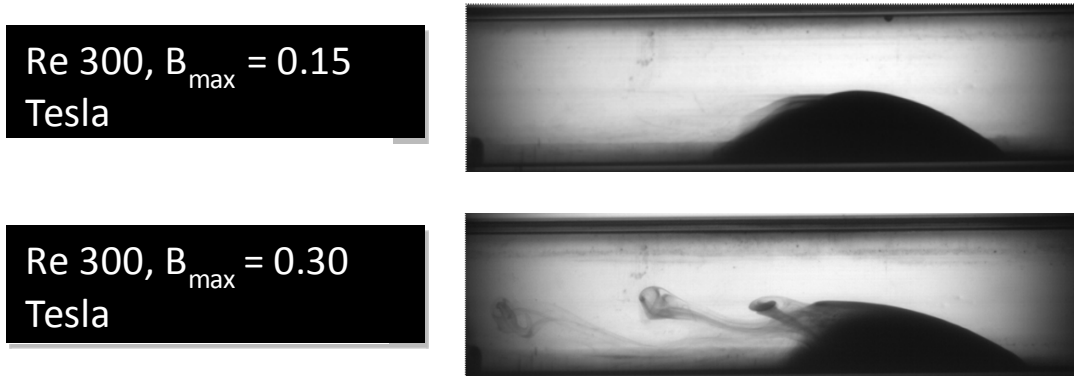


Figure 4.6. The impact of magnetic field strength for two different magnetic fields of 0.15 and 0.3 Tesla. For the stronger magnetic field, the aggregate destabilizes and K-H shedding occurs from the aggregate at a time of 25 seconds after the start of flow. K-H shedding causes a reduction in aggregate size.

Although the destabilization of ferrofluid aggregates occurs at different Reynolds numbers based on B_{\max} , aggregates follow the same path to destabilization. Four snapshots illustrating aggregate behavior at the Reynolds number at which the Kelvin-Helmholtz instability is first visualized are shown for each magnetic field strength in Figure 4.7. The set of images Figure 4.7A shows how the destabilization of the aggregate occurs for B_{\max} of 0.15 Tesla with a bulk flow rate of 500, while Figure 4.7B shows the destabilization sequence for B_{\max} of 0.30 Tesla for a Reynolds number of 400. Both sequences show how waves that are initially present on the aggregate interface are amplified. The amplification of these waves generates periodic pressure waves that act on the interface from the wake of the aggregate, which drive the transition to Kelvin-Helmholtz shedding from the aggregate. As shedding proceeds, the size of the vortices increases as the periodic pressure waves increase in strength. As the aggregate begins to diminish in size, the vortex rolls decrease in size, and attenuation of the K-H shedding occurs.

Similar features of the two B_{\max} continue as the Reynolds number is increased beyond 600, and continued convergence of the aggregate sizing is observed. The normalized aggregate size in time is plotted for Reynolds numbers of 900 and 1000 in Figure 4.8. Rapid decay of the aggregate occurs for both cases, and the overall dispersion curve is similar for both Re_{av} . These results indicate that the inertial forces continue dominance over magnetic forces for these cases, and the decreased difference in dispersion for these two Reynolds numbers illustrate that inertial forces are even more dominant than at lower Reynolds numbers. One feature of the higher magnetic field strength cases not captured by the aggregate sizing shown in Figure 4.8 is

a more compact hemi-spherical shaped ferrofluid aggregate that remains at the end of the data acquisition. In contrast, the 0.15 Tesla case results in a less compact stretched region. The behavior of these small-sized aggregates is consistent with greater magnetic field strength, as the aggregate is closer to a pole of the magnet.

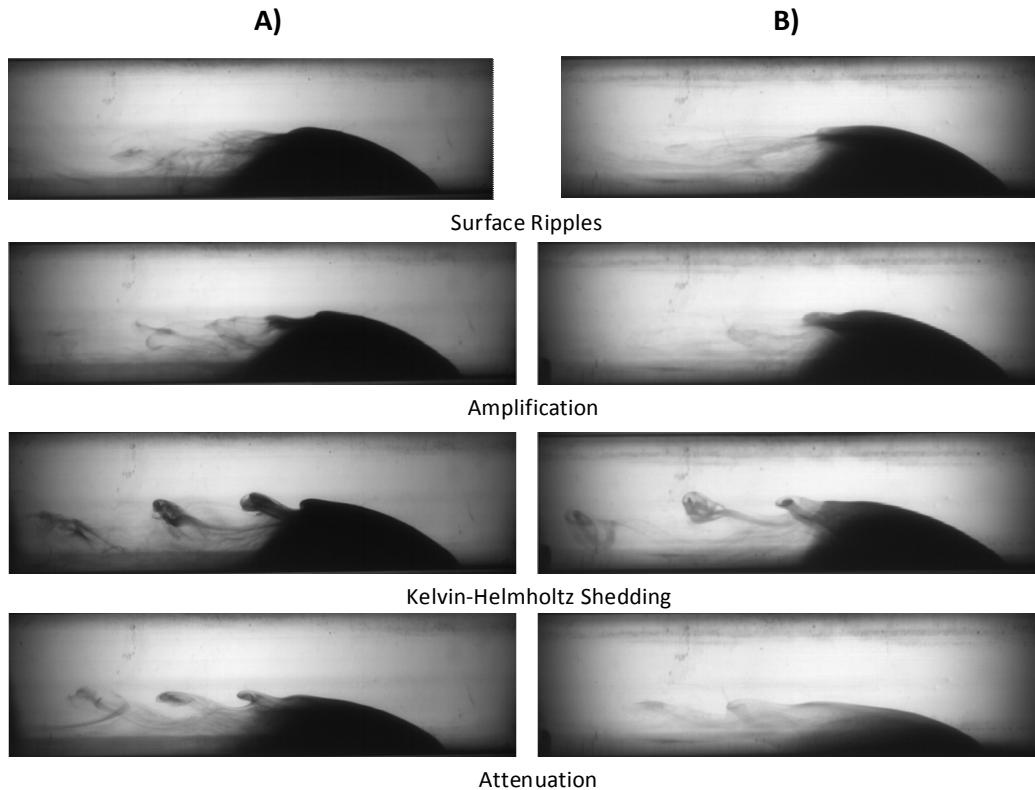


Figure 4.7. Four snapshots illustrating the transition to vortex shedding from the aggregate interface for A) a maximum field strength of 0.15 Tesla with bulk flow $Re_{av} = 500$ and B) a maximum field strength of 0.3 Tesla with a bulk flow $Re_{av} = 400$.

The POD dimension for the increased magnetic field strength at seven different Reynolds numbers is shown in Figure 4.9. These dimensions are calculated with the first eigenmode neglected, where the first mode represents the outline of the aggregate. The associated projection coefficients for the first mode indicate how the aggregate outline changes in time, or in essence how the aggregate changes in size over time. For higher-order modes, perturbations are superimposed on the aggregate outline, indicating interface disturbance in the form of K-H shedding.

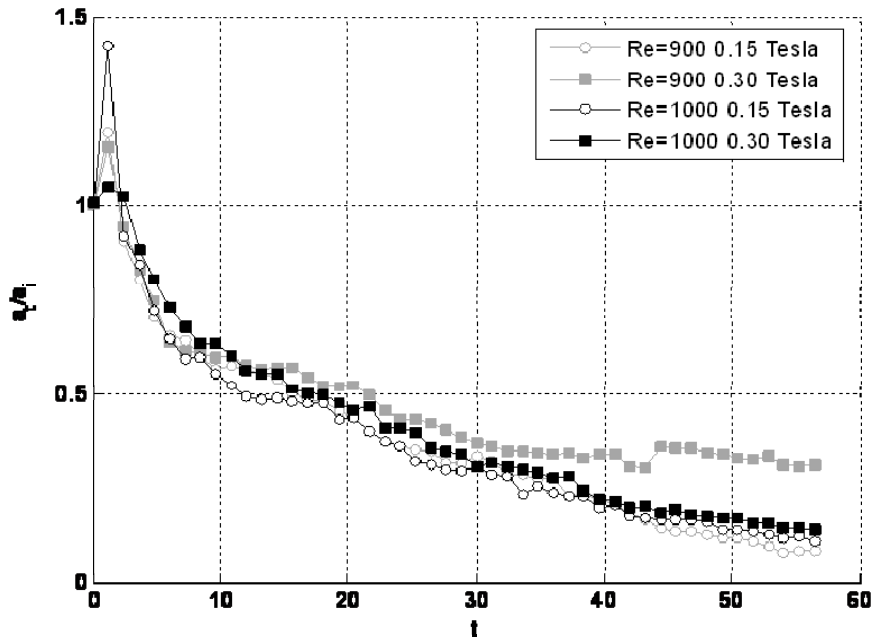


Figure 4.8. Aggregate sizing for Reynolds numbers of 900 and 1000. Convergence of size curves indicates inertia-dominated physics for these cases.

The results in Figure 4.9 show how many modes are required to reconstruct 99.5% of the remaining energy, neglecting the first mode. The higher field strength of 0.3 Tesla requires fewer modes to reconstruct 99.5% of the energy for Reynolds numbers between 200 and 300 indicating that energy is spread into higher modes for these cases. Energy transfer to higher order modes is consistent with incipient destabilization of the ferrofluid aggregate, which was observed at Re_{av} of 300 for higher field strength. Increasing the Reynolds number results in an unstable aggregate for both magnetic field strengths, and the number of modes required to capture the interface energy begins to converge as the Reynolds number is increased further. Convergence of dimension indicates the increasing dominance of inertial forces over magnetic forces as Reynolds number is increased, but the field strengths are held constant.

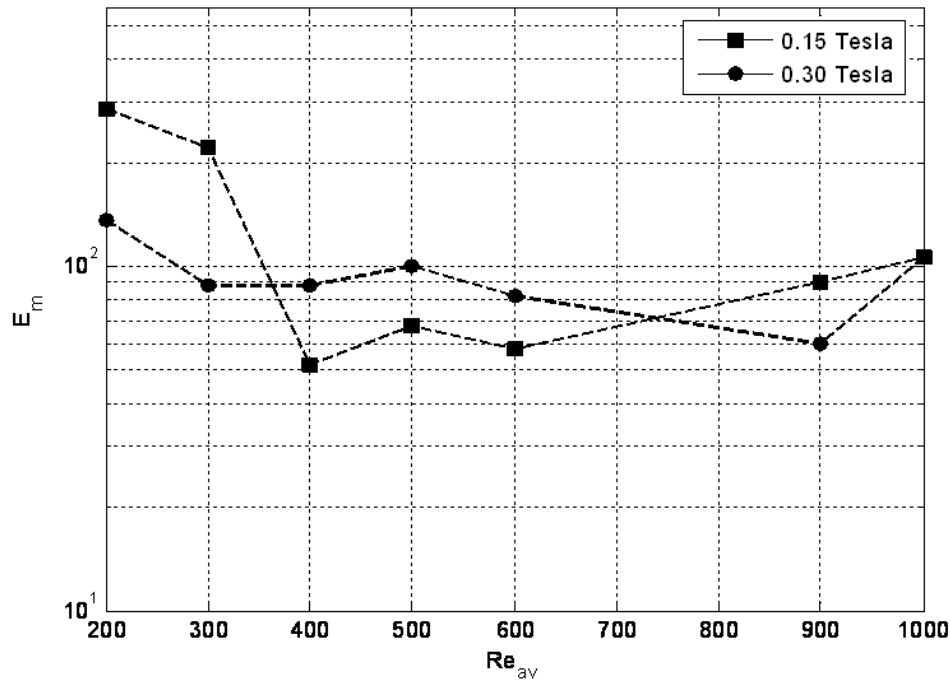


Figure 4.9. POD dimension for five different Reynolds numbers under the application of a 0.3 Tesla magnetic field compared to a 0.15 Tesla magnetic field. Convergence of the dimension occurs commensurate with behavior of aggregate sizing.

4.6 DISCUSSION

The Kelvin-Helmholtz instability is generated from a shear flow between the water and ferrofluid, where small-amplitude surface waves grow and evolve into vortices as the shearing is increased for constant magnetic field. As a dilution of the ferrofluid in water was utilized in this work, the density gradient between the two fluids is small, and the surface tension is negligible. Therefore, the primary mechanistic interaction is between the shear velocity of the two fluids as well as the magnetic forces. Since, in this experiment, we work with orthogonally-oriented magnetic fields, the surface wave direction is also oriented normal to the primary field components. Therefore, when the magnetic field strength and gradients are increased, the magnetic field acts as the mechanism to intensify the surface wave amplitude, and therefore, the aggregate can destabilize at lower Reynolds number.

The Kelvin-Helmholtz rolls act to wash away the ferrofluid aggregate rapidly, where its initial size is near $1/2D_h$. As the aggregate decreases in size, it is sheared by a lower velocity, and therefore, the surface wave amplitude decreases to the point that the magnetic field gradients act only to retain the aggregate on the test section wall near the magnet. As increasing the Reynolds number to 900 or 1000 while examining the different magnetic field strengths has little effect on the rate of aggregate decay, the relative strengths of both shear stresses and magnetic body forces is the driving factor in the behavior of the aggregate. Similarly, at low Reynolds number, changes in the magnetic field strength may singularly destabilize an aggregate that would otherwise remain stable at lower magnetic field strengths. The observations made in this experiment about the effect of increasing the normally-oriented magnetic field component is consistent with analytical stability studies of ferrofluid behavior that have been conducted by other groups, as discussed in a preceding section.

4.7 CONCLUSIONS

In this work, the dynamics of the ferrofluid aggregate retained by a permanent magnet and sheared by a non-magnetic bulk flow were investigated in terms of how aggregate behavior was affected by different magnetic field gradients. This work illustrates experimentally, for the first time, that increasing orthogonally-oriented magnetic field strengths acts to destabilize an aggregate of ferrofluid and generate K-H rolls. A 0.5 Tesla permanent magnet retained the ferrofluid in a small aggregate, and was oriented such that its primary field component was orthogonal to the streamwise direction. Focused shadowgraphs were utilized as a means to visualize and measure aggregate development in time. The Proper Orthogonal Decomposition was applied to the detected interface of the ferrofluid aggregate with the bulk flow to include the interface behavior under different flow conditions.

Herein, we experimentally observed how increasing the intensity of the magnetic field strength results in destabilization of the ferrofluid aggregate and the development of the Kelvin-Helmholtz instability due to interfacial shearing. Examination of the energy captured by the POD modes indicates that the increased magnetic field strength is responsible for the transfer of energy into higher order modes at low Reynolds numbers, indicating higher disorganization

which is consistent with the transition to the K-H instability at these lower Re_{av} . For Reynolds numbers of 500 to 600, the dispersion and dimension of each field strength case begins to converge, indicating that inertia begins to dominate over magnetic forces. As the Reynolds number increases to 900 and 1000, the difference in dispersion over time is minimal, and similar amounts of the aggregate are decayed, indicating that inertial shearing is fully dominant over the magnetic forces.

4.8 REFERENCES

1. Crowley, M.D. and R.E. Rosensweig, *The interfacial stability of a ferromagnetic fluid*. *Journal of Fluid Mechanics*, 1967. 30(4): p. 671-688.
2. Boudouvis, A.G., et al., *Normal field instability and patterns in pools of ferrofluid*. *Journal of Magnetism and Magnetic Materials*, 1987. 65(2-3): p. 307-310.
3. Rosensweig, R.E., M. Zahn, and R. Shumovich, *Labyrinthine instability in magnetic and dielectric fluids*. *Journal of Magnetism and Magnetic Materials*, 1983. 39(1-2): p. 127-132.
4. Zahn, M. and R. Rosensweig, *Stability of magnetic fluid penetration through a porous medium with uniform magnetic field oblique to the interface*. *Magnetics, IEEE Transactions on*, 1980. 16(2): p. 275-282.
5. Malik, S.K. and M. Singh, *Finite amplitude Kelvin--Helmholtz instability in magnetic fluids*. *Physics of Fluids*, 1986. 29(9): p. 2853-2859.
6. Miranda, J.A. and M. Widom, *Parallel flow in Hele-Shaw cells with ferrofluids*. *Physical Review E*, 2000.61(2): p. 2114.
7. Williams, A.M., Puri, I.K., and Vlachos, P., July 2006, *Magnetic Targeting of Particle Transport Under Pulsatile Flow*, 2006 ASME Fluids Engineering Division Summer Meeting, Miami, FL.
8. Williams, A.M. and P. P. Vlachos, August 2008, *The Dynamics of Accumulating Ferrofluid Aggregates*. 2008 ASME Fluids Engineering Division Summer Meeting, Jacksonville, FL.
9. Otsu, N., *A Threshold Selection Method from Gray-Level Histograms*, *IEEE Transactions on Systems, Man, and Cybernetics*, Vol. 9, No. 1, 1979, pp. 62-66.
10. Sirovich, L., K.S. Ball, and L.R. Keefe, *Plane waves and structures in turbulent channel flow*. *Physics of Fluids A: Fluid Dynamics*, 1990. 2(12): p. 2217-2226.

11. Kirby, M. and L. Sirovich, *Application of the Karhunen-Loeve procedure for the characterization of human faces*. Transactions on Pattern Analysis and Machine Intelligence, 1990. 12(1): p. 103-108.

12. Berkooz, G., P. Holmes, and J.L. Lumley, *The Proper Orthogonal Decomposition in the Analysis of Turbulent Flows*. Annual Review of Fluid Mechanics, 1993. 25(1): p. 539-575.

5.1 ABSTRACT

The physics of steady and pulsatile flows laden with superparamagnetic nanoparticles in a square channel accumulating under the influence of a 0.5 Tesla permanent magnet are studied by means of focused shadowgraphs. The accumulation physics of these nanoscale particles are explored as functions of the flow type (steady and unsteady) and accumulation type (injected from the top of channel versus bottom of channel). Ferrofluid is accumulated by the steady injection of a streakline that enters the test section upstream of the magnet, where an aggregate forms. The interfacial phenomena resulting from the interaction of the ferrofluid with the bulk flow is digitally-resolved using focused shadowgraphs.

Ferrofluid aggregate physics is examined both visually in the raw frames as well as by post-processing to determine the aggregate size evolution in time and couple that bulk information with interfacial behavior using the Proper Orthogonal Decomposition (POD). The shadowgraphs show that the aggregate exhibits different regimes based on bulk flow Reynolds number, which is varied between 100 and 1000, based on the mean flow rate. The aggregate exhibits stable behavior at low Reynolds numbers, where it stretches as it grows and minimal decay of the aggregate occurs. At moderate Reynolds numbers above 400, inertial forces dominate the dynamics, and aggregates do not attain the same size and height as in low Reynolds number cases. Therefore, the interaction of the aggregate with the bulk flow is diminished. The accumulation of ferrofluids is positively impacted by increased magnetic field gradients for lower Reynolds numbers, while very high or low magnetic field gradients result in smaller, unstable aggregates. This work is the first to study the accumulation of ferrofluid aggregates over such a large parameter space, which reveals many physics that were previously unexplored in ferrohydrodynamics.

5.2 INTRODUCTION

Ferrofluids are liquids in which subdomain particles made up of magnetite at nanoscale sizes and are stably-suspended. Their uniqueness stems from the high susceptibility of the nanoscale particles [1] and have been studied academically for over 40 years. Due to their magnetization potential, many classical fluid dynamics phenomena such as the Rayleigh-Taylor and Kelvin-Helmholtz instabilities may be either amplified or controlled when ferrofluids are utilized [2,3]. However, the papers studying such physics are most often analytical in nature.

Herein, we extend our understanding of accumulating ferrofluid aggregates by examining their interaction with steady and pulsatile non-magnetic flows of Reynolds numbers ranging between 100 and 1000 using focused shadowgraphs. Previous studies on this topic have characterized the behavior of such aggregates at Reynolds numbers below 400, where periodic washaway of the aggregate was described by Ganguly, Gaiind, and Puri [4,5]. A key finding of these works is that several characteristics of aggregate accumulation are described by power law behavior based on the bulk flow Reynolds number. Extension of this work has been performed by the authors, where thus far, the two-fluid interaction produces the Kelvin-Helmholtz instability for flow conditions at moderate Reynolds number of 400 and higher [6]. The vortex shedding of ferrofluid associated with the Kelvin-Helmholtz instability is responsible for exponential decay of the dispersing ferrofluid aggregate. This paper seeks to determine how aggregates that are accumulating with incident bulk flows behave as well as the driving parameters that dictate the development of ferrofluid aggregates as they accumulate and their rate of dispersion as accumulation ceases.

The focused shadowgraphs obtained for all cases were analyzed in terms of the apparent aggregate size in time. Moreover, the interface between the aggregate and bulk water flow was described by means of the Proper Orthogonal Decomposition, which is used to decompose the detected interface into its fundamental modes. This method is useful for examining interactions between different modes, can also be used to illustrate how aggregate interaction with the bulk flow changes as the aggregates size varies. Herein, the means by which the raw shadowgraph frames were obtained will be discussed first, followed by the methodology to perform post-processing of these frames in order to determine the aggregate size and detect its interface with the bulk flow. The accumulation of ferrofluid aggregates will

be discussed in terms of the behavior of bottom-injected ferrofluid for steady and unsteady flows, followed by the results for top injected ferrofluids. Finally, the effect of five different magnetic field strengths will be discussed with respect to their impact on development and retention of ferrofluid aggregates.

5.3 FOCUSED SHADOWGRAPH METHODS

The data was obtained in this experiment by means of focused shadowgraphs; a qualitative method to visualize a flow and is particularly effective when viewing phenomena with a high contrast interface, as is the case with water flowing past a ferrofluid aggregate contained in a 15 mm square test section. The ferrofluid aggregate was visualized by directing a 250 Watt halogen light through spherical and ground glass lenses to illuminate a region of uniform intensity. A schematic showing the setup for the shadowgraph experiments is shown in Figure 5.1.

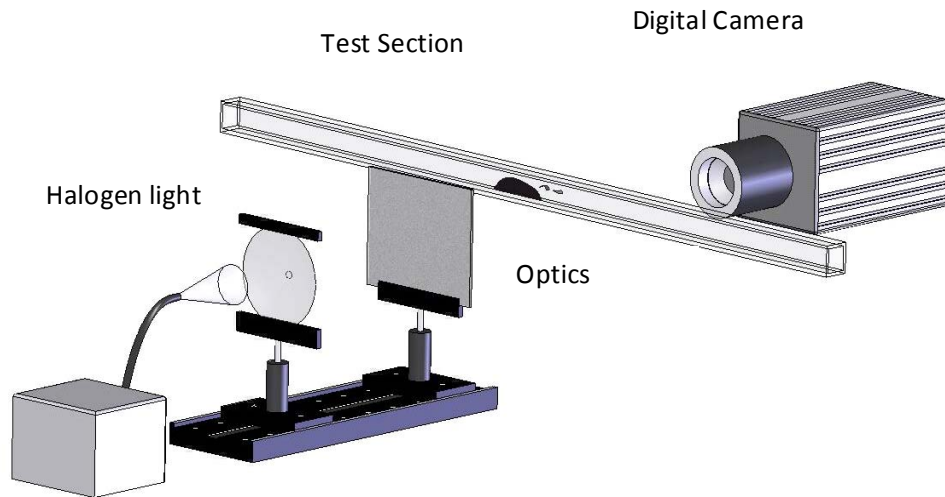


Figure 5.1. Schematic of focused shadowgraph experiment. A digital camera imaged the ferrofluid aggregate accumulation and subsequent dispersion.

An orthogonally-oriented digital camera was used to image the side plane of the test section where the ferrofluid aggregate was retained by the magnet. The image magnification was 57 microns per pixel with an image size of 1280 by 300 pixels, which encompasses the height and equivalent hydraulic diameter of the channel of 15 mm and a length of $4 D_h$. The test section itself was 1 meter long to provide a fully-developed flow for all Reynolds numbers examined in this work. Digital images were sampled at 30 Hz to resolve the ferrofluid buildup and shedding at the location of the magnet. The total number of images obtained for each data set was 10300 images, corresponding to a real time sampling of nearly six minutes.

In each case, a 2 ml volume of ferrofluid (EMG 705, Ferrotec, Inc.) was injected 4 diameters upstream of the region of interest at the beginning of each case and introduced into the specified bulk flow. A KD Scientific 230 syringe pump was utilized for all injection, and is accurate to within 1% of the flow rates examined in this work. The ferrofluid injection rate was selected based on the Reynolds number, considering the position of the incoming ferrofluid stream with respect to the expected Poiseuille velocity profile. The needle was at a location where the bulk flow velocity corresponds to approximately 25% of the average. Therefore, the injection flow rate was selected to match the Reynolds number at that flow speed. Faster or slower injection rates result in either a turbulent jet or a process too slow to be sufficiently captured due to limited camera buffer. A summary of the injection rates for each of the Reynolds numbers examined in this experiment is shown in Table 5.1.

Table 5.1. Injection flow rates based on bulk flow inertia for all Reynolds numbers examined in experiment.

Reynolds Number	Injection Rate ml/m
100	0.344
200	0.688
300	1.03
400	1.38
500	1.72
600	2.10
700	2.44
800	2.75
900	3.10
1000	3.44

The ferrofluid, which is miscible with water, was captured and retained by a 0.5 Tesla permanent magnet that was obliquely oriented with one of its vertices closest to the test section such that the ferrofluid was subjected to field gradients that are nearly 2-dimensional. The magnet tip was located a vertical distance of 4 mm from the test section for the majority of test cases. A later section of this paper will explore the effect of different magnetic field gradients, which was achieved by varying the vertical separation of the magnet tip and test section wall.

A total of 80 different cases were examined in this experiment, where the effects of inertia, flow unsteadiness, top versus bottom of the channel injection of the ferrofluid streakline, and magnetic field gradients were tested. Each effect was examined for Reynolds numbers based on the average test section velocity that ranged between 100 and 1000 in increments of 100. A schematic describing the relative locations of the test section, magnet, and ferrofluid aggregate are shown in Figure 5.2. All unsteady flows examined in this experiment were sinusoidal pulsatile flows. The amplitude and offset of the sinusoid waveform was made such that the pulsatile flow had the same mean flow rate as the steady flows, and therefore, the same Reynolds number based on the mean flow. The sine wave pulsation frequency was selected to be 0.3 Hz to visualize the structure development of the shedding aggregate.

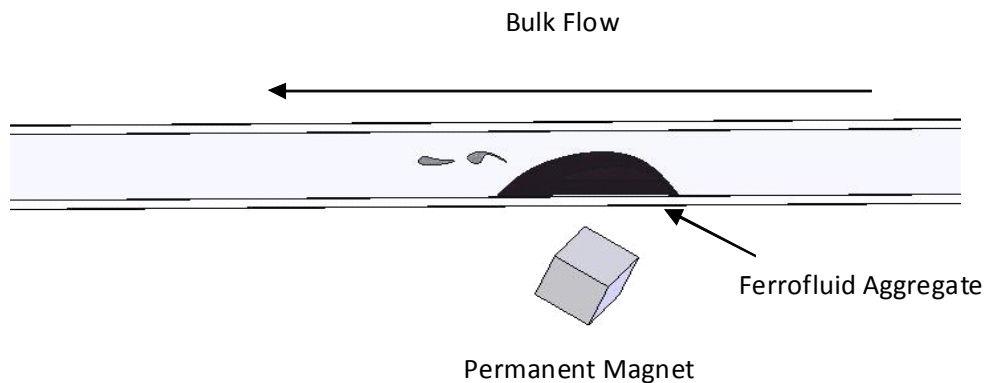


Figure 5.2. Schematic of ferrofluid aggregate and relative orientations of test section and permanent magnet.

5.4 PROPER ORTHOGONAL INTERFACE DECOMPOSITION

The raw images obtained from the shadowgraph acquisition were post-processed to calculate the apparent aggregate size and to sample the aggregate interface with the bulk flow in time. A sample image illustrating the conversion from the raw grayscale frame to the detected edge is shown in Figure 5.3. The aggregate size and interface was post-processed for each acquired snapshot using software written in-house in conjunction with the MATLAB image processing toolbox. The grayscale images were converted to binary frames using Otsu's thresholding method, which assumes uniform illumination and a bimodal image histogram, and separates foreground and background [7].

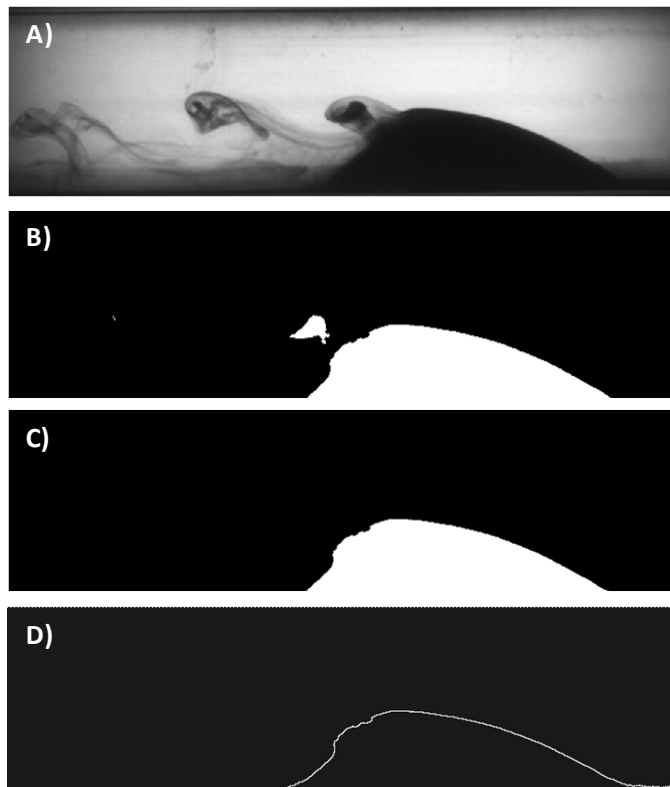


Figure 5.3. The image processing used to transform a grayscale image A) to a region corresponding to the instantaneous aggregate size (B and C) and the detected edge of the aggregate (D).

The result of this thresholding is used to binarize the grayscale images and the rough aggregate profile is obtained. Once the images are binarized, regions of connected pixels are

grouped and sorted by size for each frame, and the size of the aggregate was obtained by selecting the largest region. The aggregate size determined from the binary images was weighted with the grayscale intensities in the region of the aggregate, which accounts for the local ferrofluid concentration and corrects the aggregate ratio by up to 10%. The random error between two frames at quiescent flow was calculated to be +/- 0.5%.

Using the detected edges from each frame, Proper Orthogonal Decomposition (POD) was performed. POD provides a means to decompose the detected interface into its fundamental components using basis functions chosen for each set of data due to their energetic efficiency. The detected edges, $Y(x,t)$, are described by the combination of the POD modes with corresponding temporal coefficients, and takes the form of

$$y(x,t) = \sum_{i=1}^N \alpha_i(t) \phi_i(x) \tag{5.1}$$

where α_i are the projection coefficients which describe the temporal changes of the mode shapes, ϕ_i . POD has been used comprehensively in fluid mechanics with particular attention to studies of turbulence [8,9,10] and also flows in which instabilities are present [11]. The projection coefficients obtained using POD are useful to describe the interactions between the different modes, which can be illustrated using phase portraits that compare the temporal behavior relating two or more modes. Calculating the number of modes required to reconstruct the interface indicates its degree of stability and organization, and is known as the dimension, which is based on the energy threshold of 99.5% of the total value. This reconstruction is determined by comparing the summation of a specific number of modes, m , to the cumulative sum of all modes, N , written as

$$E_m = \frac{\sum_1^m \lambda_n}{\sum_1^N \lambda_n} \tag{5.2}$$

where λ_n is the expected absolute value of the squared reconstruction containing both the projection coefficient and mode for each mode number.

5.5 EFFECT OF BULK FLOW INERTIA AND UNSTEADINESS

The effect of the bulk flow inertia is to carry the ferrofluid aggregate past the target magnet site as increasing inertia generates higher shear compared with magnetic forces. Qualitatively, the aggregate accumulates stably for Reynolds numbers of 100-200 in steady flow, but aggregate decay and destabilization is observed at 300 and above. Figure 5.4 illustrates the build up and then decay of the ferrofluid aggregate once injection ceases for a ferrofluid streakline injected from the bottom of the test section. Flow is moving from right to left, with the injection stream shown by the thin line of dark fluid that enters the region of interrogation near the bottom of the aggregate.

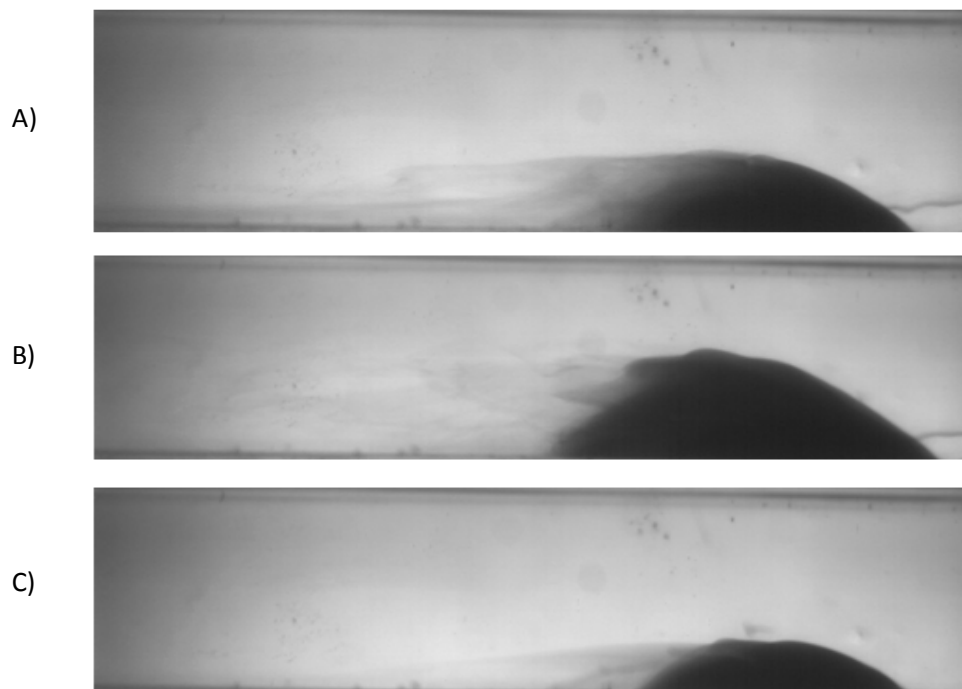


Figure 5.4. Ferrofluid accumulation and washaway for a Reynolds number of 300 at A) 50% of total injected volume B) 100% of total injected volume and C) at the end of the data set.

Erosion of the aggregate is manifested in tendrils of ferrofluid that are sheared from the aggregate at a Reynolds number of 300. At higher Reynolds numbers, the decay is driven by the

Kelvin-Helmholtz shedding from the aggregate which develops from ripples on the interface between the aggregate and bulk flow that amplify into ferrofluid rolls. In pulsatile flows, periodic stretching and coalescence of the ferrofluid aggregate is observed in conjunction with the temporal variation of the flow rate.

As the flow inertia increases, the maximum attained height of the aggregate (and the maximum aggregate size) decreases. A summary of the normalized aggregate sizes is shown in Figure 5.5 for steady flow. The normalization factor was selected based on the aggregate size in quiescent flow after 2 ml of ferrofluid was injected, which represents the maximum possible size of the aggregate. When the aggregate size in time is normalized to this maximum, a size ratio referenced to 1 is obtained, which indicates 100% attainment of the maximum possible aggregate size. The normalized aggregate sizes are plotted versus dimensionless time, where the normalization factor for each case is the period over which ferrofluid is injected. In Figure 5.5, the maximum aggregate size ratio decreases from near 1 for Reynolds numbers of 100 to 300 to zero for Reynolds numbers of 900 and 1000. The reduced ability of the magnet to capture the ferrofluid aggregate is consistent with shear stresses dominating the magnetic body forces. The normalized aggregate size plotted against normalized time for pulsatile flows are shown in Figure 5.6 across all Reynolds numbers. The higher peak bulk flow velocities encountered for pulsatile flow dictate the diminished capture ability of the magnet. This effect can be observed particularly for an average Reynolds number of 400, where in steady flow, a normalized time of 4 shows a leveling of the relative aggregate size to roughly 0.28 compared to its maximum size of 0.54. This result implies that enough of the aggregate has been dispersed such that it is interacting to a lesser degree with the bulk flow and therefore the change in aggregate size slows as the aggregate shrinks. In contrast, pulsatile flow results in a continuing decay of the aggregate past 4 injection time lengths until the aggregate is nearly washed away. For higher Reynolds numbers, pulsatility results in very limited accumulation of ferrofluid, and that accumulated aggregate has a short residence time. Therefore, for bottom-injected ferrofluid streaklines, pulsatility disrupts the ability of magnetic field gradients to retain the aggregate.

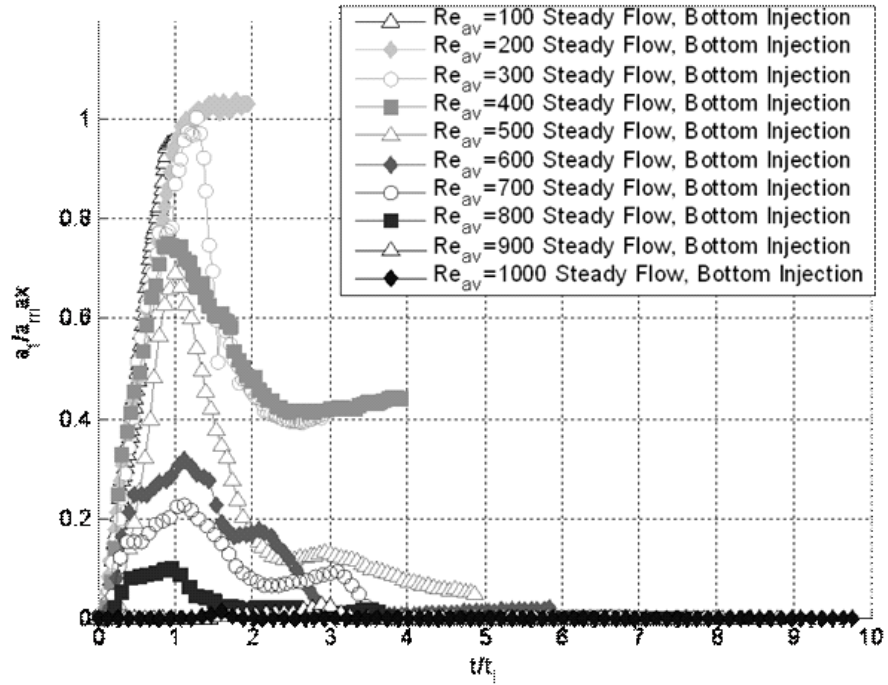


Figure 5.5. Plot of the intensity-weighted aggregate accumulation versus normalized time for accumulation in steady flow.

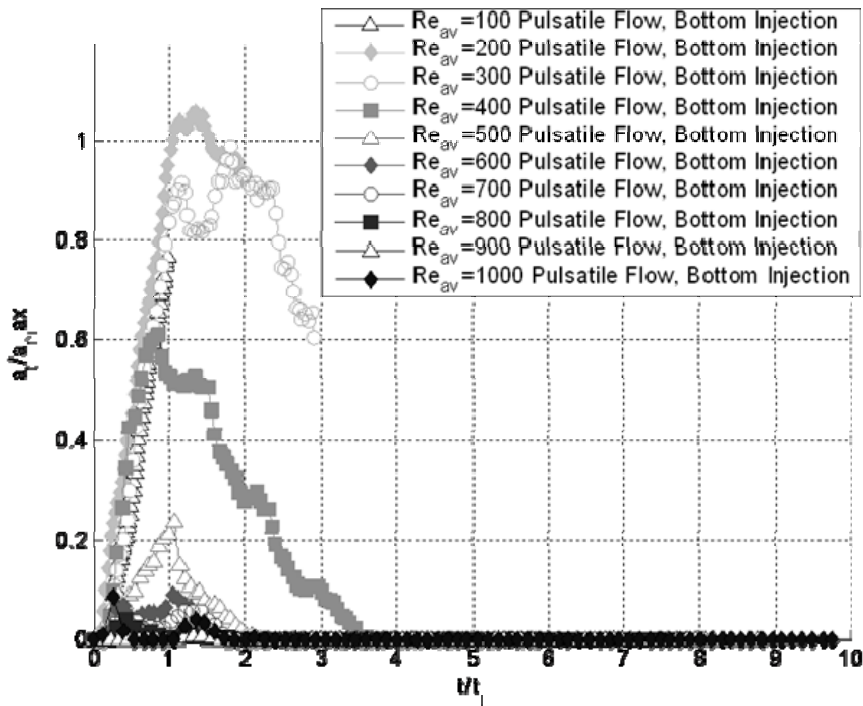


Figure 5.6. Normalized accumulation plotted versus normalized time with respect to total injection timespan for pulsatile flow.

Figure 5.7 shows the normalized maximum aggregate size for both steady and pulsatile flows. Here, the stretching of the ferrofluid aggregate is observed, indicated by aggregate size ratios exceeding 1. Aggregate stretching is consistent with results presented from Williams, et. al. [6], where stretching was observed as a precursor for aggregate dispersion for Reynolds numbers of 400 and 300 in steady and pulsatile flows, respectively. For higher Re , aggregate stretching can lead to the Kelvin-Helmholtz instability. For the accumulating ferrofluid aggregate, transition occurs as the Reynolds number is increased above 300, and the ferrofluid aggregate does not reach its maximum potential size. Figure 5.7 illustrates that the maximum aggregate size experiences an exponential decay as the Reynolds number is increased. Both steady and pulsatile flows exhibit similar capture ability of the ferrofluid aggregate for the same average Reynolds numbers, however, pulsatility results in lower aggregate capture over nearly all cases of bottom injected ferrofluid streaklines.

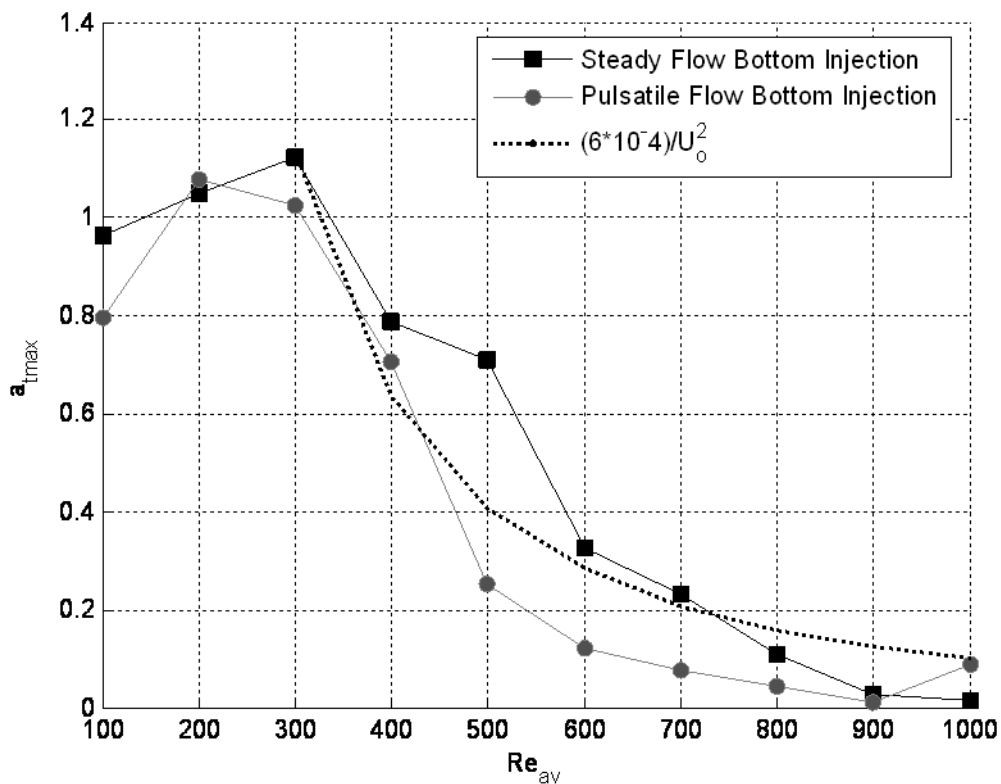


Figure 5.7. Plot of the maximum size attained by the aggregate taken from the temporal aggregate measurements, normalized by the maximum aggregate size.

The results of the POD processing for steady and pulsatile flows for bottom injection of ferrofluid are shown in Figure 5.8. For each Reynolds number, the dimension, or the total number of modes required to reconstruct 99.5% of the total energy in the interface is plotted. The results of the POD analysis indicate that pulsatile flows with bottom injected ferrofluid require more modes to reconstruct the energy, which indicates the higher complexity of the interface in pulsatile flow. An increase in the dimension for the pulsatile flow cases is consistent with the addition of the periodic stretching and contraction of the aggregate as it interacts with the bulk flow. Moreover, the number of modes required to reconstruct the interface increases with the Reynolds number, which is consistent with aggregate destabilization and Kelvin-Helmholtz shedding.

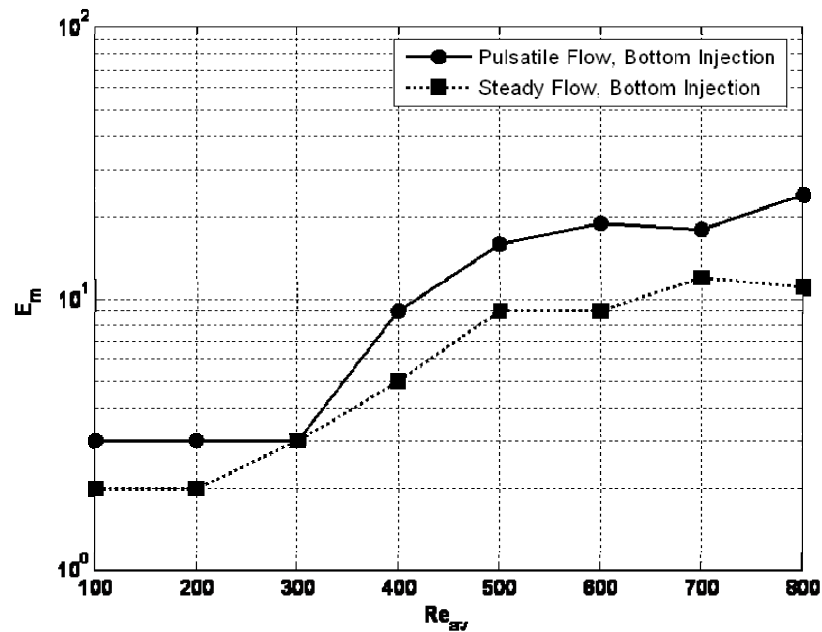


Figure 5.8. Plot of the number of modes required to reconstruct 99.5% of the energy of the interface for steady and pulsatile flows when the ferrofluid is injected from the bottom on the test section.

5.6 TOP INJECTION OF FERROFLUID STREAKLINE

As observed in the previous section, the ferrofluid accumulation was negatively impacted by increasing the flow inertia for both steady and pulsatile cases. Now, the effect of injecting the ferrofluid streakline on the opposite test section wall relative to the magnet is

examined. Injecting the ferrofluid streakline on the top test section wall results in modified ferrohydrodynamics, as now the ferrofluid is being accelerated through the bulk flow, orthogonal to the streamwise direction, by magnetic forces. This results in the formation of finger-like expansions from the ferrofluid streakline, and ultimately, vortex rings consistent with the Rayleigh-Taylor instability that expand as packets of ferrofluid approach the magnet. Figure 5.9 shows the behavior for top injected ferrofluid for three time snapshots of the ferrofluid aggregate in a Reynolds number of 300 at 50 and 100% of the total injection volume, and at the end of the data set. The bending of the ferrofluid streakline towards the magnet is observed, as well as the Rayleigh Taylor fingering that strengthens as the streakline nears the magnet. Since the ferrofluid streakline is injected from the top, one direct consequence is the development of a significantly smaller aggregate, and a large wake region is visible just downstream of the aggregate due to the overshooting of the ferrofluid streakline. Once injection is complete in Figure 5.9C, the aggregate becomes compact, with a minimal wake region. Visually, comparing the results in Figure 5.9 and Figure 5.4, a diminished aggregate capture occurs, since the ferrofluid streakline does not travel directly to the region of high-gradient magnetic fields.

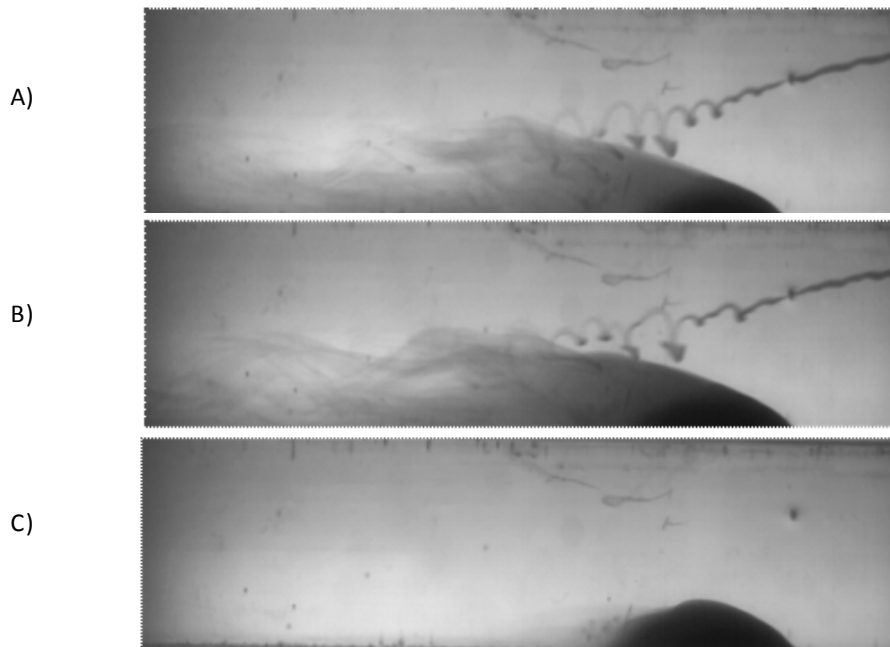


Figure 5.9. Ferrofluid accumulation and washaway for top injection at a Reynolds number of 300 at A) 50% of total injected volume B) 100% of total injected volume and C) at the end of the data set.

Comparing the normalized accumulation in steady flow for top injection to that from bottom injection in Figure 5.10, we first observe that at the low Reynolds numbers of 100 to 300, accumulation of the ferrofluid aggregate occurs. However, the net accumulated ferrofluid aggregate is much smaller than for the bottom injection cases. For the pulsatile flow results shown in Figure 5.11, flow pulsatility actually provides a benefit towards the accumulation of the aggregate for Reynolds numbers above 400, due to the periods of low bulk flow. Conversely, pulsatile flows with Reynolds numbers below 400 result in a reduced build up of the aggregate compared to steady flows. Therefore, flow pulsatility is a dual effect for top-injected ferrofluids, negatively impacting accumulation for low Reynolds numbers due to the periodic high flow rates, but assisting accumulation for Reynolds numbers above 400 due to periods of low flow.

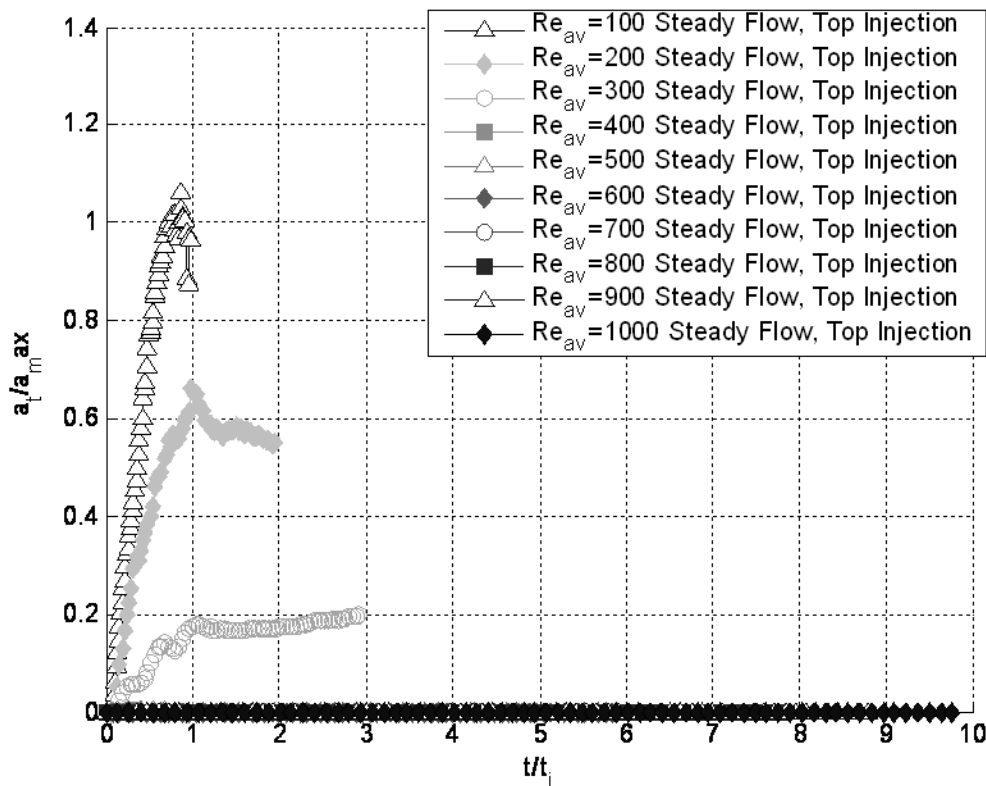


Figure 5.10. Steady flow, top injection of ferrofluid aggregate. Significant accumulation only occurs for low Reynolds numbers.

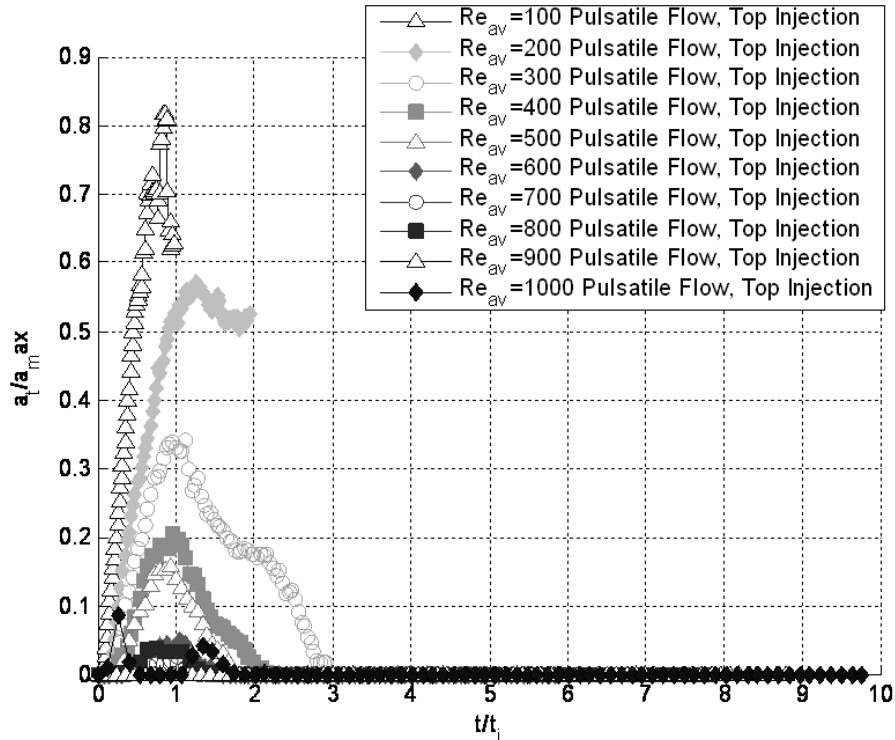


Figure 5.11. Pulsatile flow, top injection of the ferrofluid aggregate. Pulsatility assists accumulation for higher Reynolds numbers compared to the results for steady flow.

Summaries of the aggregate maximum aggregate size and number of modes needed to reconstruct the aggregate interface are shown in Figure 5.12 and Figure 5.13, respectively for the top-injected ferrofluid cases. Figure 5.12 confirms that pulsatility acts as both a suppressor and enhancement to aggregate accumulation based on the Reynolds number not only as the aggregate accumulates and disperses, but the dual effect of pulsatility extends to the maximum aggregate size attained. The enhancement in aggregate accumulation for pulsatile flows decreases as the Reynolds number increases, up to 1000 where essentially no accumulation occurs as evidenced by the aggregate attaining a zero size. Figure 5.13 illustrates that pulsatile flows require more modes for interface reconstruction than do steady flows, as observed previously for the bottom-injected cases. The reconstruction requirement for steady flows drops to one mode for Reynolds numbers above 300, as no accumulation occurs and the detected interface is a flat line for all snapshots. As Reynolds number increases, the dimension for pulsatile flows increases, then decreases. This is indicative of a complex interface at moderate Reynolds numbers, where the aggregate has attained a significant size and hence is interacting significantly with the bulk flow. The decrease in number of modes needed at high

Reynolds numbers results from a very slight aggregate merely being slowly sheared away from the magnet, with no Kelvin-Helmholtz shedding.

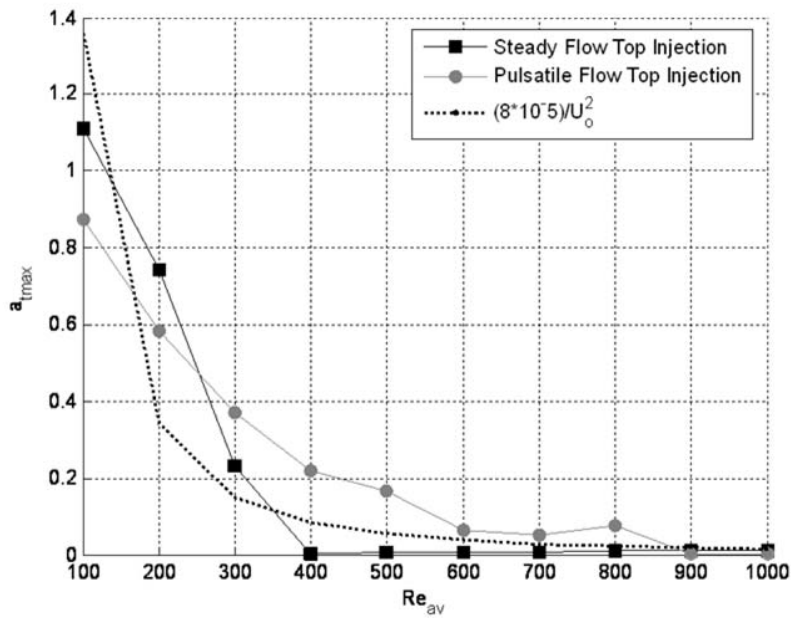


Figure 5.12. Plot of the maximum size attained by the aggregate taken from the temporal aggregate measurements, normalized by the maximum aggregate size for top injection.

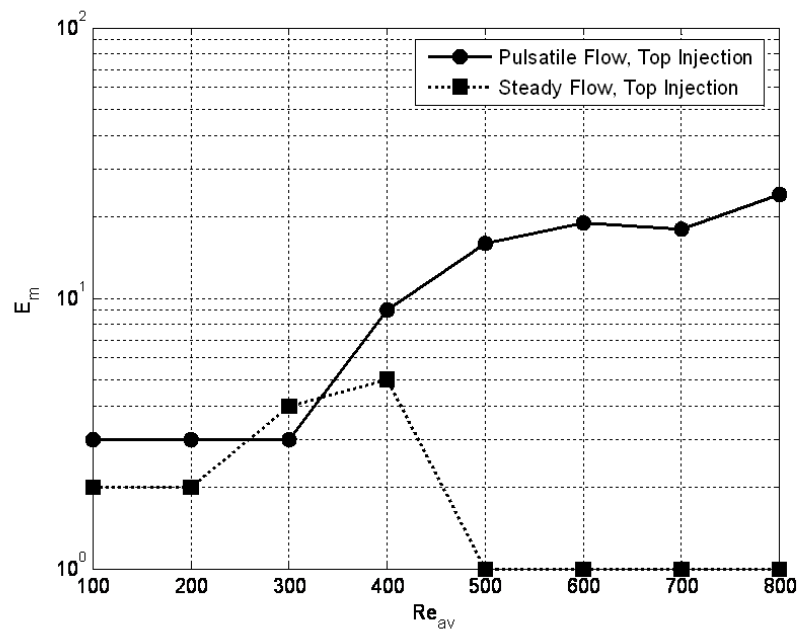


Figure 5.13. Plot of the number of modes required to reconstruct 99.5% of the energy of the interface for steady and pulsatile flow for top injected ferrofluid.

5.7 EFFECT OF MAGNETIC FIELD GRADIENTS ON ACCUMULATION DYNAMICS

Five different magnetic field gradients were studied in this experiment, which were selected based on characterization of the magnetic field inductance in the z-direction, B_z , which is oriented orthogonal to the streamwise direction of flow. In addition to a B_{\max} of 0.15 Tesla utilized in both the top and bottom injection data presented thus far, the four other maximum field strengths at the inner test section wall are 0.075, 0.0225, 0.3, and 0.375 Tesla. These fields are created by adjusting the vertical distance of the magnet tip relative to the test section, with the maximum field strength of 0.375 Tesla representing that where the magnet tip is in contact with the outer test section wall.

The results of the five different field gradients for steady flow Reynolds numbers of 200 are shown in Figure 5.14. No clear differences in aggregate behavior are observed for this Reynolds number in both steady and pulsatile flow, where a similar set of curves are obtained as in Figure 5.14. The main effect that occurs at a Re_{av} of 200 is the development of a slightly larger aggregate for stronger magnetic fields. The volume of aggregate is the same, but the aggregate interaction with the bulk flow is strengthened and additional stretching of the aggregate occurs. Moreover, increasing field gradients results in increased magnetic body forces, and therefore, a more cohesive aggregate.

Plots showing the effect of field gradients for a steady flow Reynolds number of 300 and 400 are shown in Figure 5.15 and Figure 5.16. Here, the variation of magnetic field gradients makes a distinct impact on the stability of the aggregate. For a Reynolds number of 300, an increase of magnetic field strength to 0.225 Tesla from 0.15 Tesla results in an increased ferrofluid size and stability as the aggregate does not experience decay. However, as the field gradients are increased further, the aggregate does not reach the same apparent size, and remains stabilized for field gradients of 0.3 and 0.375 Tesla, compared to the destabilization and decay observed at 0.15 Tesla. The higher magnetic field gradients deform the ferrofluid streakline, causing the streakline to merge with the aggregate at a greater height. The higher streakline energizes the interface as it flows into the aggregate, and a portion of the streakline to wash over the aggregate, and downstream. For a Reynolds number of 400, a similar trend is observed where increasing the magnetic fields from 0.15 Tesla initially assists in increasing

aggregate size and stability. However, increasing to the maximum field strength results in limited aggregate stability, as the aggregate attains a much smaller maximum size.

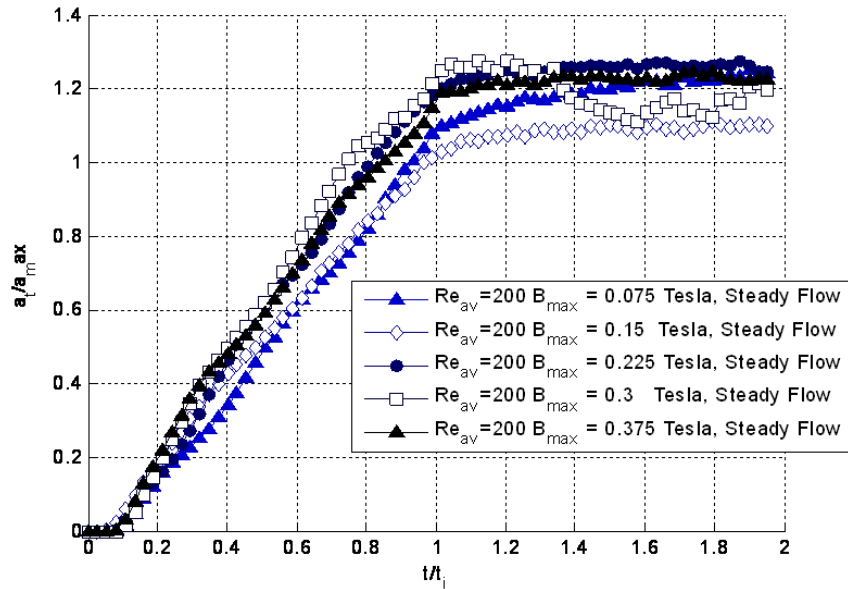


Figure 5.14. Effect of five different field gradients on the normalized aggregate sizes.

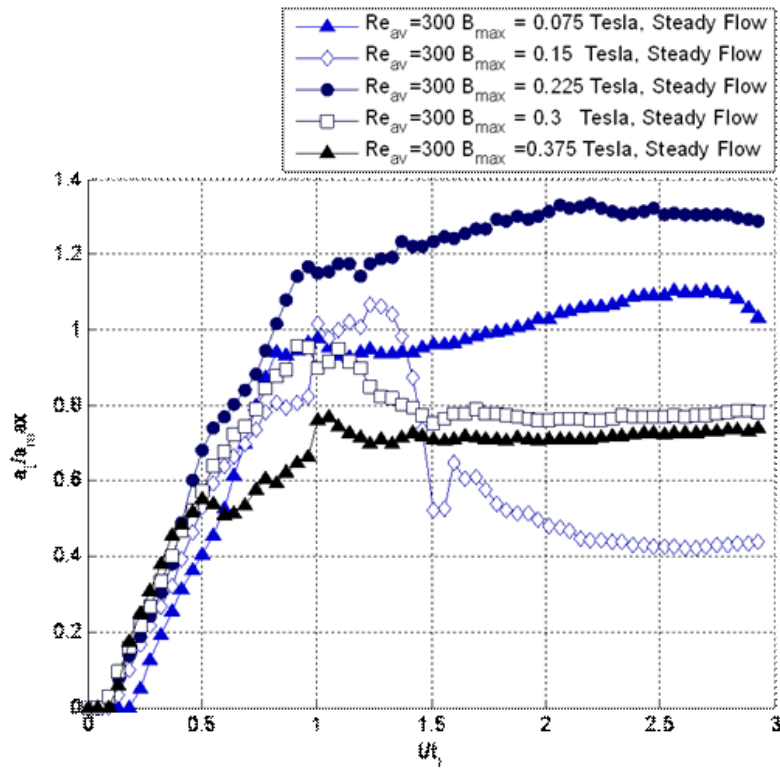


Figure 5.15. Normalized aggregate size versus normalized time for steady flow Reynolds number of 300, illustrating the effect of field gradients.

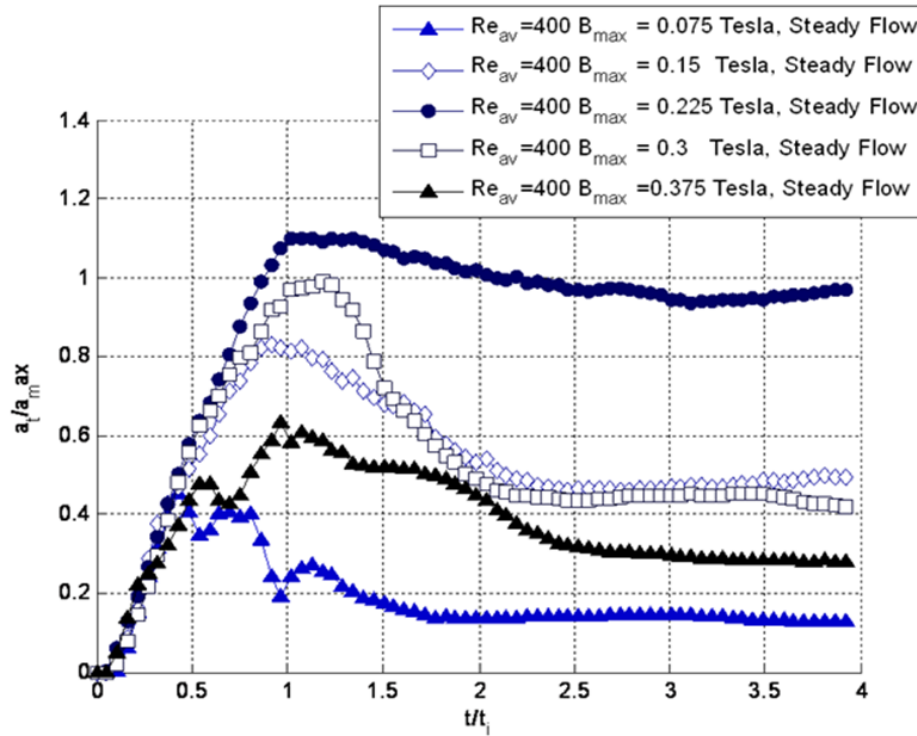


Figure 5.16. Effect of field gradients for a Reynolds number of 400 in steady flow.

In pulsatile flow, a set of curves is obtained for Reynolds numbers of 300 and 400 where the stretching and coalescence of the aggregate is visualized as with previous cases of pulsatile flow, shown in Figure 5.17 and Figure 5.18. An increase of magnetic field gradients initially results in an increase in apparent aggregate size. However, increased maximum field strengths above 0.15 Tesla also results in a decreased ability to retain aggregates, similar to lower field strengths. Unlike in steady flows at these Reynolds numbers, the pulsatility also destabilizes the aggregate and results in additional decay. This effect is especially emphasized at the lowest field strength of 0.075 Tesla, where in steady flow at a Reynolds number of 400, the aggregate stabilizes at a relative size of 0.12, while in pulsatile flow, the aggregate is completely decayed. Moreover, these two pulsatile cases show that while a stable aggregate at a normalized size of 1.15 may be obtained after a normalized time of 1.2 for an average Reynolds number of 300, at a Reynolds number of 400, the aggregate washes away rapidly for B_{max} of 0.3 Tesla. These two cases support for the observations for steady flows, where magnetic forces must remain in balance with inertia in order to retain a stable aggregate. The higher Reynolds number case coupled with pulsatility results in a rapidly decaying aggregate and the K-H instability.

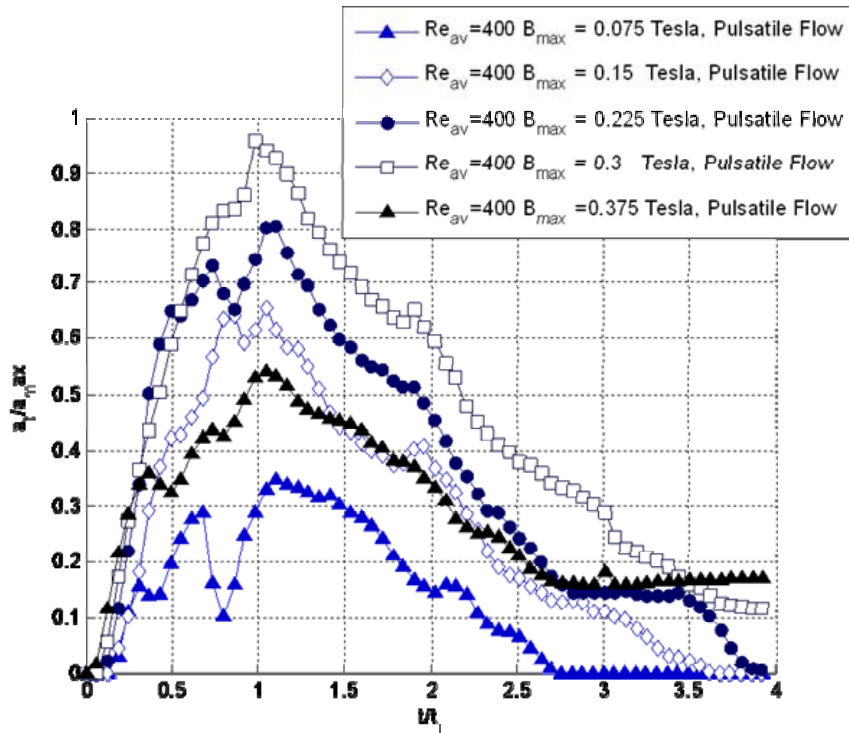


Figure 5.17. Effect of field gradients for a Reynolds number of 400 in pulsatile flow.

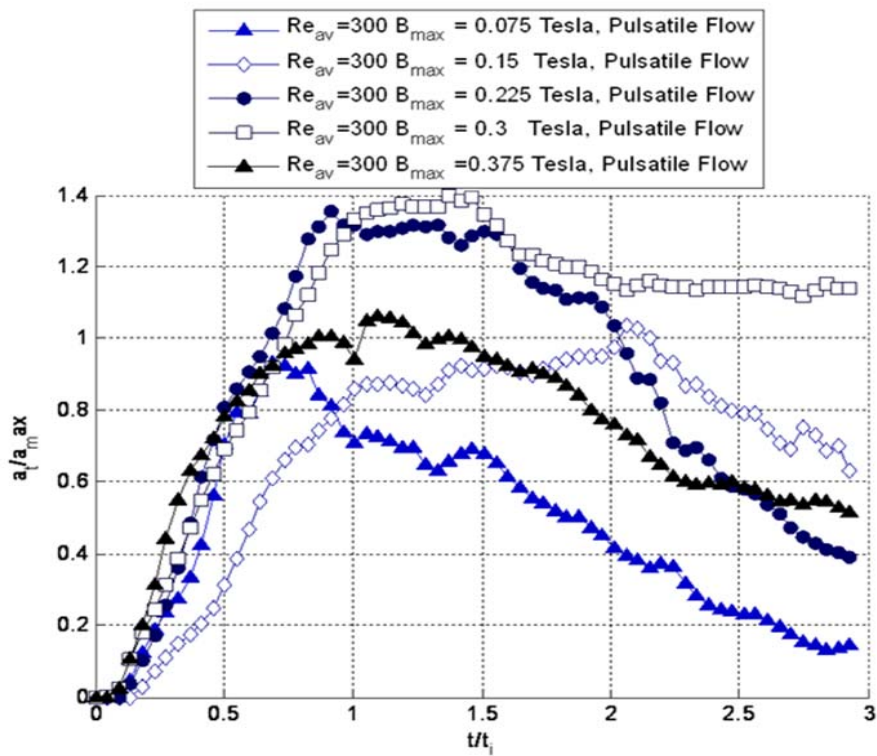


Figure 5.18. Effect of field gradients on ferrofluid aggregates for a Reynolds number of 400 in pulsatile flow.

5.8 DISCUSSION

The results shown in this paper have illustrated how accumulation of ferrofluid aggregates can be differently influenced by the bulk flow conditions, injection location of the ferrofluid, and changing the magnetic field gradients. When the ferrofluid is injected from the bottom of the test section, the aggregate increases in size over the span of the injection. As injection ceases, the aggregate begins to decay, as ferrofluid washes away from the main aggregate. For cases of Reynolds numbers above 300 in both steady and pulsatile flow, a reduction in the aggregate retained during injection occurs due to the increased inertia and therefore limits the ability of the magnet to capture the ferrofluid. Flow pulsatility is also seen to be a factor in further degradation of the aggregate when compared to the same average Reynolds number for steady flows. The degradation is attributed to the peak flows resulting in higher shearing of the aggregate interface.

Injecting the ferrofluid from the top wall of the test section results in diminished aggregate sizes compared to injecting ferrofluid from the bottom of the test section. As the ferrofluid enters opposite to the magnet, it must be drawn through the bulk flow before it reaches the high magnetic field gradients needed to create and retain an aggregate. Top injection also results in the development of the Rayleigh-Taylor instability as ferrofluid is accelerated orthogonally with respect to the flow. Steady flows provide for aggregate accumulation for Reynolds numbers up to 300 for top injection of ferrofluid. Beyond that Re , the flow momentum is too great to be overcome by magnetic body forces, and significant amounts of ferrofluid are not accumulated by the magnet. Increasing the field strength is likely to improve the size of the aggregate captured both for the higher Reynolds number cases. For both top and bottom injection of ferrofluid, flow pulsatility has the effect of driving down the aggregate size, even though for top injected ferrofluids it can initially be responsible for assisting to accumulate that aggregate.

The effect of field strength can bolster the aggregate size, as well as limit its accumulation as well as cause K-H shedding. Previous analytical studies of the K-H instability in ferrofluids have shown that tangentially-applied fields have a stabilizing effect, whereas in this experiment, we have applied a normally-oriented magnetic field. Therefore, we would expect

that as we increase the field gradients that a destabilization of the aggregate would occur. This is precisely what is observed for the plots examining the effect of magnetic field strengths for Reynolds number of 300 and 400. One expected effect is that a balance between the flow inertia and magnetic forces may be created in such a way as to maximize the aggregate size and stability. The effect of field strength study illustrates this concept, as particularly in steady flow, one magnetic field strength between the highest and lowest tested resulted in a large, stable aggregate. Moreover, the field strength needed to reach this equilibrium increases as the Reynolds number is increased from 300 to 400, as required to maintain balance between the magnetic body forces and shearing.

The regions of stable aggregates over the range of the magnetic field strengths and Reynolds numbers examined herein are described by the normalized pressure, P_{norm} , written as

$$P_{norm} = \frac{B_z^2}{\rho \mu U_s^2} \tag{5.3}$$

where B_{max} is the maximum magnetic field strength in Tesla at the inner test section wall; the maximum field strength to which the aggregate is subjected. U_o is the mean bulk flow velocity. P_{norm} is plotted versus the Reynolds number in Figure 5.19 for bottom-injected ferrofluid aggregates. An area plotted over P_{norm} indicates the development of an aggregate that retains at least 50% of its maximum size over the length of data acquisition.

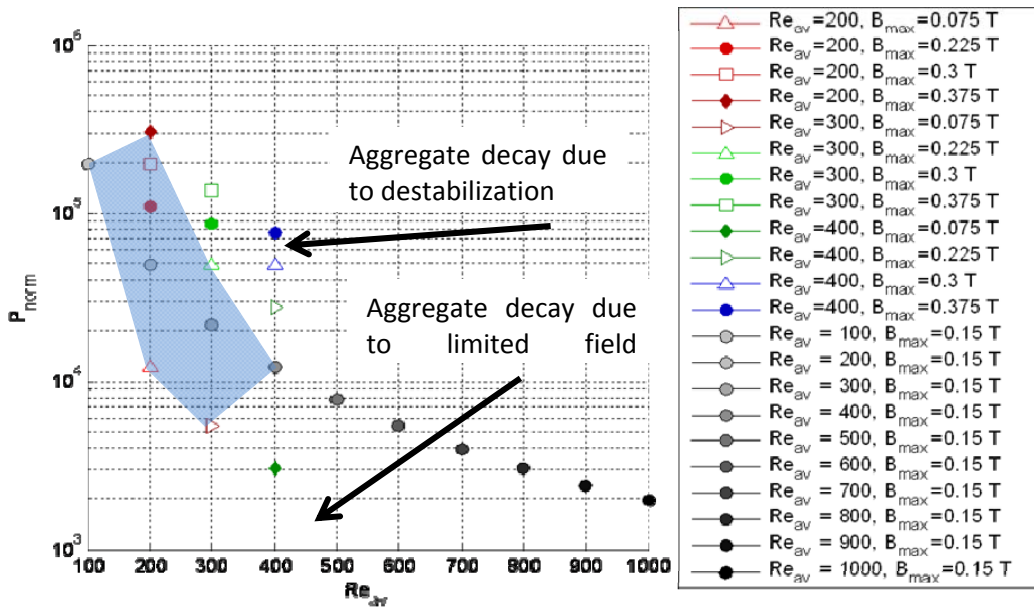


Figure 5.19. The normalized pressure versus the Reynolds number for all Reynolds numbers and field strengths for steady flow cases.

For very low magnetic fields, the aggregate accumulates to a limited degree. Even so, the aggregate can decay as the drag forces due to aggregate blockage generate shearing stresses. In contrast, the high magnetic field gradients foster the destabilization of the aggregate, and therefore, its dispersion. Based upon these experimental results, values of P_{norm} within the envelope for those specified Reynolds numbers of 400 and under are expected to remain stable.

5.9 CONCLUSIONS

Herein, the effects of many different parameters on the accumulation and residence time of ferrofluid aggregates have been examined using focused shadowgraphs. Post-processing of the frames provides insight into aggregate physics by sizing the aggregate in time as well as determining the aggregate interface behavior. In accumulation, Kelvin-Helmholtz shedding is prevalent in ferrofluid aggregates dispersing in bulk flows for Reynolds numbers 300 and greater under certain conditions, including unsteady flows.

Several conclusions can be drawn about the effect of different conditions on the impact of the aggregate, which are summarized as follows:

- A. Steady bulk flows with bottom injected ferrofluid favors aggregate accumulation, while pulsatility assists in driving aggregate instability and decay.
- B. Pulsatile bulk flows with top injected ferrofluid improves aggregate accumulation compared to steady flow, but the aggregate is ultimately washed away due to the unsteady effects.
- C. The effect of field gradient has similar impacts on aggregates subjected to both steady and unsteady bulk flows.
- D. An optimum normalized pressure exists based on the bulk flow inertia, where values of magnetic field gradients result in limited accumulation, while high gradients result in aggregate instability.

5.10 REFERENCES

1. Popplewell, J., *Technological applications of ferrofluids*. Physics in Technology, 1984. 15(3): p. 150-156
2. Pacitto, G., et al., *Rayleigh-Taylor instability with magnetic fluids: Experiment and theory*. Physical Review E, 2000. 62(6): p. 7941.
3. Malik, S.K. and M. Singh, *Finite amplitude Kelvin--Helmholtz instability in magnetic fluids*. Physics of Fluids, 1986. 29(9): p. 2853-2859.
4. Ganguly, R., A.P. Gaiind, and I.K. Puri, *A strategy for the assembly of three-dimensional mesoscopic structures using a ferrofluid*. Physics of Fluids, 2005. 17(5): p. 057103-9.
5. Ganguly, R., B. Zellmer, and I.K. Puri, *Field-induced self-assembled ferrofluid aggregation in pulsatile flow*. Physics of Fluids, 2005. 17(9): p. 097104-8.
6. Williams, A.M., Stewart, K. and Vlachos, P., November 2007, *The Dynamics of Agglomerated Ferrofluid in Pulsatile flows*. APS Division of Fluid Dynamics 60th Meeting, Salt Lake City, UT.
7. Otsu, N., *A Threshold Selection Method from Gray Level Histograms*, IEEE Transactions on Systems, Man, and Cybernetics, Vol. 9, No. 1, 1979, pp. 62-66
8. Sirovich, L., K.S. Ball, and L.R. Keefe, *Plane waves and structures in turbulent channel flow*. Physics of Fluids A: Fluid Dynamics, 1990. 2(12): p. 2217-2226.
9. Adrian, R. J., K. T. Christensen, et al. *Analysis and interpretation of instantaneous turbulent velocity fields*. Experiments in Fluids, 2000. 29(3): 275-290.
10. Berkooz, G., P. Holmes, and J.L. Lumley, *The Proper Orthogonal Decomposition in the Analysis of Turbulent Flows*. Annual Review of Fluid Mechanics, 1993. 25(1): p. 539-575.
11. Meyer, K.E., J.M. Pedersen, and O. Ozcan, *A turbulent jet in crossflow analysed with proper orthogonal decomposition*. Journal of Fluid Mechanics, 2007. 583, pp 199-227.

6 THE THREE-STAGE INTERACTION OF FERROFLUID AGGREGATES WITH PULSATILE FLOWS

6.1 ABSTRACT

Experimentally resolving the spatiotemporal dynamics of ferrofluids has proven elusive due to their opacity. These dynamics remain important factors in the application of ferrofluids to mixing, heat transfer, medical devices, and others. To date, experimental techniques have been predominantly limited to free surface measurements, ultrasonically-measured velocity profiles, and pressure distributions. Herein, the first spatiotemporally resolved planar measurement of the internal flow structure of magnetized ferrofluid aggregates interacting with a bulk flow of low magnetic susceptibility are presented. The flow was measured using Time Resolved Digital Particle Image Velocimetry (DPIV) with 200 Hz single-pulsed sampling to resolve the region of bulk flow as well as the flow internal to the ferrofluid aggregate. The resulting data illustrates the dynamic interaction of the accumulated ferrofluid aggregate with a bulk pulsatile flow of water. Three main structures that appear in these flow fields are the suction, roll up, and ejection of ferrofluid aggregate depending on the instantaneous flow rate. The appearance of these structures is driven by the flow inertia. The strength of the vortical structures within the aggregate is out of phase with the flow rate, and the suction vortex corresponds to the peak circulation within the aggregate, enabling the appearance of secondary structures that lead to the roll up and ejection of ferrofluid.

6.2 INTRODUCTION

Ferrohydrodynamics is dedicated to the study of fluids that can be strongly magnetized in the presence of applied magnetic fields. Often, these fluids are comprised of superparamagnetic nanoparticles, which become highly magnetized under magnetic fields but return to their initially unmagnetized state once the field is removed. Surfactant coatings

combined with Brownian motion allow the particles to remain in a stable suspension, even when magnetized. The research of magnetic fluids encompasses basic ferrofluid mechanics and composition to different hydrodynamic instabilities [1,2,3]. The magnetizability of ferrofluids also provides a route for either the amplification or control of such instabilities based on the properties of the magnetic field.

Many new technologies have been developed as a result of over 40 years of ferrohydrodynamics research such as dampers and seals with improved characteristics and service life [4]. One of the newer and most promising applications of ferrofluids is Magnetic Drug Targeting (MDT) [5]. MDT is a means to utilize ferrofluids in conjunction with magnetic fields to target drug therapies within the body. The ferrofluid, which can be sized down to nanometer scales, can be reversibly bonded to medicinal agents, and carries drugs to target sites where they are retained by magnetic forces in aggregates. The targeting of such therapy enhances the efficacy of the drug while minimizing its toxicity to healthy tissues and organs [6]. In vivo studies have examined the use of ferrofluids functionalized with chemotherapies with promising results, using 50% or less of the typical systemic dose to achieve remission of tumors in laboratory animals [7,8].

However, of the experiments that have been published in ferrohydrodynamics, a very limited body of work has focused on the mechanics of ferrofluids interacting with bulk flows [9,10]. Moreover, experiments studying ferrohydrodynamics have applied a limited group of techniques which have been primarily limited to ultrasonic point measurements [11], free surface measurements [12], and shadowgraphs of the free surfaces of ferrofluids. Usage of advanced optical measurement techniques such as Digital Particle Image Velocimetry (DPIV) has been circumvented in ferrohydrodynamics due to the opacity of ferrofluids. In this work, we obtain Time Resolved DPIV (TRDPIV) measurements [13-14] of the ferrofluid aggregate as a result of its limited size compared with our measurement plane. To date, only one other published paper has used the DPIV technique to investigate ferrofluid or ferroparticle dynamics, which was a proof of concept experiment that studied Poiseuille flow mixed with ferroparticles at the microscale [15]. Out of the results presented herein, we observe the rich three-stage interaction of ferrofluid aggregates in pulsatile flows, as revealed for the first time by spatiotemporally resolved flow measurements.

6.3 EXPERIMENTAL METHOD

Herein, water-based ferrofluid with 10 nanometer-sized particles (EMG-705, Ferrotec, Inc) mixed with 10 micron neutrally-buoyant flow tracers were injected in a streakline into the 10 mm diameter test section in initially-quiescent flow. An aggregate of the injected ferrofluid was retained by a 0.6 Tesla permanent magnet, oriented obliquely such that the magnetic field is predominantly in two dimensions. After the aggregate was accumulated, flow was ramped up and set to the specific flow waveform for each case and 6000 frames were acquired, capturing the motion of the flow tracer particles, corresponding to 35 seconds of real-time sampling. Two pulsatile flow conditions were examined in this work for Reynolds numbers based on the average flow rate of 400 and 600 and the channel diameter of 10 mm. The kinematic viscosity comes from the standard properties of water, as it was utilized as the bulk flow medium. The bulk flow rate was verified by use of a Transonic Systems ultrasonic flow meter, which is accurate to 10% of the measured flow for the flow rates undertaken in this experiment.

The flowfields were measured in a spatiotemporally resolved plane of velocity measurements single-pulsed with TRDPIV (Time Resolved Digital Particle Image Velocimetry). A coherent light source in the form of a 532 nm wavelength Nd:YAG laser was expanded into a 1 mm thickness plane and aligned streamwise to the flow direction, coincident to the centerline of the tube. The data was obtained using a high speed IDT XS-5 camera sampling at 200 frames per second. A schematic of the setup utilized for data acquisition is shown in Figure 6.1. The data was processed using passes of 64 by 32 and 32 by 16 pixel windows with a vector spacing of 4 pixels, corresponding to a resolution of 140 μm . The data was processed using the Robust Phase Correlation (RPC) algorithm, which is effective for processing frames with high noise levels, as occur within the region of the aggregate [16].

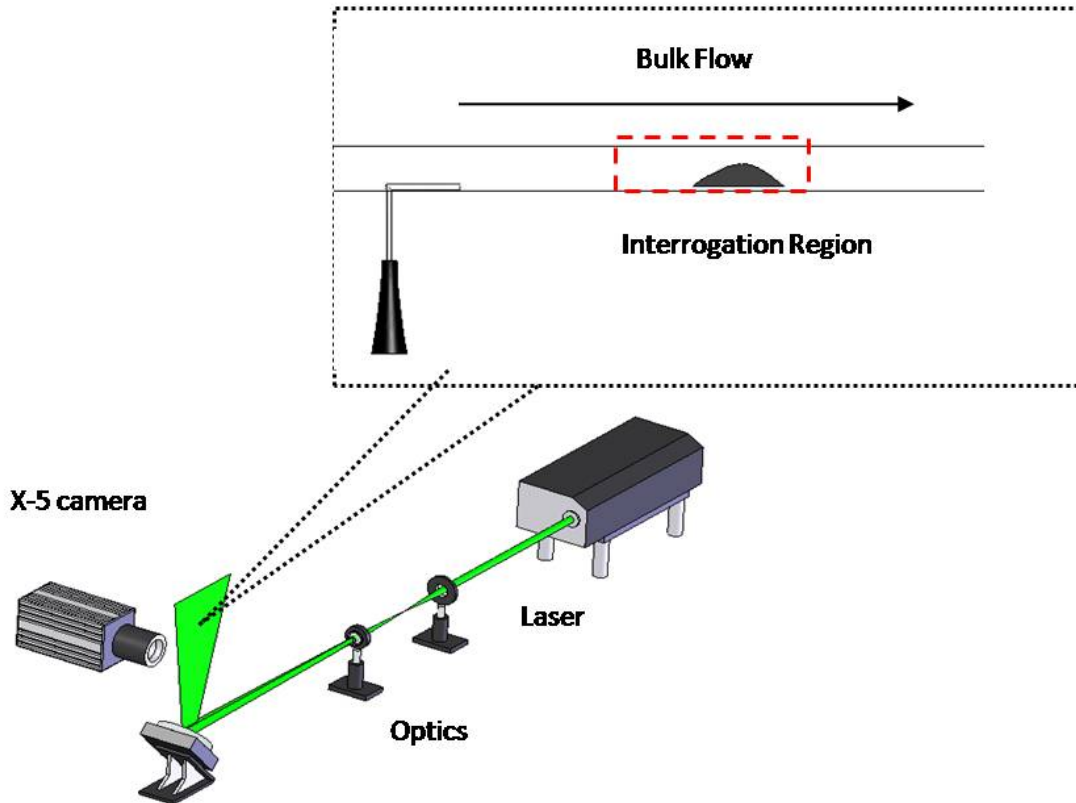


Figure 6.1. Experimental schematic for TRDPIV data acquisition.

6.4 RESULTS

Raw digital frames that demonstrate the physics of ferrofluid aggregates in pulsatile flow for a Reynolds number based on average flow rate of 400 are shown in Figure 6.2. These images illustrate the multi-stage interaction between the ferrofluid and bulk flow. In Figure 6.2, the aggregate is shown at 5 seconds after flow startup, at the bottom of the channel near the magnet. The ferrofluid appears in these images as a gray to black colored material, depending on its local concentration. The bulk flow, flowing from right to left, is mixed with the 10 micron flow tracers. The flow tracers are depicted as localized bright regions the size of a few pixels. From Figure 6.2A-F we observe the ferrofluid aggregate stretching and coalescing as a function of the flow rate.

The length of the straight arrows in Figure 6.2 depicts the relative velocity of the incident flow over the aggregate for each frame. During peak flow, in Figure 6.2A, the aggregate shears

downstream, and it stretches as it shears. As flow begins to slow, the aggregate begins to coalesce in Figure 6.2B due to the magnetic body forces drawing the aggregate back towards the magnet location. The shear layer convection in the downstream direction interacts with the recirculation of the ferrofluid in the upstream direction to generate a recirculation region, shown in Figure 6.2B. As flow slows further in Figure 6.2C, the recirculation vortex expands and then lifts off from the test section wall in Figure 6.2D. The lift-off of the vortex results in secondary flow generation and the vortices present in the aggregate are shed downstream in Figure 6.2E as flow ramps up towards its peak value.

The post-processed vorticity contours corresponding to the raw frames in Figure 6.2 are shown in Figure 6.3. The magnet tip is located at x and y coordinates of [0, 0], and the distances are normalized with respect to D_h . Figure 6.3A illustrates the peak flow process, which will henceforth be referred to as ejection. The shear layer remains visible in that a region of positive vorticity surrounds the approximate aggregate region. In Figure 6.3B, after flow slows, the formation of a primary vortex in the shear layer appears that encompasses the region of the ferrofluid aggregate. This vortex enlarges as the time-varying flow rate decreases to its lowest level in Figure 6.3C. Suction from the primary vortex results in an entrainment jet that stretches the primary vortex and fosters liftoff of the vortex from the wall in Figure 6.3D. The primary vortex stretches until it cleaves into two smaller cat-eye structures as the fluid packet begins to separate from the wall. In turn, the entrainment jet generates a vortex rotating clockwise and opposite-sensed to the primary vortex near the wall. This counter-rotating vortex results in the cutoff of vorticity supply of the top two vortices, and their strength decreases precipitously. The top two vortices are convected downstream in the negative x direction as flow ramps up to the ejection process in Figure 6.3E. The process repeats for the duration of the data acquisition as for this flow rate, only small amounts of aggregate are washed away during ejection in Figure 6.3F. Although there are several different fluid structures that form and are shed as the aggregate coalesces and stretches, the three fundamental interactions are identified as the suction, roll up, and ejection of the ferrofluid aggregate.

The raw images illustrating the interaction between the bulk flow and ferrofluid aggregate for a Reynolds number of 600 are shown in Figure 6.4A, B, and C illustrate the suction, roll up, and ejection processes that similarly occurred for a Reynolds number of 400. The corresponding vorticity contours are shown in Figure 6.5. Compared to the results for a Reynolds number of 400, the vortices are less developed for the suction, roll up, and ejection

processes, as the aggregate is sheared more by the higher peak flows for an average Re of 600. However, the fundamental structures and interaction between the ferrofluid aggregate and bulk flow remain the same.

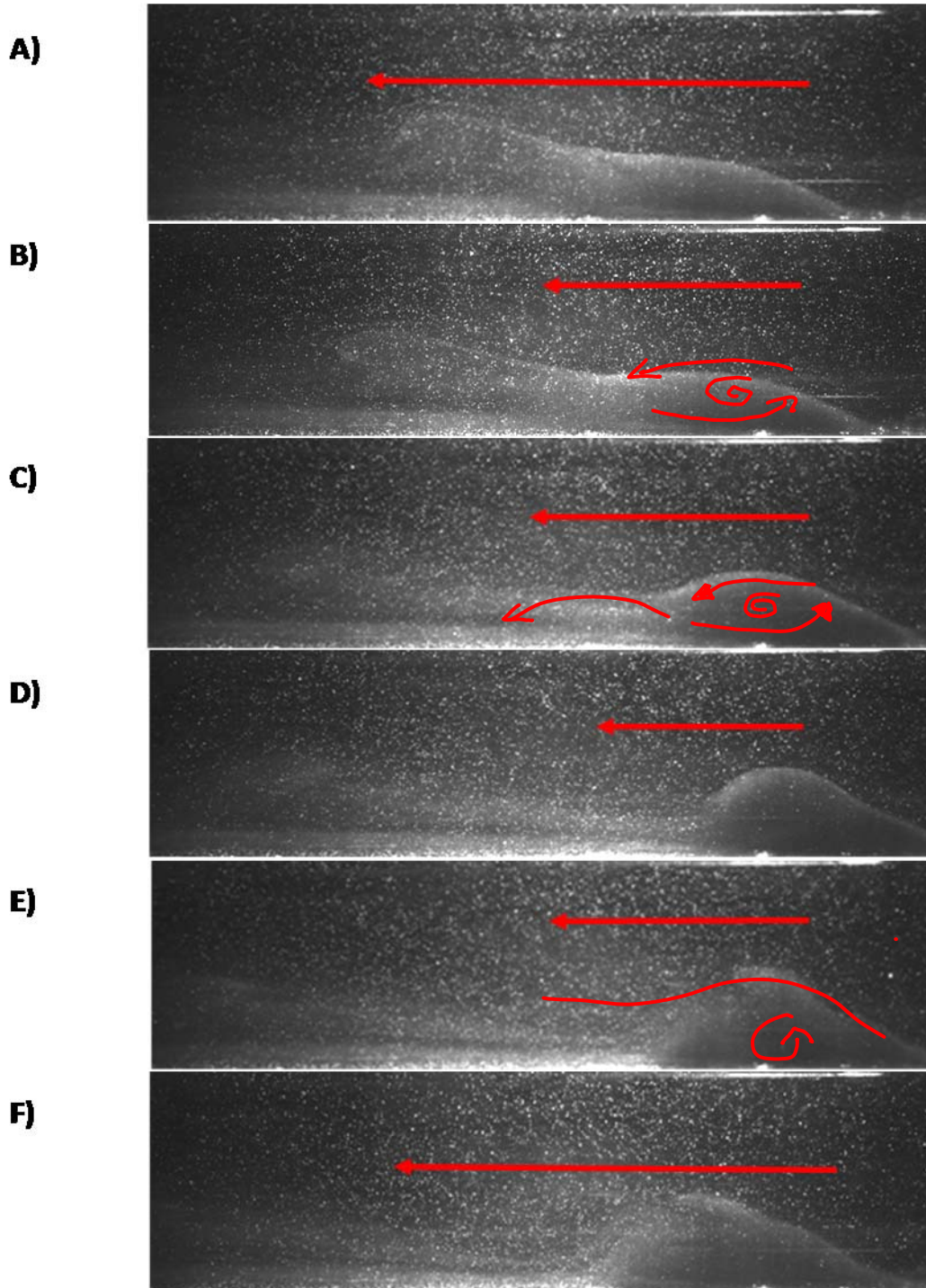


Figure 6.2. Raw TRDPIV images illustrating the ferrofluid (gray material) interacting with the bulk flow, seeded with tracer particles appearing as intensely illuminated pixels.

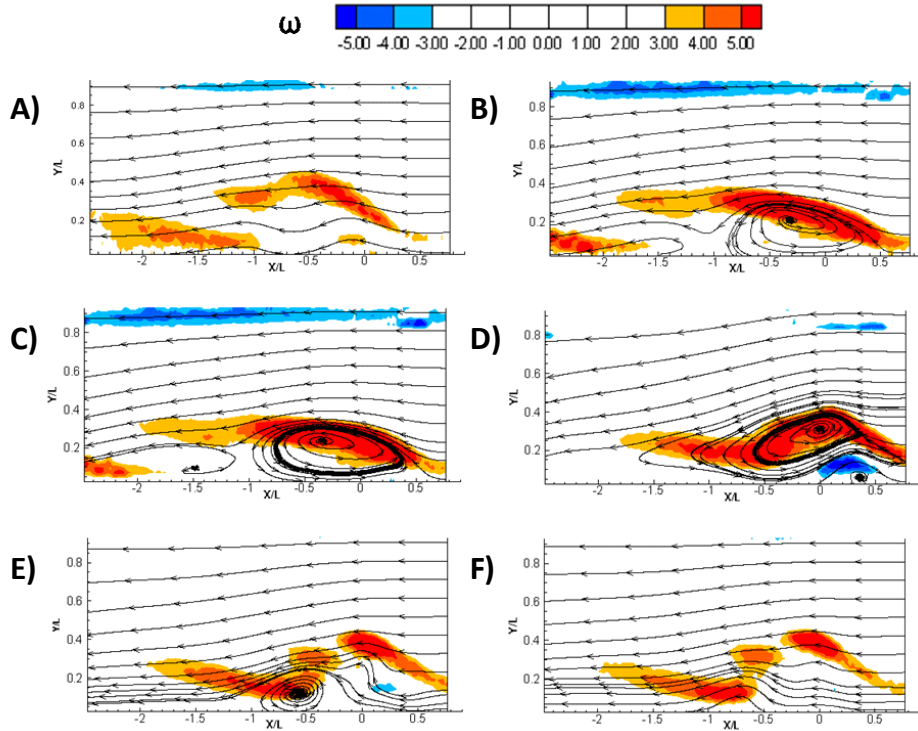


Figure 6.3. Contours of vorticity illustrating the three-stage process for $Re_{av} = 400$. The large primary vortex develops during the suction phase, or the period of lowest bulk flow.

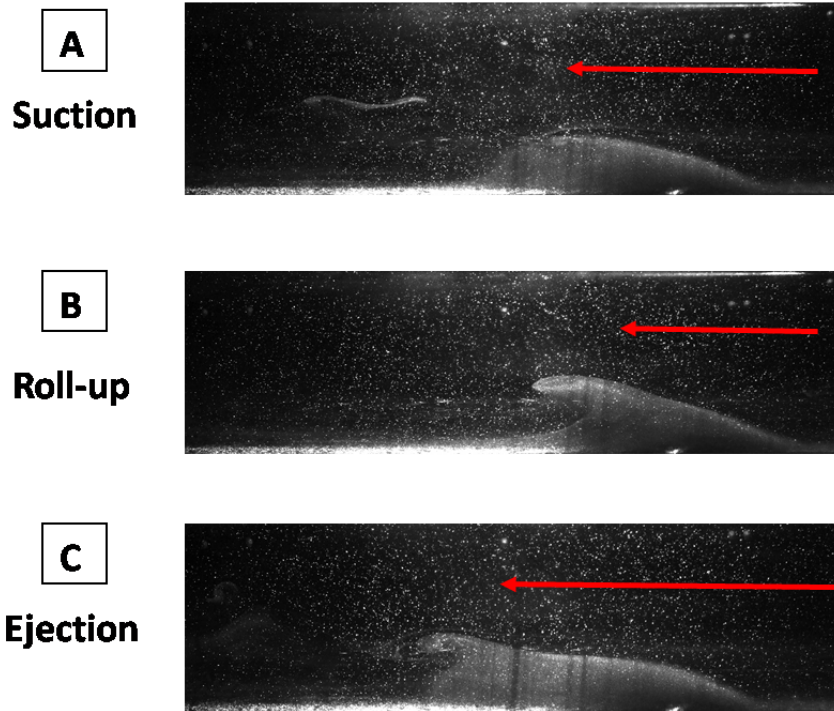


Figure 6.4. Raw frames showing the three-stage interaction in response to flow pulsatility for an average Reynolds number of 600.

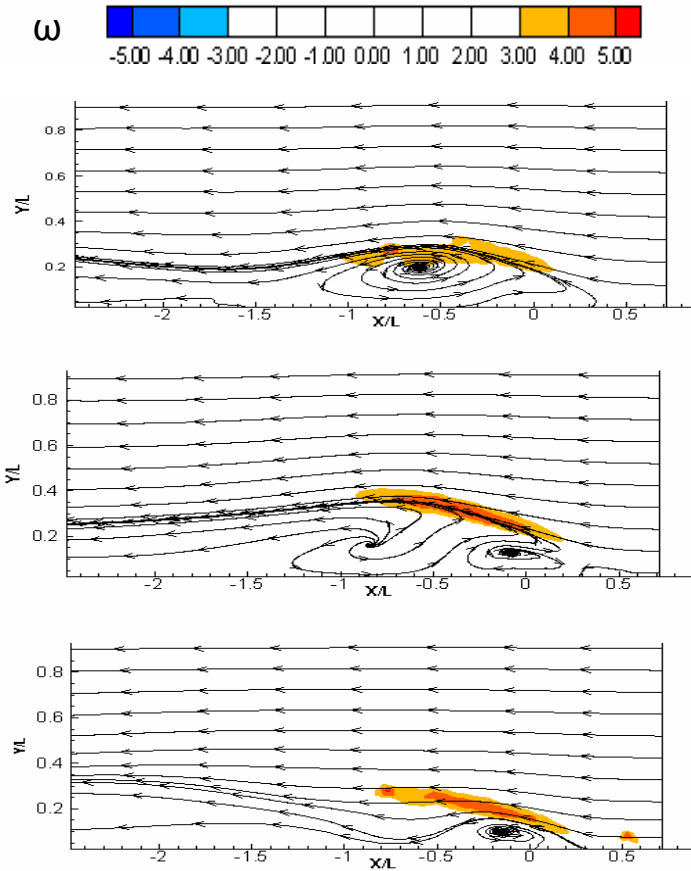


Figure 6.5. Contours of vorticity for an average flow-based Reynolds number of 600.

6.5 VORTEX IDENTIFICATION

To confirm the three-stage interaction by the way the dynamics of the vortices, vortex identification was performed using the Δ criterion, wherein vortices are distinguished by streamlines that curl in towards each other [17,18]. The Δ criterion mathematically finds vortices by identifying regions of the flow in which eigenvalues of the velocity gradient tensor are complex, which has the characteristic equation of

$$\lambda^3 + P\lambda^2 + Q\lambda + R = 0$$

6.1

where P, Q, and R are invariants of the velocity gradient tensor. Based upon the decomposition in Equation 6.1, the Δ criterion is calculated for incompressible flows by

$$\Delta = \left(\frac{1}{3}\right)Q^3 + \left(\frac{1}{2}\right)R^2 > 0 \quad 6.2$$

where positive Δ indicate complex eigenvalues and the location of a vortical region. The Q and R parameters are calculated by

$$Q = \frac{1}{2}(\|\Omega\|^2 + \|S\|^2) \quad 6.3$$

$$R = \text{Det}(U_{ij}) \quad 6.4$$

where S and Ω are the symmetric and antisymmetric parts of the velocity gradient tensor.

The delta criterion was applied to all time steps from the post-processed velocity fields to locate vortices within each velocity field. The vortex centers were calculated by finding the centroid of the polygon outlining the detected vortex boundaries. The circulation of each of the vortices is computed in the region of the vortex by performing a line integral around the identified vortex outline. The maximum circulation of the vortices was computed for all snapshots of the flow and these are plotted with the measured flow rate for both cases in Figure 6.6 and Figure 6.7 for Reynolds numbers of 400 and 600, respectively. The circulation values shown in the two figures, Γ_{\max} , is normalized by the kinematic viscosity of water. The maximum circulation over time and the flow rate are out of phase for both Reynolds numbers. Consistent with the observations from the vorticity contours, the peak circulation values are lower for a Reynolds number of 600 versus 400.

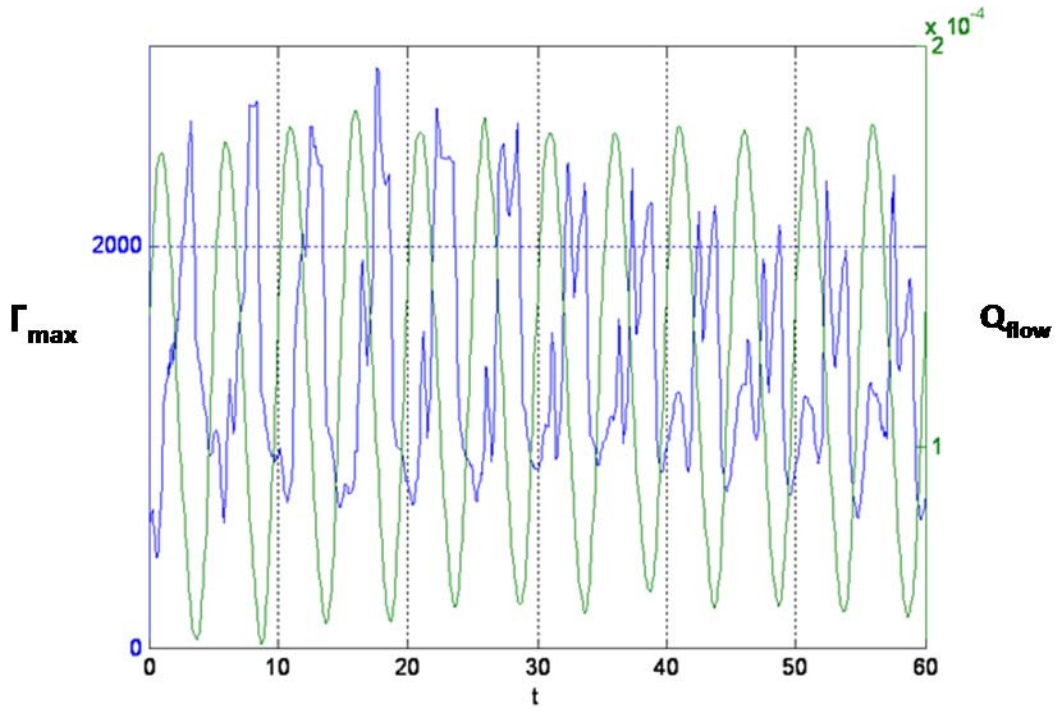


Figure 6.6. Plot of maximum circulation versus time for Re_{av} of 400 with flow rate plotted on right hand axis. Flow and circulation are out of phase.

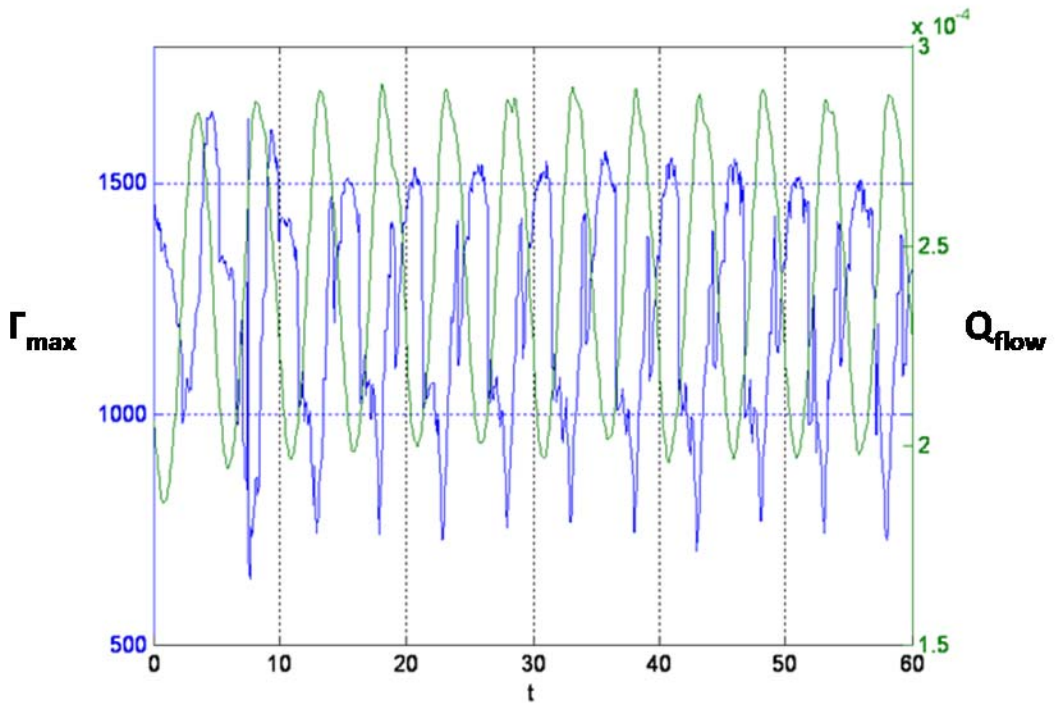


Figure 6.7. Maximum circulation (blue) overlaid with flow rate (green) for Re_{av} of 600.

The identified vortices are plotted along with the circulation in Figure 6.8, corresponding to the three-stage interaction for a Reynolds number of 400. In the case of multiple vortices as in Figure 6.8C, the maximum circulation of the three identified vortices is plotted instead. For peak flow, relatively low circulation of the vortex identified in the shear region of the aggregate occurs in Figure 6.8A, while the suction vortex in Figure 6.8B represents the maximum circulation over a period of pulsatile flow. The peak circulation of the suction vortex is the enabling mechanism for the entrainment jet formation and therefore, the roll up of the primary vortex and generation of a secondary vortex.

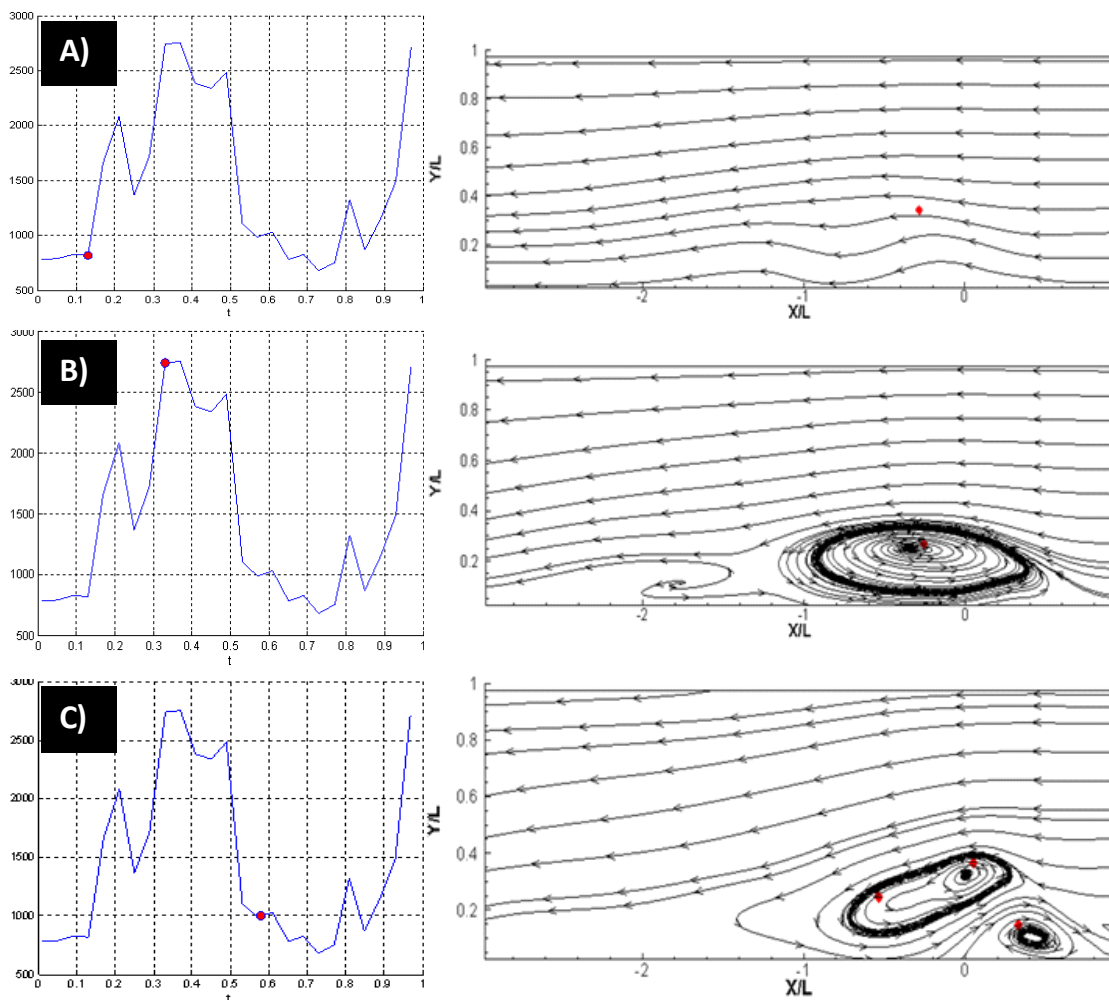


Figure 6.8. Snapshots showing streamtraces with vortex centers identified by red dots for the three-stage interaction for a Reynolds number of 400 with circulation.

As the relationship between the maximum circulation and flow rate are out of phase over the length of the acquired data in Figure 6.6 and Figure 6.7, the peak circulation values remain relatively stable over time. However, the pulsatile flow can result in the decay of the aggregate as it washes away due to the ejection of ferrofluid at the peak flow rate. Figure 6.9 provides a comparison between two images 15 seconds after flow start up for both Reynolds numbers during the ejection process. The aggregate for Re_{av} of 400 remains substantial compared to the earlier time shown in Figure 6.2, while for Re_{av} of 600, significant dispersion of the aggregate away from the magnet has occurred.

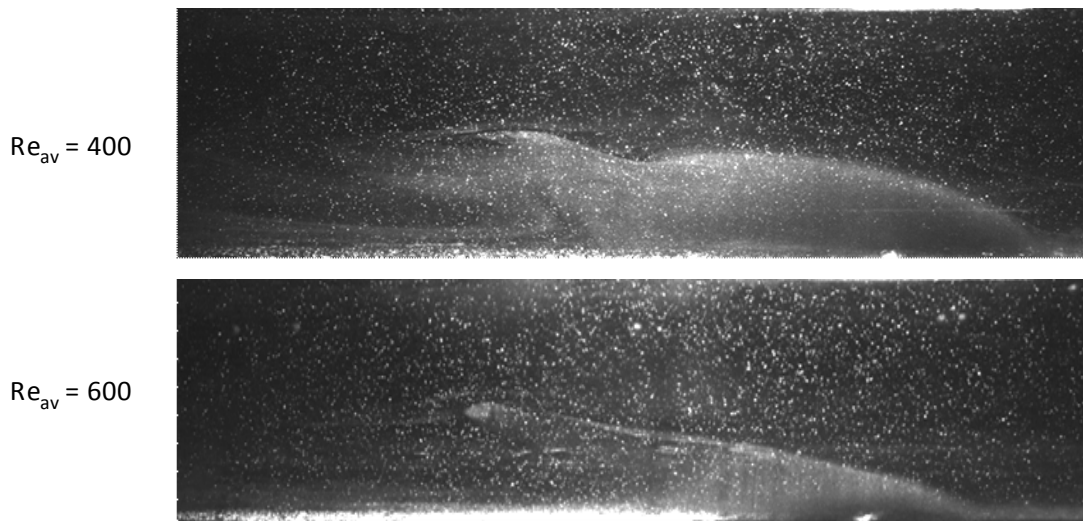


Figure 6.9. Comparison of the relative aggregate sizes for $Re_{av} = 400$ and 600 at 15 seconds after flow startup. Qualitatively, much more of the aggregate has eroded for the higher flow rate although the overall circulation phase driven by the flow rate remains similar.

6.6 PROPER ORTHOGONAL DECOMPOSITION

In the previous section, the time-varying strength of vortices was correlated to the three-stage interaction process. However, this process is also supported by an examination using the Proper Orthogonal Decomposition (POD). POD was performed on the velocity fields in time to develop a low order characterization of the fluid mechanics of the ferrofluid-water system, and the measured flow field is decomposed into its fundamental components using orthogonal basis

functions. The modes are ordered from highest energy in the first mode to lowest in the last mode, and based on the energy captured by the lower modes; reduced-order models can be developed to describe complex systems. Comprehensive reviews of POD are given by Berkooz et al [19,20]. The frames are decomposed into modes with corresponding coefficients of the form

$$y(x, y, t) = \sum_{i=1}^N a_i(t) \varphi_i(x, y)$$

6.5

where α_i are the projection coefficients which describe the time history of the mode shapes, φ_i , that contain only the spatial information of each mode.

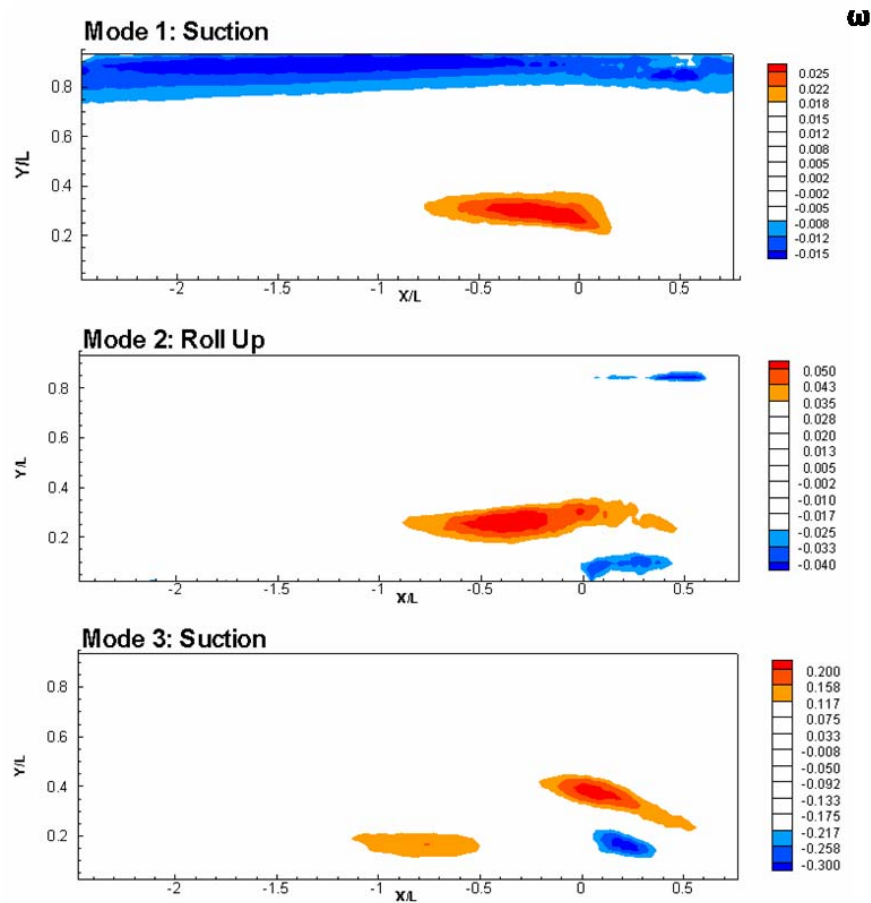


Figure 6.10. Vorticity contours of the three highest energy modes for Re_{av} of 400 corresponding to the three-stage interaction of the aggregate and bulk flow.

Examining the vorticity of the highest energy modes in Figure 6.10 for a Reynolds number of 400, the overall shape can be correlated back to the velocity and vorticity fields that have already been presented. The modes themselves contain only spatial information, so their scales cannot be referenced back to the vorticity plots from the measured velocity fields. In mode 1, the region of high counterclockwise vorticity correlates to the suction process, and is located at the interface of the bulk flow and aggregate. Mode 2 is analogous to the roll up stage, where secondary flow is generated in the form of the counter-rotating vortex appearing as a region of negative vorticity. Finally, Mode 3 is synonymous with ejection, as we see the high positive vorticity region breaks up into smaller regions and convects downstream.

The results obtained using POD are useful to describe the interactions between the different modes or structures in the flow over time using the projection coefficients describing the relative magnitude of compared modes. The projection coefficients for modes 1, 2, and 3 are plotted in Figure 6.11 and Figure 6.12 for Reynolds numbers of 400 and 600, respectively. Each point for these three-dimensional plots is plotted in a grayscale color that starts at light gray for the first time instant and advances to black over time. As is the case for both Reynolds numbers, the phase portraits of the first three modes form a stable limit cycle over time. Each loop of the cycle represents one full period of pulsatility in the bulk flow. Therefore, given that the first three modes of the POD represent the suction, roll up, and ejection of ferrofluid, the stable limit cycle obtained from these phase portraits indicates that the suction, roll up, and ejection interact in a stable, periodic relationship over time.

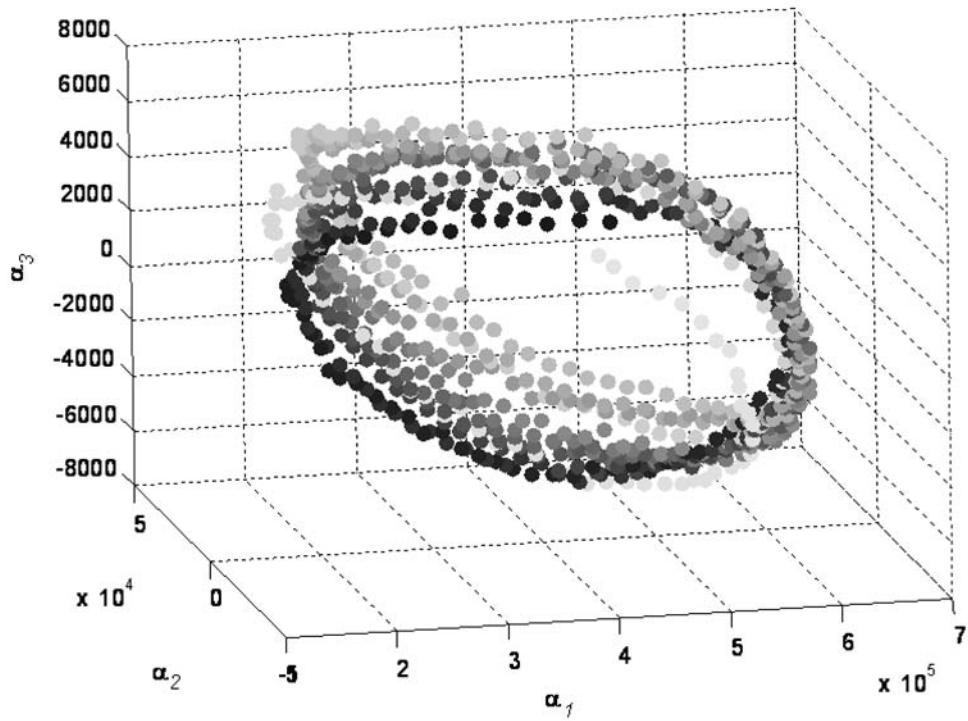


Figure 6.11. Phase portrait for Modes 1, 2, and 3 for Reynolds number of 400.

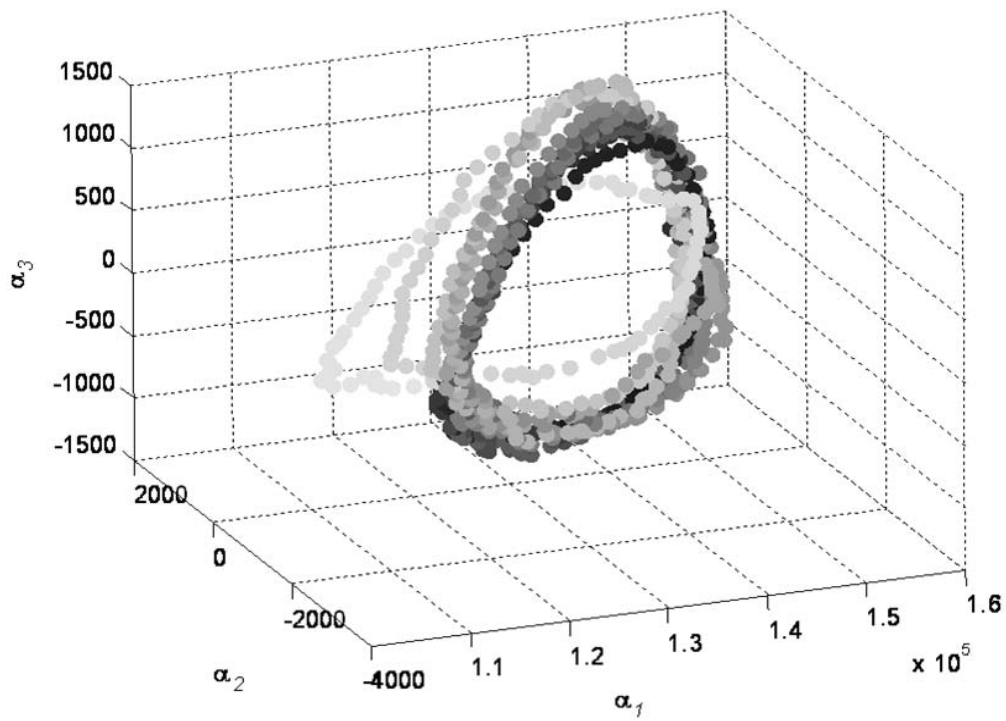


Figure 6.12. Phase portrait for Modes 1, 2, and 3 for an average Reynolds number of 600.

6.7 CONCLUSIONS

Herein, the external and internal dynamics of ferrofluid aggregates retained by a permanent magnet in pulsatile flow with two Reynolds numbers based on mean flow were presented. TRDPIV was used for the first time to characterize these dynamics in ferrofluids. The three-stage interaction between the ferrofluid aggregate and bulk flow was identified by examining the flow fields, the vortex dynamics, and the relationship between the high energy modes by means of POD. The three fundamental motions of the aggregate are described as the suction, roll up, and ejection of ferrofluid in response to the time-varying bulk flow. For an average Reynolds number of 400, an increased circulation of the fluid structures is consistent with lower overall shearing. For an average Reynolds number of 600, the three-stage interaction of the aggregate with the bulk flow is maintained, even as the higher shearing results in increased decay of the aggregate.

These experimental results illustrate the first spatiotemporally resolved ferrohydrodynamics flow, which furthers intuition of ferrofluid aggregate interaction with incident flows. The strong coupling of the aggregate dynamics with the bulk flow is indicated by periodic aggregate behavior with the maximum circulation which is out of phase with respect to the bulk flow. Moreover, even if the aggregate decays, the intensity of circulation is maintained as well as the three-stage process. Examining results from Proper Orthogonal Decomposition, the first three highest energy modes correspond to suction, roll up, and ejection. These modes interact with each other in three dimensions in a steady limit cycle over time as remarked in both the vortex identification and in the velocity fields themselves.

6.8 REFERENCES

-
1. Adrian, R.J., *Twenty years of particle image velocimetry*. *Experiments in Fluids*, 2005. 39(2): p. 159-169.
 2. Abou, *The Normal Field Instability in Ferrofluids: hexagon-square transition mechanism and wavenumber selection*. *Journal of Fluid Mechanics*, 2000. 416: p. 217-237.

-
3. Perry, M.P. and T.B. Jones, *Interfacial parametric ferrohydrodynamics*. Journal of Applied Physics, 1975. 46(2): p. 756-760.
 4. Raj, K. and R. Moskowitz, *A review of damping applications of ferrofluids*. Magnetics, IEEE Transactions on, 1980. 16(2): p. 358-363.
 5. Lubbe, A.S., et al., *Clinical Experiences with Magnetic Drug Targeting: A Phase I Study with 4'-Epidoxorubicin in 14 Patients with Advanced Solid Tumors*. Cancer Research, 1996. 56(20): p. 4686-4693.
 6. Lubbe, A.S., C. Alexiou, and C. Bergemann, *Clinical Applications of Magnetic Drug Targeting*. Journal of Surgical Research, 2001. 95(2): p. 200-206.
 7. Alexiou, C., et al., *Magnetic drug targeting: biodistribution and dependency on magnetic field strength*. Journal of Magnetism and Magnetic Materials, 2002. 252: p. 363-366.
 8. Alexiou, C., et al., *In vitro and in vivo investigations of targeted chemotherapy with magnetic nanoparticles*. Journal of Magnetism and Magnetic Materials, 2005. 293(1): p.389-393.
 9. Ganguly, R., et al., *Analyzing ferrofluid transport for magnetic drug targeting*. Journal of Magnetism and Magnetic Materials, 2005. 289: p. 331-334.
 10. Ganguly, R., B. Zellmer, and I.K. Puri, *Field-induced self-assembled ferrofluid aggregation in pulsatile flow*. Physics of Fluids, 2005. 17(9): p. 097104-8.
 11. Sawada, T., H. Kikura, and T. Tanahashi, *Kinematic characteristics of magnetic fluid sloshing in a rectangular container subject to non-uniform magnetic fields*. Experiments in Fluids, 1999. 26(3): p. 215-221.
 12. Sudo, S., K. Ise, and S. Kamiyama, *Jet formation of magnetic fluid with vibration of an annular magnet*. Journal of Magnetism and Magnetic Materials, 2002. 252: p. 162-165.
 13. Willert, C.E. and M. Gharib, *Digital particle image velocimetry*. Experiments in Fluids, 1991. 10(4): p. 181-193.
 14. Westerweel, J., *Fundamentals of digital particle image velocimetry*. Measurement Science & Technology, 1997. 8(12): p. 1379-1392.
 15. Nguyen, N.T., et al., *The application of μ PIV technique in the study of magnetic flows in a micro-channel*. Journal of Magnetism and Magnetic Materials, 2005. 289: p. 396-398.
 16. Eckstein, A., J. Charonko, et al., *Phase correlation processing for DPIV measurements*. Experiments in Fluids, 2008.
 17. Chong, M.S., A.E. Perry, and B.J. Cantwell, *A general classification of three-dimensional flow fields*. Physics of Fluids A, 1990. 2, 765-777.
 18. Cucitore, R., M. Quadrio, et al., *On the effectiveness and limitations of local criteria for the identification of a vortex*. European Journal of Mechanics - B/Fluids, 1999. 18(2): 261-282.
 19. Berkooz, G., P. Holmes, and J.L. Lumley, *The Proper Orthogonal Decomposition in the Analysis of Turbulent Flows*. Annual Review of Fluid Mechanics, 1993. 25(1): p. 539-575.

20. Holmes, P., Lumley, J. L., and Berkooz, G., *Turbulence, coherent structures, dynamical systems and symmetry*. Cambridge: Cambridge University Press, 1996.

7 SPATIOTEMPORALLY-RESOLVED DYNAMICS OF DISPERSING FERROFLUID AGGREGATES

7.1 ABSTRACT

Ferrohydrodynamics research has been approached predominantly from either numerical or basic experimental techniques. To date, these experimental techniques have been limited to point measurements or shadowgraphs due to the opacity of the ferrofluids. As a result, the complete dynamics of ferrohydrodynamic flows have remained unexplored. In this work, Time Resolved Digital Particle Image Velocimetry (TRDPIV) is employed to fully resolve the dynamic interaction of magnetized ferrofluid aggregates with bulk nonmagnetic fluids over a range of flow conditions. This topic is hydrodynamically rich, where shearing between the aggregate and bulk flow develop into the Kelvin-Helmholtz instability. Ferrofluid aggregates are mixed with fluorescent particles in order to enable visualization of the internal flow structures of the aggregate and generate quantitative velocity measurements in both the bulk flow and aggregate.

The TRDPIV measurements are made in a 15 mm square channel where the flow fields associated with aggregate of ferrofluid retained by a 0.5 Tesla permanent magnet are measured as the ferrofluid disperses. The effects of both steady and pulsatile flows are quantified, as are the impact of varying the magnetic field gradients. In both steady and pulsatile flows, a recirculation region is observed within the ferrofluid, driven by the shear layer between the bulk flow and aggregate interface as well as magnetic forces drawing ferrofluid back to the aggregate. The interaction of the aggregate with the flow is also governed by the aggregate height relative to that of the test section. Higher, larger aggregates are less stable, and therefore, more likely to be dispersed by the bulk flow. As the aggregate diminishes in size, it is both more stable and is less subject to shearing forces from the flow. Flow pulsatility enriches the dynamics of the flow and generates complex flow structures resulting from interaction between the aggregate and bulk flow. This work is the first to explore the rich spatiotemporal behavior of dispersing ferrofluid aggregates interacting with steady and unsteady bulk flows.

7.2 INTRODUCTION

Ferrohydrodynamics is dedicated to the study of fluids that can be strongly magnetized in the presence of applied magnetic fields. These fluids are comprised of stably suspended superparamagnetic nanoparticles, which become highly magnetized under magnetic fields but return to their initially unmagnetized state once the field is removed. The research of magnetic fluids encompasses basic ferrofluid mechanics and composition to several different hydrodynamic instabilities [1,2,3]. The magnetizability of ferrofluids factors into fluidic instabilities that can be either controlled or accelerated when compared to non-susceptible fluids based on the orientation of the applied magnetic field. Many new technologies have been developed as a result of over 40 years of ferrohydrodynamics research such as ferrofluid-based dampers and seals [4], Magnetic Drug Targeting (MDT) [5] and other disease treatment methods [6].

Experiments studying ferrohydrodynamics have applied a limited range of techniques [7], while the usage of modern, optical-based techniques such as Digital Particle Image Velocimetry have been avoided in ferrohydrodynamics due to the opacity of the working fluid. In this work, we obtain Time Resolved DPIV (TRDPIV) measurements of the ferrofluid aggregate as it changes based on the incident bulk flow. The results presented herein reveal the rich spatiotemporal dynamics of ferrofluid aggregates that explores the influence of different parameters on their behavior including Reynolds number, flow unsteadiness, and magnetic field gradients. The results obtained from this experiment will be presented first in terms of the change in vorticity contours corresponding to the aggregate over time for steady flows, followed by pulsatile flows. A final section provides insight into the mechanism by which the aggregate evolves over time, examining the relationship between the shearing at the aggregate interface and the circulation of the vortex within the ferrofluid aggregate.

7.3 EXPERIMENTAL PROCEDURE

Herein, 10 nanometer-sized particles in suspension (EMG-705, Ferrotec, Inc) were mixed with 10 micron neutrally-buoyant flow tracers. Flow fields were acquired in steady and pulsatile water bulk flow conditions for Reynolds numbers of 200, 300, and 400. The flow was measured using planar TRDPIV (Time Resolved Digital Particle Image Velocimetry). A 532 nm wavelength Nd:YAG laser beam was expanded into a plane and aligned streamwise to the flow direction, coincident to the centerline of the 15 mm square cross-section channel, which had a length of 1 m. The data was obtained using a high speed IDT XS-5 digital camera sampling at 100 Hz using single laser pulses for flow tracer illumination. A schematic of these components is shown in Figure 7.1. Digital image frames were 1280 by 420 pixels, with a magnification of 36 microns per pixel. For each case, a total of 6000 frames were acquired, corresponding to 60 seconds of real-time sampling. The results presented herein represent an ongoing investigation by the authors of the DPIV technique to ferrohydrodynamics [8].

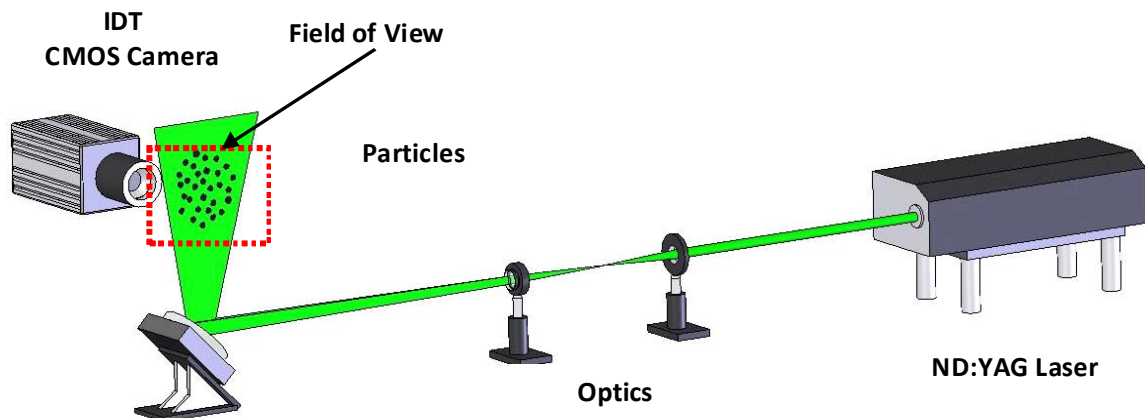


Figure 7.1. Schematic of the laser, optical setup, and digital camera used to acquire TRDPIV data.

Before the start of each case, two milliliters of ferrofluid was injected into the test section and accumulated by a permanent 0.5 Tesla magnet located 4 diameters downstream from the injection location. Ferrofluid was injected by means of a 90 degree needle aligned parallel to the length-wise test section wall and the streamwise direction of flow. Injection was controlled by a KD 230 syringe pump, with injection accurate to 1% of specified volume. The permanent magnet retaining the ferrofluid aggregate was oriented obliquely such that a vertex of its cubic profile was located nearest ferrofluid injected in the first second of the to the test section. This results in a high density of magnetic field lines with a nearly two-dimensional gradient profile. A schematic of the test section showing the relative locations of the test section, ferrofluid, and magnet is shown in Figure 7.2.

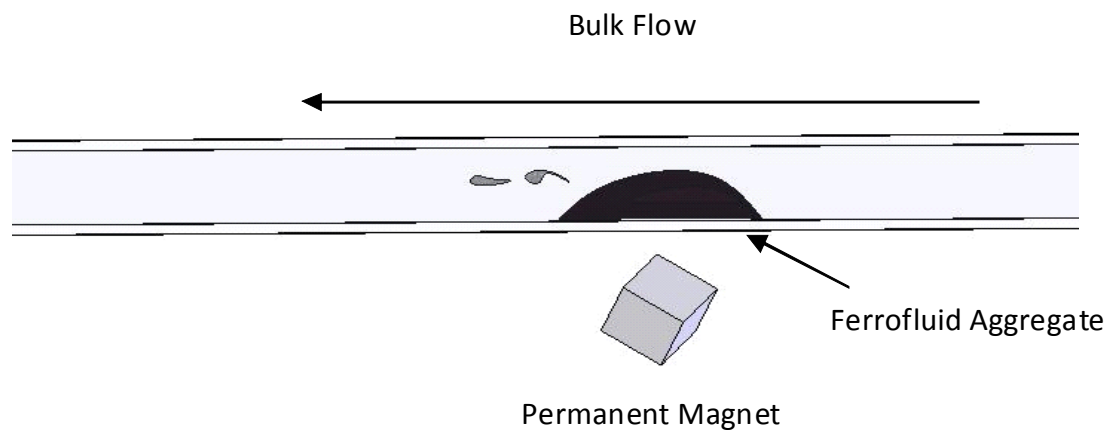


Figure 7.2. Schematic illustrating the relative location of the magnet and ferrofluid aggregate.

Data for a total of 18 cases were acquired in this experiment, where the effects of flow inertia, unsteadiness, and magnetic field gradients interact. The unsteady flows employed sinusoidal waveforms with the same mean flow rate as the corresponding steady flow case for each Reynolds number. The Reynolds number for each case is based upon the mean velocity as well as D_h . The effects of three different field gradients were explored as well for steady and pulsatile flows. The cases were selected based on a previously performed extensive shadowgraph examination of a wide range of parameters influencing the ferrohydrodynamics of

ferrofluid aggregates by the authors [9]. A full test matrix for all test cases collected in this experiment is shown in Table 7.1.

Table 7.1. Complete test matrix of all test cases for PIV experiment examining ferrohydrodynamics of ferrofluid aggregates across a parameter space.

Case	Reynolds Number	Steady/ Pulsatile	Maximum Field Strength (Tesla)
1	200	Steady	.075
2	200	Steady	0.15
3	200	Steady	0.375
4	200	Pulsatile	.075
5	200	Pulsatile	0.15
6	200	Pulsatile	0.375
7	300	Steady	.075
8	300	Steady	0.15
9	300	Steady	0.375
10	300	Pulsatile	.075
11	300	Pulsatile	0.15
12	300	Pulsatile	0.375
13	400	Steady	.075
14	400	Steady	0.15
15	400	Steady	0.375
16	400	Pulsatile	.075
17	400	Pulsatile	0.15
18	400	Pulsatile	0.375

7.4 RESULTS

Raw images obtained from TRDPIV were processed using two passes of the Robust Phase Correlation (RPC) method, which is particularly effective for processing frames with high background noise [10]. Two correlation passes of 64 by 64 and 32 by 32 pixel size windows with 8 by 8 pixel grid resolution were performed. Median and mean vector validation was performed on the correlated frames to eliminate erroneous measurements. An example illustrating the high background noise within the region of the aggregate, necessitating the use of the RPC, is shown in Figure 7.3. Even though the image in Figure 7.3 indicates high background noise in the aggregate, flow tracer particles can still be imaged. At higher concentrations of ferrofluid, the interaction with the bulk flow is amplified into the Kelvin-Helmholtz instability, shown in Figure 7.4, though the turbidity of the ferrofluid in this case does not permit visualization of flow tracers as evidenced by a vector field shown along with the raw frames.

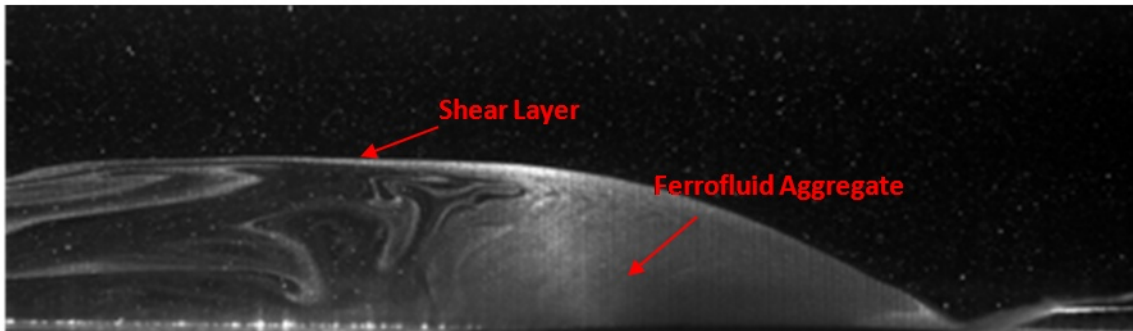


Figure 7.3. Raw PIV frame illustrating visible flow tracers in the bulk flow as well as the high noise region within the aggregate.

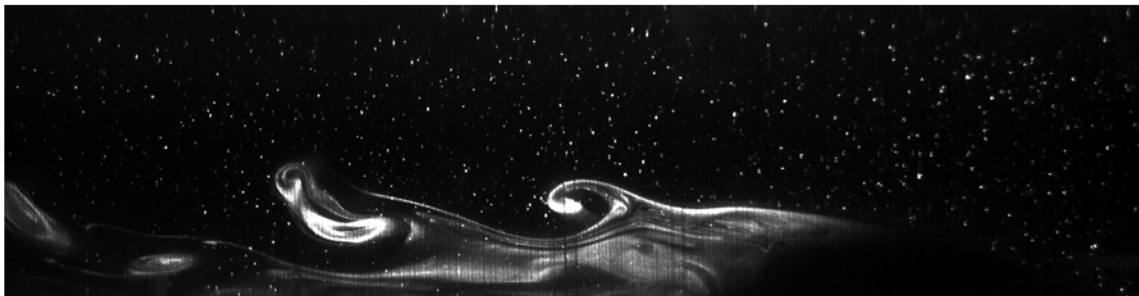


Figure 7.4. Vortex shedding of 2% concentration at a Reynolds number of 500 in steady flow and the development of the Kelvin-Helmholtz instability, with post-processed vector field illustrating limited measurement capacity within aggregate.

The ferrofluid concentration for all experiments presented is 0.5% by volume, compared with 2% by volume shown in Figure 7.4. The concentration of ferrofluid is a variable which will not be addressed herein, but has a direct impact on the development of the Kelvin-Helmholtz instability of the ferrofluid aggregate. 0.5% by volume concentration ferrofluid does not illustrate the Kelvin-Helmholtz instability at the same Reynolds number of 500 that is shown in Figure 7.4, but the shear layer convects away from the magnet, and only small-amplitude surface waves are visualized. This is a result of the lower ferrofluid concentration forming a lower effective viscosity aggregate compared to that of the higher concentration, since fewer nanoparticles are being magnetized and retained at the magnet.

Three time instants of post-processed vorticity contours overlaid with streamtraces for Reynolds numbers of 200, 300, and 400 for maximum magnetic field strengths of 0.375 Tesla are shown in Figure 7.5, Figure 7.6, and Figure 7.7. These flow fields represent time instants 1 second after the start of flow, and at 30 and 60 seconds after the start of data acquisition. In each set of flow fields, a local velocity increase in the bulk flow in the flow outside the aggregate corresponds to blockage of the flow. This blockage is confirmed by observing the paths of streamlines calculated from the incoming bulk flow, which trace the contour of the ferrofluid aggregate.

Figure 7.5 shows the development of aggregate fluid dynamics for three time instants for 1 second, 30, and 60 seconds for $Re_{av} = 200$. The x and y coordinates are normalized with the hydraulic diameter of the test section of 15 mm, with the (0,0) coordinates corresponding to the approximate location of the magnet tip located outside of the test section. The vorticity contour levels are normalized with both U_o and D_h for nondimensionalization purposes. For all cases, flow appears in the frames moving from right to left in the negative x direction. Edge detection of the aggregate interface with the bulk flow performed on images binarized using the MATLAB image processing toolbox illustrates the boundary of the aggregate, shown as a white line overlaid on the contours. The two white lines in Figure 7.5 indicate regions of diffuse ferrofluid in the outer layer, while the layer nearest the test section wall represents a dense, core region of ferrofluid.

Figure 7.5A shows the bulk flow partially impeded by the aggregate, which is indicated by the region of low velocity flow at the bottom of the test section. Within the aggregate, disruption of the streamline smoothness results from limited measurement capability within the aggregate. In Figure 7.5B, the aggregate has stretched downstream after 30 seconds of flow. A

clear vortex has developed at the interface between the bulk flow and the ferrofluid aggregate. The vortex results from the shearing from the bulk flow pushing the ferrofluid downstream and the restoring effects of the velocity deficit downstream of the aggregate and magnetic field gradients acting to circulate fluid back in the direction of the aggregate. This vortex also appears to be responsible for the stretching of the aggregate in the positive y direction, as the recirculation acts to draw ferrofluid away from the core aggregate. This phenomenon, appearing in many of the cases, will be explored in a later section. Aggregate stretching intensifies the apparent blockage of the test section as evidenced by the increased velocity between the aggregate and the top of the test section when compared to Figure 7.5A. The stretching of the aggregate interacting with the bulk flow and blockage intensification ultimately leads to further aggregate shearing downstream in Figure 7.5C. However, the aggregate remains stable and it is not significantly eroded during the 60 seconds data acquired for an average Reynolds number of 200 with B_{\max} of 0.375 Tesla. For lower magnetic field strengths at this Reynolds number, the aggregate does not exhibit the upward stretching of the aggregate as in Figure 7.5. Lower field strengths result in rapid smearing of the hemi-spherical shaped aggregate into a shear layer that extends far downstream and the aggregate washes away as time proceeds.

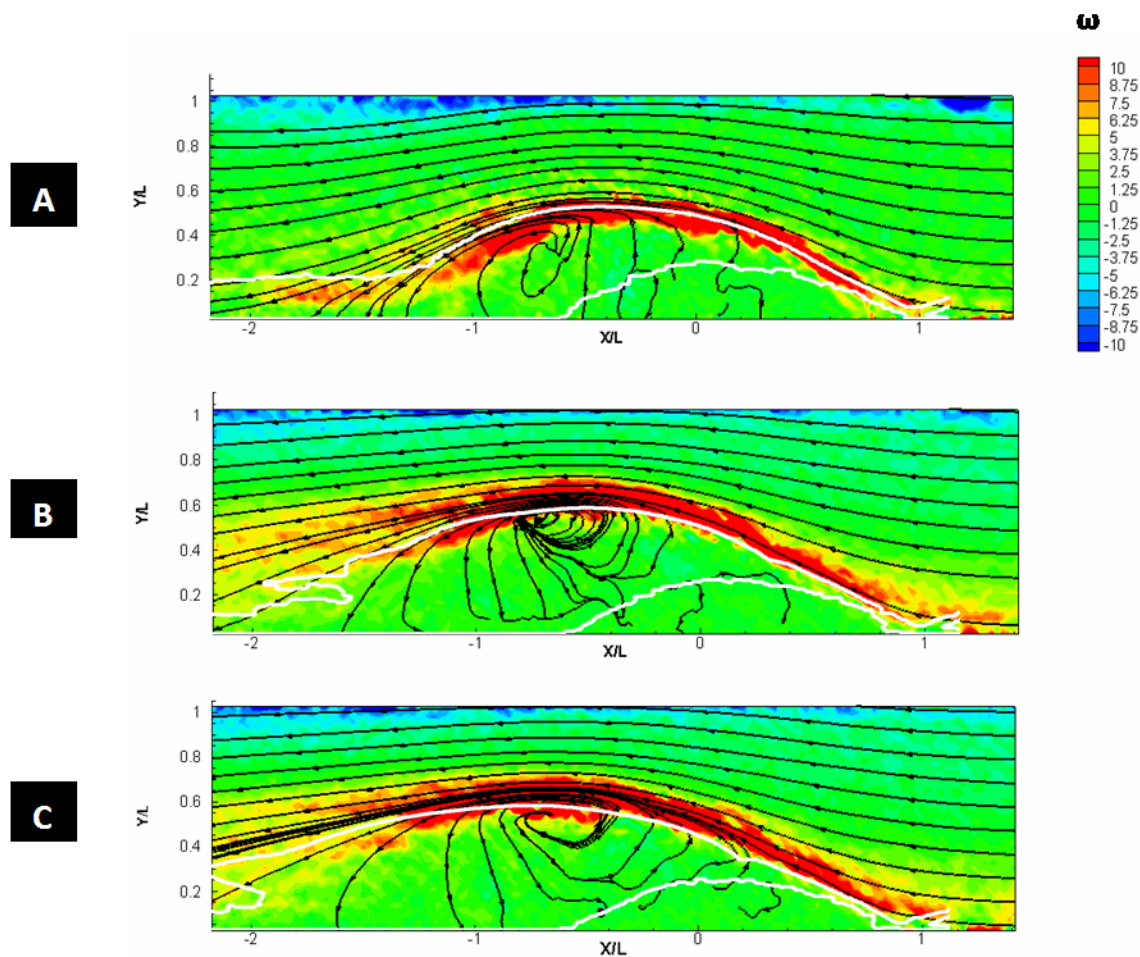


Figure 7.5. Instantaneous vorticity contours overlaid with streamlines for a Reynolds number of 200 at a maximum magnetic field strength of 0.375 Tesla; detected edges corresponding to aggregate interface with bulk flow overlaid onto contours.

When the Reynolds number is increased to 300 in Figure 7.6, significant aggregate decay is observed when compared to a Reynolds number of 200 in steady flow for the same B_{\max} . Once the bulk flow has reached its steady state in Figure 7.6A, a heightened velocity increase over the peak of the aggregate (outline shown in white) driven by higher bulk flow inertia causes the aggregate to stretch downstream, and the shear layer expands. The expansion of the aggregate shear layer also results in a reduction of aggregate size, which is observed in Figure 7.6C as the shear layer expansion results in more of the aggregate convected away from the region of high magnetic field strength. The reduction of the aggregate height results in lesser flow blockage and therefore, deceleration over the aggregate. Finally, we observe that two distinct regions of ferrofluid density are not detected for this Reynolds number, indicating that higher flow inertia

does not allow for the development and maintenance of core and diffuse regions of ferrofluid concentration.

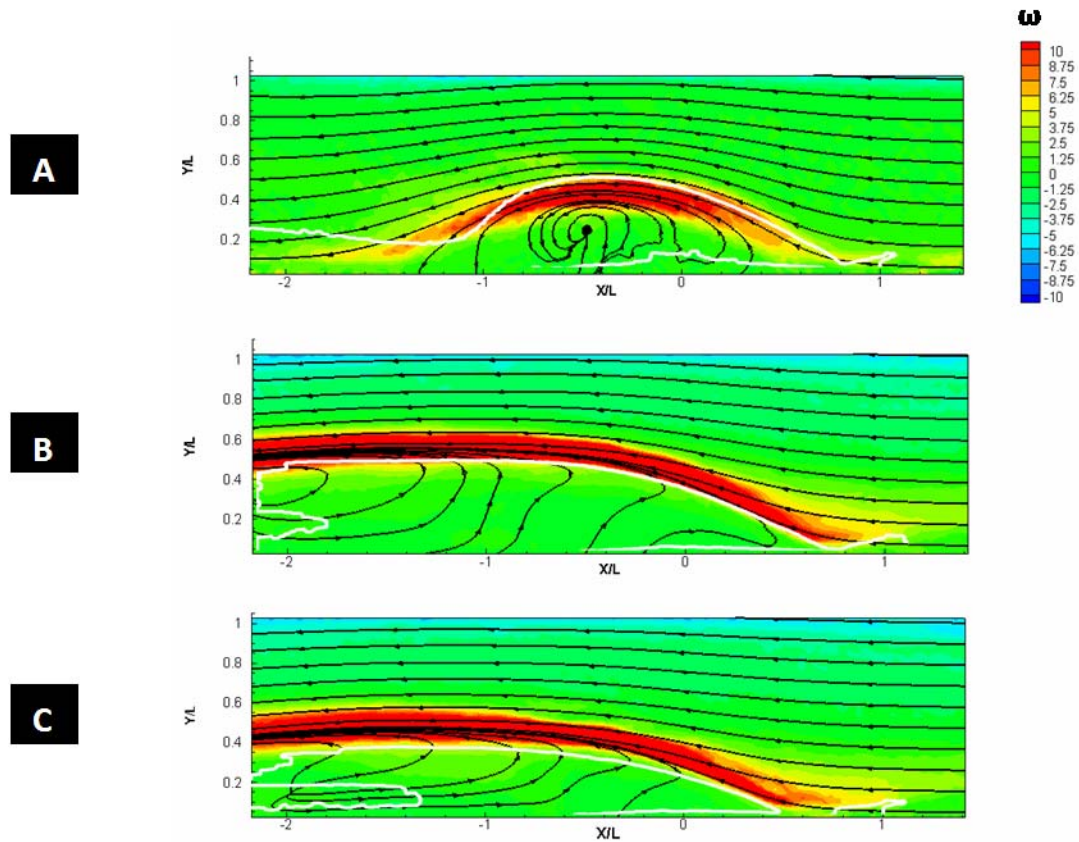


Figure 7.6. Instantaneous vorticity contours for a Reynolds number of 300 at a maximum magnetic field strength of 0.375 Tesla.

Finally, in Figure 7.7, three time instants for a steady flow at a Reynolds number of 400 is illustrated just after flow ramp up as well as after 30 and 60 seconds of incident bulk flow, also for B_{\max} of 0.375 Tesla. At this Reynolds number, the flow inertia is significantly stronger than magnetic forces, and therefore, aggregate erosion is rapid. Recirculation within the aggregate in Figure 7.7A is reduced to slight distortion of the streamlines in Figure 7.7B. At 60 seconds after flow startup, the aggregate is nearly completely decayed, and limited distortion of the streamlines occurs, as shown in Figure 7.7C.

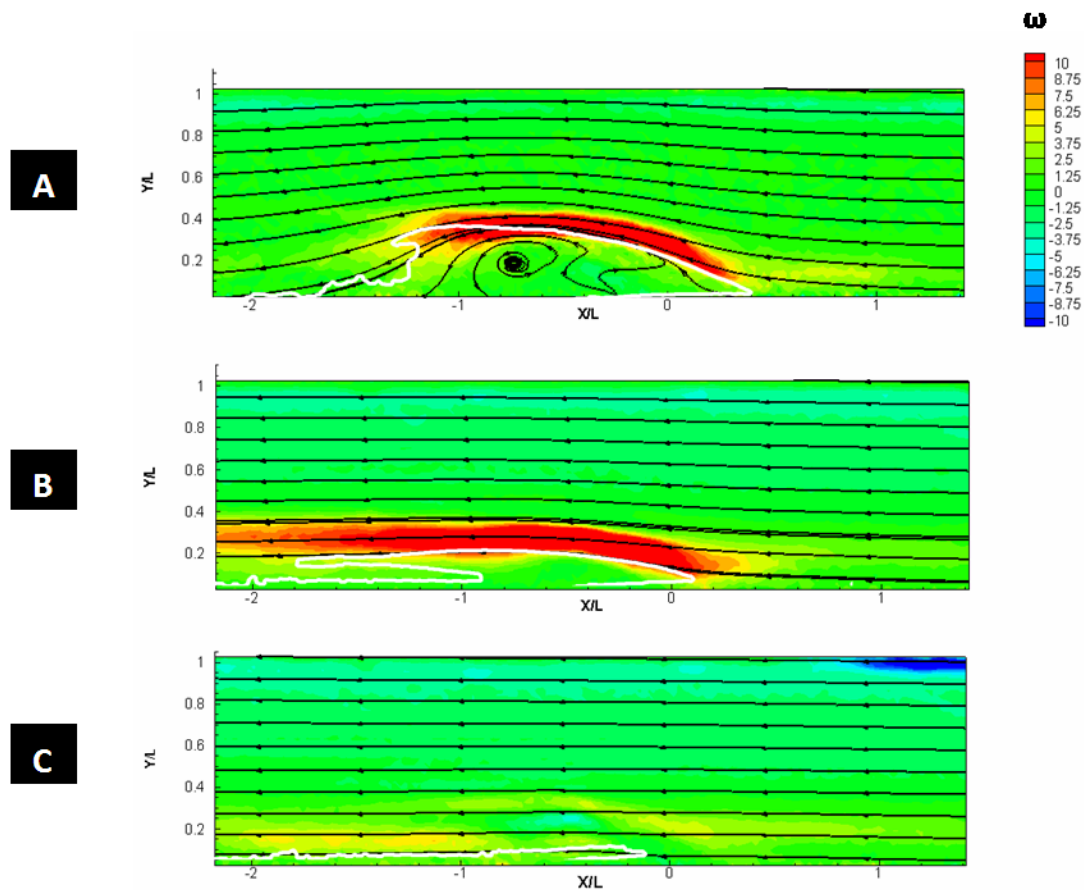


Figure 7.7. Instantaneous vorticity contours for a Reynolds number of 400 at a maximum magnetic field strength of 0.375 Tesla.

In pulsatile flow, the aggregate deforms dynamically based on the instantaneous flow rate. The pulsatility results in significant decay of the aggregate due to the high peak flow rate, and therefore, limited distortion and blockage of the flow occurs as the aggregate decays. The most dynamic and complex behavior of the aggregate at 0.5% concentration is observed for the highest magnetic field gradients, of 0.375 Tesla. Sequences demonstrating the effect of pulsatility for average Reynolds numbers of 200, 300, and 400 illustrate the principal dynamics of ferrofluid aggregates under the influence of pulsatile flow. Pulsatile flows in ferrofluid aggregates are primarily described by suction, roll up, and ejection of the ferrofluid aggregate in response to the instantaneous flow rate. Therefore, the vorticities and fluid structures will be examined for these stages for each Reynolds number.

At an average Reynolds number of 200, the pulsatile flow interacts with the ferrofluid aggregate to a degree that the bulk flow is significantly altered, but aggregate decay is

minimal. Three time instants of vorticity contours overlaid with streamtraces from this pulsatile flow are shown in Figure 7.8. During periods of low flows, in

Figure 7.8A, the aggregate region is encompassed by a suction vortex, top boundary of the vortex is the shear layer between the aggregate and bulk flow.

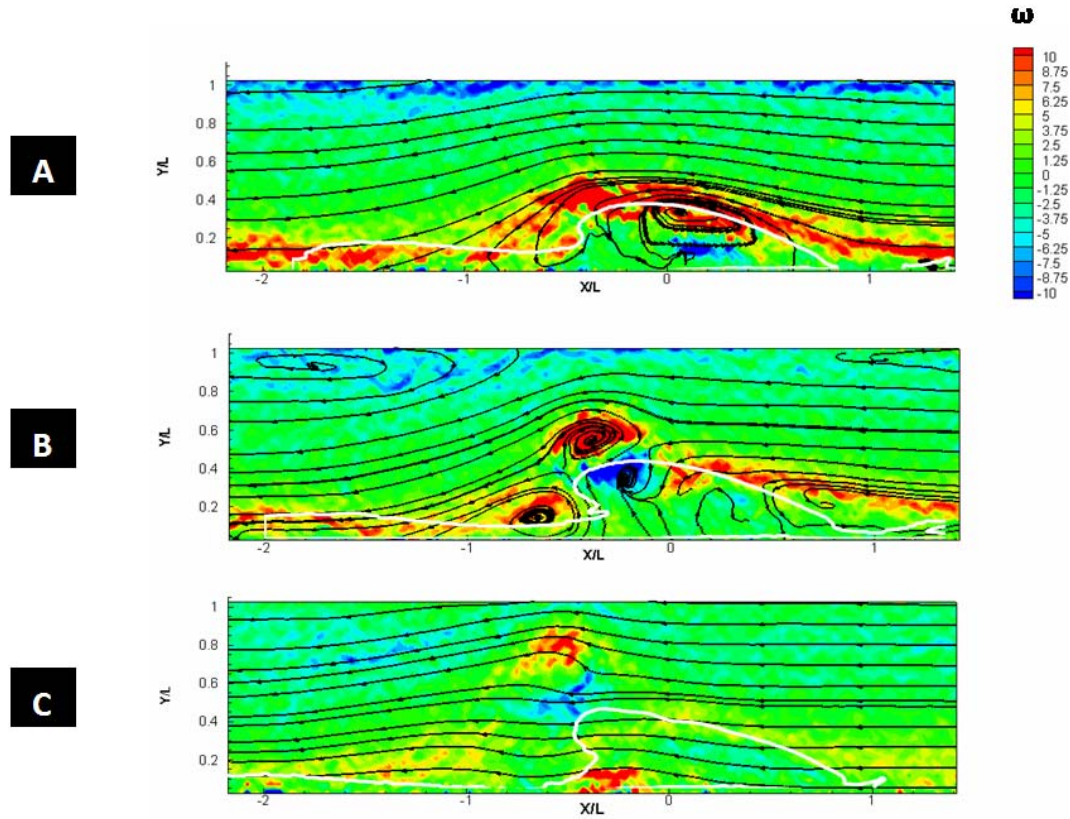


Figure 7.8. Instantaneous pulsatile flow velocity contours illustrating the aggregate behavior for a Reynolds number of 200 at 0.375 Tesla maximum field strength.

The rotation of the fluid within the ferrofluid aggregate is driven by the shear layer interacting with the magnetic body forces acting in the positive x direction. During the roll-up stage, occurring as flow ramps up from the low level at which the suction vortex forms, the aggregate reverses direction and begins to move in the negative x direction, resulting in the ejection of a vortex ring structure from the aggregate itself. As flow peaks in

Figure 7.8C, the aggregate stretches downstream along with the bulk flow, and some convects far downstream with the bulk flow, but the aggregate retains its structure and a clear shear layer is present.

As the Reynolds number is increased to an average of 300 in Figure 7.9, similar flow structures are apparent when compared to a Reynolds number of 200, although the increased peak inertia results in distinct differences in portions of the aggregate dynamics. The two sequences of pulsatility in

Figure 7.8 and Figure 7.9 are those just after flow has ramped up, so the two aggregate sizes are initially similar. However, in Figure 7.9A at low flow, the size of the aggregate in suction is smaller, as can be observed by comparing with

Figure 7.8A. During flow acceleration in Figure 7.9B, the roll up process is similar to that of the lower Reynolds number, but is accompanied by the formation of three additional vortices which are convected downstream as regions of high positive and negative vorticity as flow ramps up to peak levels in Figure 7.9C.

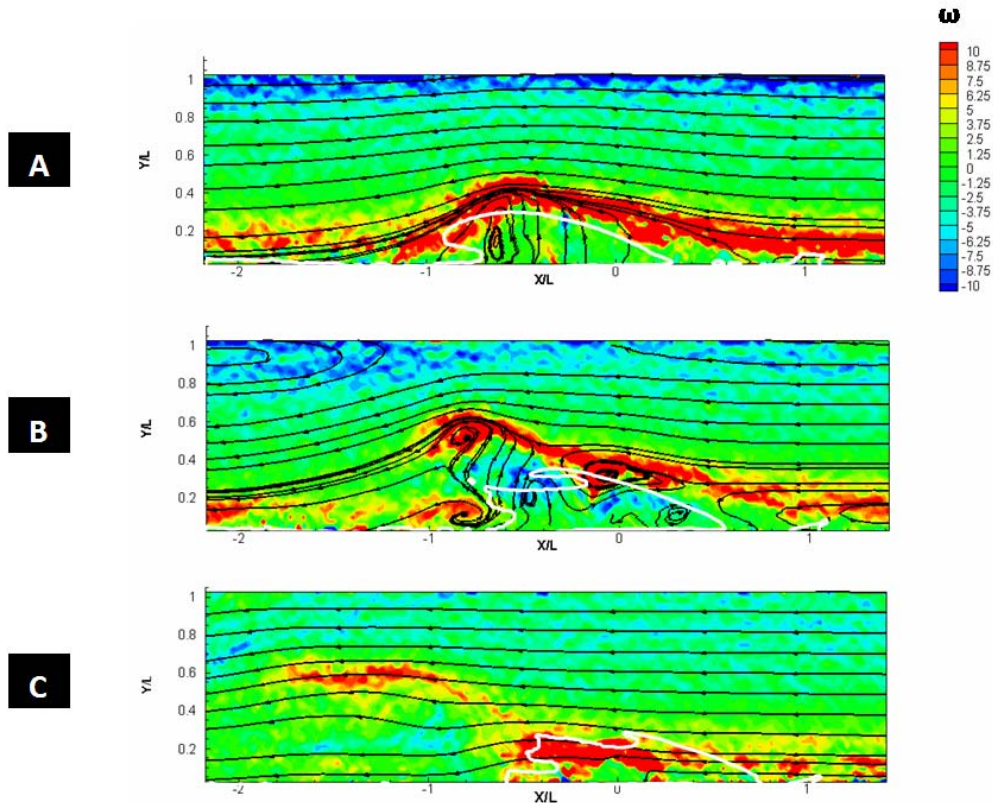


Figure 7.9. Instantaneous velocity contours for pulsatile flow with an average Reynolds number of 300 with a maximum field strength of 0.375 Tesla.

As the average Reynolds number is increased to 400, the peak flow rates significant aggregate shearing, and therefore, a relatively undeveloped suction vortex as shown in Figure 7.10A compared to the two lower Re_{av} for pulsatile flow at $B_{max} = 0.375$ Tesla. At moderate flows, flow structure definition in the roll up phase is well attenuated in Figure 7.10B. As with unsteady flows with average Reynolds numbers of 200 and 300, when the flow is at its peak in

Figure 7.10C, little streamtrace distortion occurs in the region of the aggregate as it is sheared downstream during peak flow. The aggregate for the average Reynolds number in pulsatile flow of 400 decays rapidly, as the high shearing of ferrofluid away from the magnet does not allow for the restoring magnetic body force to reform the aggregate in between periods of flow peaking as occurred for the two lower Re_{av} in pulsatile flows.

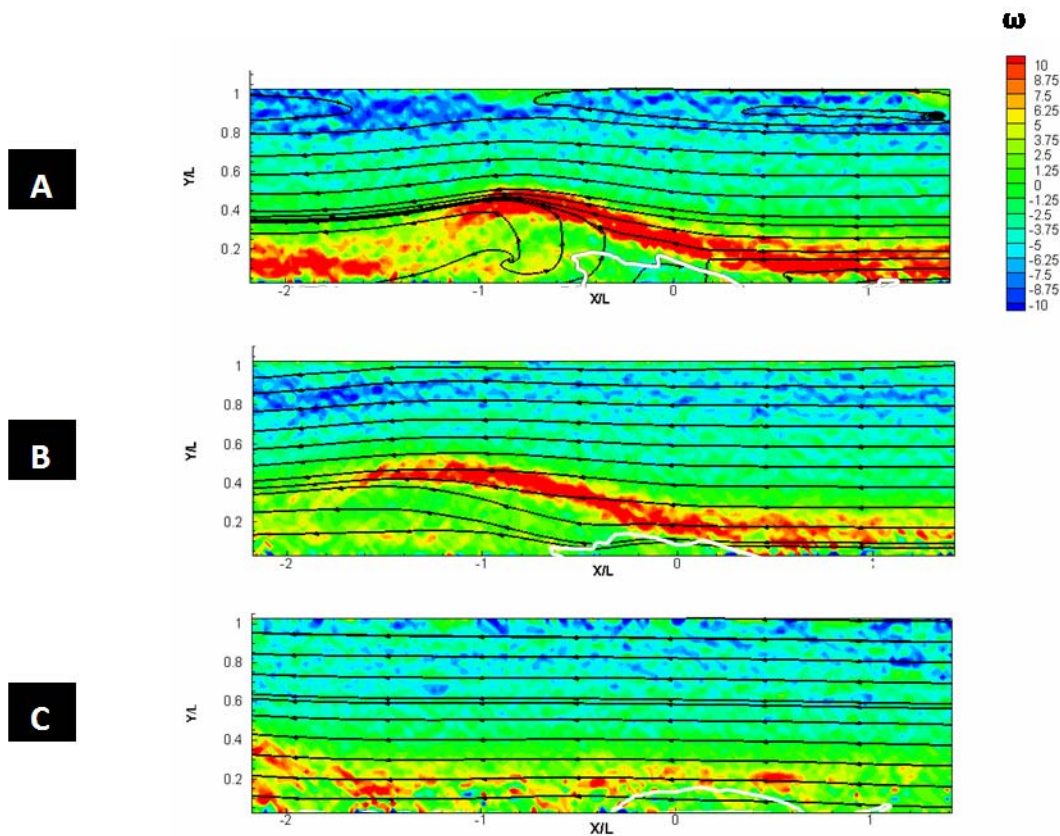


Figure 7.10. Instantaneous frames illustrating flow behavior for a pulsatile flow with an average Reynolds number of 400 with a maximum magnetic field of 0.375 Tesla.

Finally, the effect of magnetic field gradients on the ferrofluid-fluid system are addressed with an example of a pulsatile flow with average Reynolds number of 200. Frames corresponding to similar instantaneous flow rates are shown in Figure 7.11 for comparison with those shown in

Figure 7.8. The aggregate in Figure 7.11 is retained by maximum field gradients of 0.15 Tesla compared to the data presented thus far with $B_{\max} = 0.375$ Tesla. In this case, when flow reaches its minimum in Figure 7.11A, a large suction vortex forms that encompasses the aggregate, similar to the higher magnetic field strength. In Figure 7.11B, the roll up stage results in lower vorticity values in the region of the roll up vortices, corresponding to the lower magnetic field strength exerting less influence over the strength of the flow structures. Higher magnetic field gradients act to spin up vortices in the region of the ferrofluid aggregate, which will be addressed in the next section. Peak flows in Figure 7.11C similarly result in limited streamtrace distortion as the aggregate is convected downstream, and the overall aggregate size is diminished during this stage due to the lower field strength.

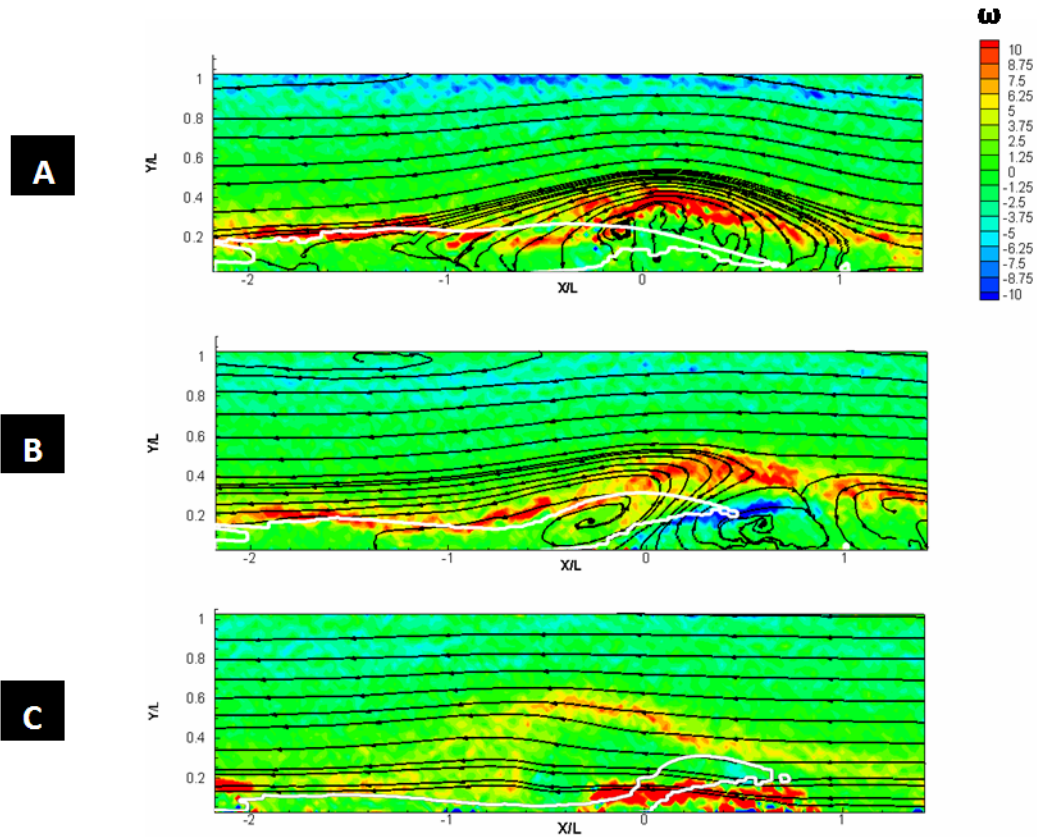


Figure 7.11. Instantaneous vorticity contours illustrating flow behavior for pulsatile flow an average Reynolds number of 200 with a maximum magnetic field of 0.15 Tesla.

The magnetic field effectively induces additional tensile forces on the ferrofluid aggregate as the field gradients are intensified. Therefore, the effective stiffening of the ferrofluid aggregate occurs. As a result, the ferrofluid-fluid interaction is modified in that the aggregate maintains a more significant structure, even as the flow peaks and ebbs. For the low magnetic field strength of 0.15 Tesla at the wall in a pulsatile bulk flow, the ferrofluid-fluid system interacts in a general suction, roll up, and ejection process as flow goes from its lowest level to its highest. The same process is visible even as the magnetic field is increased up to 0.375 Tesla at the wall. However, due to the increased effective viscosity of a ferrofluid that is more highly magnetized due to the increased field strength [11,12], the ferrofluid aggregate for 0.375 Tesla retains a clear structure throughout the pulsatile process.

7.5 DISCUSSION

In these results, the aggregate is observed to interact with the bulk flow as a quasi-solid obstruction in steady flow, and a dynamically stretching and contracting region that can behave as an obstacle based on the applied magnetic field strength. We now explore the mechanisms by which the ferrofluid aggregate interaction with the incident flow changes over time. Utilizing the detected edges in time from the raw frames, the mean velocity over the point of the maximum ferrofluid aggregate height was calculated. The mean velocity flowing directly over the maximum aggregate height acts to shear away the aggregate, and will henceforth be referred to as the shear velocity, U_s . The values of U_s plotted versus real time are shown for steady and pulsatile average Reynolds numbers of 300 in Figure 7.12 and Figure 7.13, respectively. The Reynolds number of 300 was selected for this detailed investigation due to the display of all fundamental mechanics of the ferrofluid aggregate under the different conditions investigated. Ratios of U_s to U_o are positive as, a nonzero aggregate size always presents some blockage to the flow. For steady flows, the increase in magnetic field strength is correlated with the increased height of the aggregate, and therefore, increased U_s . The height increases to a point where the shear stresses and magnetic forces interact, resulting in shedding of ferrofluid away from the aggregate, and therefore, a drop in shear velocity for B_{max} of 0.075 Tesla. As the magnetic field increases, the shear velocity increases as the magnetic field interacts with the vortex within the aggregate causing the aggregate to stretch orthogonal to the direction of the bulk flow. In pulsatile flow, the effect of the magnetic field is again manifested by different blockage based on the applied field, where the trend of increasing blockage follows the increasing magnetic field.

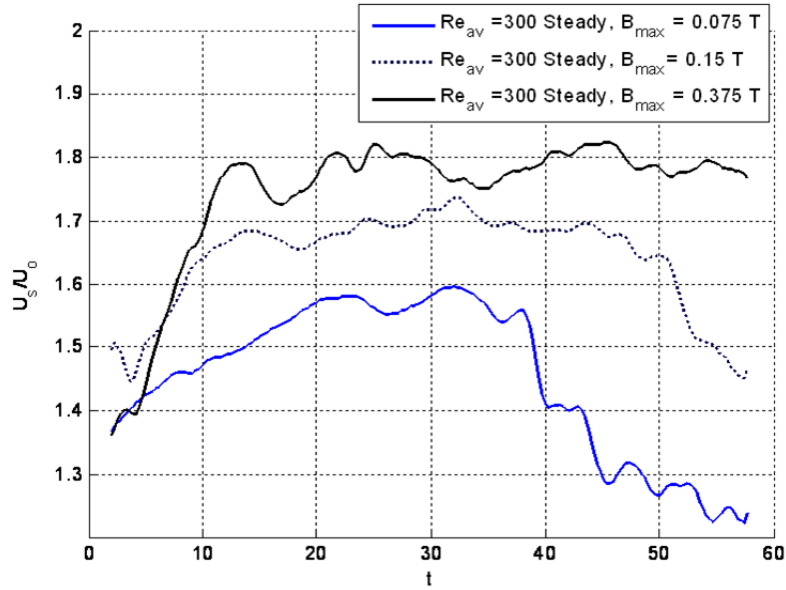


Figure 7.12. Shear velocity normalized with respect to the average freestream velocity for steady flows with a Reynolds number of 300.

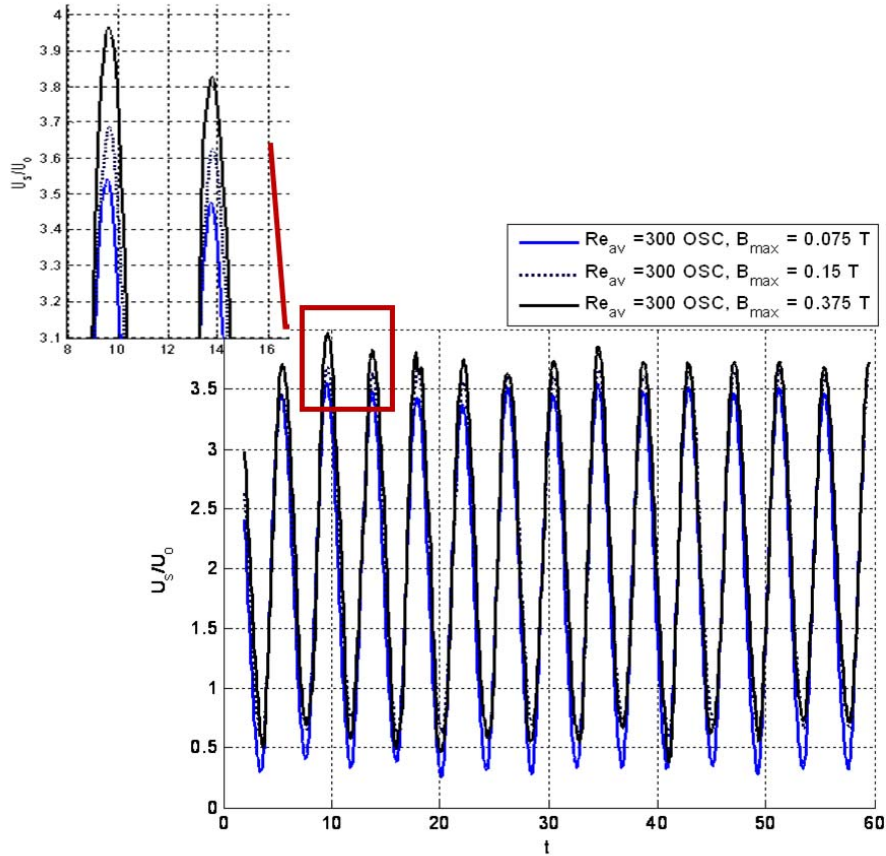


Figure 7.13. Shear velocity normalized with respect to the average freestream velocity for pulsatile flows with an average Reynolds number of 300.

To confirm the interaction of the vortex within the aggregate with aggregate stretching, the dynamics of the vortices within the flow fields were next examined. The circulation of the vortices was calculated by first detecting the vortices and their corresponding centers using the delta criterion [13,14], which is written as

$$\Delta = \left(\frac{1}{3}\right)Q^3 + \left(\frac{1}{2}\right)R^2 > 0 \quad 7.1$$

where positive Δ indicate complex eigenvalues and the location of a vortical region. The Q and R parameters are invariants of the velocity gradient tensor and are calculated by

$$Q = \frac{1}{2}(\|\Omega\|^2 + \|S\|^2) \quad 7.2$$

$$R = \text{Det}(U_{ij}) \quad 7.3$$

Vortices within each flow field were detected for all times. The circulation of the detected vortex or vortices was calculated by a line integral around the polygon that defines the vortex region. All detected vortices for the steady flows are in within the aggregate on the downstream edge of the shear later with respect to the magnet. The maximum circulation values are normalized by the kinematic viscosity of water. For steady flows, the low magnetic field results in a continual decrease in circulation as the aggregate develops an extended shear layer rapidly since the low field gradients do not retain a cohesive aggregate. Therefore, the aggregate height and corresponding shear velocity decays slowly while the circulation strength within the aggregate also decreases, shown in Figure 7.14. For higher magnetic field strengths, the aggregate retains better structure, and therefore the spin up of the vortex within the aggregate occurs corresponding to an increase in the circulation. For the highest B_z of 0.375 Tesla, the circulation peaks and decays slowly, correlating with U_s/U_o in Figure 7.12.

In contrast, for pulsatile flows, the circulation peaks and ebbs in time due to flow pulsatility as in Figure 7.15. As with steady flows, an increase in the normalized circulation peaks occur as the magnetic field gradients are increased from lowest to highest levels. As the aggregate for these cases does not experience significant decay over time, a fairly steady overall

RMS value of the peak circulation over time is obtained for each of the magnetic field strengths of interest.

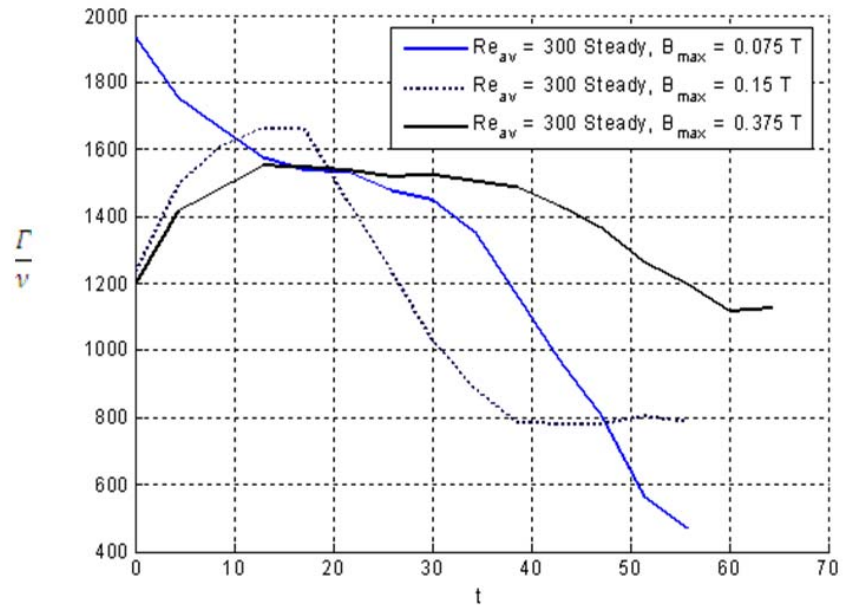


Figure 7.14. Normalized circulation versus time, t for three magnetic field strengths retaining an aggregate in steady bulk flow with a Reynolds number of 300.

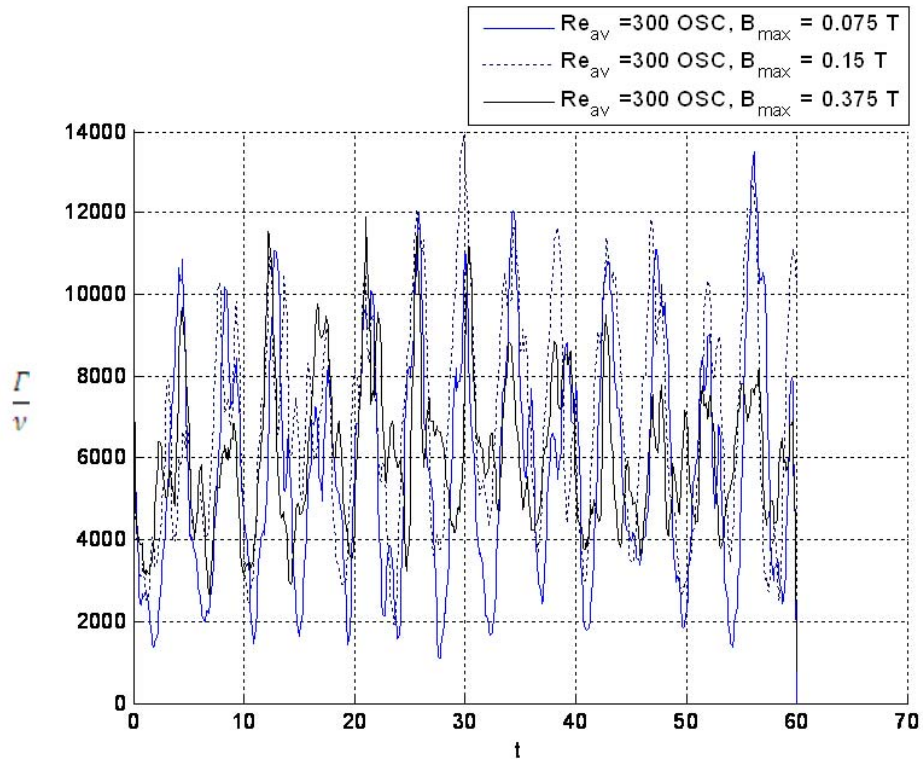


Figure 7.15. Normalized circulation versus time, t , for three magnetic field strengths retaining an aggregate in pulsatile bulk flow with Re_{av} of 300.

7.6 CONCLUSIONS

Herein, the dynamics of ferrofluid aggregates in steady and pulsatile flow are spatiotemporally resolved using TRDP-IV. Reynolds numbers ranging from 200 to 400 are explored for steady and sinusoid pulsatile bulk flows. Aggregates containing 0.5% concentration by volume ferrofluid were retained by a permanent 0.5 Tesla magnet with an incident bulk flow flowing past the aggregate acting counter to the magnetic forces, shearing the aggregate downstream. The magnetic field gradients were varied between 0.075 and 0.375 Tesla over the range of steady and pulsatile flows.

The results of this work indicate that ferrofluid aggregate behavior is codependent on both bulk flow and the magnetic field gradients. In steady flow for the same field gradients, the aggregate is observed to erode rapidly as the Reynolds number is increased, deforming from a hemispherical mass to a pronounced, thinning shear layer. The shear layer formed results in a slow fluid rotation within the aggregate, with a downstream vortex. The vortex assists the stretching of the aggregate out into an extended shear region, where it is eroded away due to weakened magnetic forces.

In pulsatile flow, the ferrofluid aggregate and bulk flow demonstrate strong coupling, where the aggregate deforms periodically based on the temporal variation of the bulk flow. During periods of high flow, the aggregate shears downstream, though a clear shear layer remains present. As flow decreases, the aggregate coalesces back towards the magnet. The coalescing ferrofluid creates a blockage to flow, and as flow decreases to its lowest level, fluid impinges onto the aggregate and rolls off as a pair of vortices. The interaction of the aggregate with the bulk flow decays as the aggregate decays as the interfacial shearing decreases. The magnetic field gradients have a strong effect on the behavior of the aggregate, and strengthened field gradients can enhance the instability of the shear flow between the ferrofluid and bulk flow. The relevant mechanism arises from the increased field gradients strengthening the vortex in the wake of the aggregate, causing the aggregate to lift up from the test section wall and therefore, the aggregate is more likely to be sheared downstream.

7.7 REFERENCES

1. Adrian, R.J., *Twenty years of particle image velocimetry*. Experiments in Fluids, 2005. 39(2): p. 159-169.
2. Abou, The Normal Field Instability in Ferrofluids: hexagon-square transition mechanism and wavenumber selection. Journal of Fluid Mechanics, 2000. 416: p. 217-237.
3. Perry, M.P. and T.B. Jones, *Interfacial parametric ferrohydrodynamics*. Journal of Applied Physics, 1975. 46(2): p. 756-760.
4. Raj, K. and R. Moskowitz, *A review of damping applications of ferrofluids*. Magnetics, IEEE Transactions on, 1980. 16(2): p. 358-363.
5. Lubbe, A.S., et al., Clinical Experiences with Magnetic Drug Targeting: A Phase I Study with 4'-Epidoxorubicin in 14 Patients with Advanced Solid Tumors. Cancer Research, 1996. 56(20): p. 4686-4693.
6. Brusentsov, N.A., et al., *Evaluation of ferromagnetic fluids and suspensions for the site-specific radiofrequency-induced hyperthermia of MX11 sarcoma cells in vitro*. Journal of Magnetism and Magnetic Materials, 2001. 225(1-2): p. 113-117.
7. Kikura, H., Y. Takeda, and T. Sawada, *Velocity profile measurements of magnetic fluid flow using ultrasonic Doppler method*. Journal of Magnetism and Magnetic Materials, 1999. 201(1-3): p. 276-280.
8. Williams, A.M, and P. Vlachos, August 2008, *Spatiotemporally-resolved Dynamics of Dispersing Ferrofluid Aggregates*. ASME Fluids Engineering Division Summer Meeting, Number FEDSM2008-55275.
9. Williams, A.M. and P. P. Vlachos, August 2008, *The Dynamics of Accumulating Ferrofluid Aggregates*. ASME Fluids Engineering Division Summer Meeting, Paper Number FEDSM2008-55101.
10. Eckstein, A., J. Charonko, et al. *Phase correlation processing for DPIV measurements*. Experiments in Fluids, 2008.
11. Patel, R., R. V. Upadhyay, et al. Viscosity measurements of a ferrofluid: comparison with various hydrodynamic equations. Journal of Colloid and Interface Science, 2003. 263(2): 661-664.
12. Yu Zubarev, A. and L. Yu Iskakova. *On the theory of rheological properties of magnetic suspensions*. Physica A: Statistical Mechanics and its Applications, 2007. 382(2): 378-388.
13. Chong, M.S., Perry, A.E., Cantwell, B.J., *A general classification of three-dimensional flow fields*. Physics of Fluids A, 1990. 2, 765-777.
14. Cucitore, R., M. Quadrio, et al. *On the effectiveness and limitations of local criteria for the identification of a vortex*. European Journal of Mechanics - B/Fluids, 1999. 18(2): 261-282.

8 CONCLUSIONS AND FUTURE WORK

Experimental measurement related to ferrohydrodynamics have been limited to basic shadowgraphy or other point measurements since the inception of ferrohydrodynamics study. In this work, we applied the conventional measurement technique of the focused shadowgraph and studied the development of the Kelvin-Helmholtz instability in ferrofluid aggregates for the first time. In addition, these studies are complimented by spatiotemporally-resolved measurements obtained using Time Resolved Particle Image Velocimetry, where we have provided results in a ferrohydrodynamics experiment for the first time. The TRDPIV results offer the measured velocity fields within the aggregate itself along with those within the bulk flow. One direct result obtained when comparing shadowgraph and TRDPIV results is in the effect of the magnetic field gradients. From the both the aggregate accumulation and dispersion experiments, increasing maximum magnetic field to 0.3 Tesla or above can result in the destabilization of the aggregate and its rapid wash away based on the parameters of this experimental work. However, changing the magnetic field also has consequences for the fluid structures themselves, which is an effect that was not quantified by the focused shadowgraph method.

The broader impacts of this research will extend not only to further investigations of ferrofluid dynamics, but also to relevant applications of ferrofluids. Experimentally, the development of the Kelvin-Helmholtz instability based on the conditions have provided the first results examining the destabilization of the ferrofluid aggregate based on increases in orthogonally-oriented magnetic fields. This research has also shown that TRDPIV can be successfully utilized in certain cases in ferrohydrodynamics, and could be translated to other experiments, where experimentally-resolved space-time measurements would complement the predominantly analytical and numerical studies that have been performed.

8.1 SUMMARY OF RESULTS

The behavior of the ferrofluid aggregate is driven by the parameters under which it is studied. Flow unsteadiness, Reynolds number, magnetic field gradients all have different but significant impacts on the behavior of the ferrofluid aggregate build up and retention at the magnet location. The development of the Kelvin-Helmholtz instability occurs for aggregates that have a large apparent size with a corresponding height near half of the D_h in Reynolds numbers above 400 in either steady or pulsatile flow. The K-H instability weakens as the aggregate washes away and is subjected to lowered shearing from the bulk flow. The Kelvin-Helmholtz rolls may disappear as the aggregate restabilizes as its size decreases and shear stresses and magnetic body forces balance.

In addition to these general observations about the nature of ferrofluid aggregates under different conditions, several specific conclusions generated from the compilation of this work are:

1. **Reynolds Number-based Regimes for Dispersing Aggregates:** For aggregates in dispersion, Reynolds number-based regimes describe the stability of such aggregates.
2. **Decreased organization of the aggregate interface as the Kelvin-Helmholtz instability develops and strengthens:** the POD dimension of the interface increases as a function of Reynolds number.
3. **Magnetic field gradients at low or high levels relative to the flow conditions negatively impact aggregate retention:** low magnetic field strengths of 0.225 Tesla or less result in minimal aggregate accumulation, while high magnetic field strengths result in aggregate destabilization and washaway
4. **$1/U_o^2$ dependence between the maximum captured aggregate height and the Reynolds number for top and bottom-injected accumulating aggregates.**
5. **The three-stage interaction of ferrofluid aggregates with pulsatile flows:** suction, roll up, and ejection of the ferrofluid aggregate occurs periodically with different values of the flow rate. The circulation strength of the vortices peaks as the flow

rate decreases to its lowest limit and the circulation and flow rate remain out of phase for all measured velocity fields.

6. **Ferrofluid aggregates in steady flow develop a shear layer that expands and then decays based on the circulation strength of the vortex that develops in their wake:** the shear layer develops with a vortex in the wake of the recirculation region that peaks, generating lift of the aggregate from the test section wall. This lifting can lead to the destabilization of the aggregate, and therefore, the circulation within the aggregate wake diminishes.
7. **Fluid-ferrofluid interaction intensifies for higher magnetic field strengths:** the effect is most defined during pulsatile flows. For highest magnetic field strengths, a vortex ring forms that rolls over the aggregate interface during the roll up stage of flow as a result of higher magnetization concurring with a higher effective viscosity. Lower magnetic field strengths result in flow structures that are contained largely to the immediate region of the aggregate during all stages of pulsatile flow.

For ferrofluids applied clinically in an application such as MDT, several ramifications result from these data. Counter-intuitively, continually increasing the magnetic field gradients that the aggregate is subjected to may act counterproductively to capture and retain those aggregates. Conversely, very low magnetic field gradients logically result in limited capture of the ferrofluid. These data have also shown how the Kelvin-Helmholtz instability can result even at arterially-relevant Reynolds numbers such as 400 in pulsatile flow. Moreover, the amount of aggregate accumulated and retained in the near-magnet region is highly dependent on how the ferrofluid aggregate is introduced into the flow.

8.2 FUTURE WORK AND RESEARCH DIRECTIONS

The dynamics of aggregates of ferrofluids is a topic from which many different research directions may be pursued, both from mechanics and applications perspectives. Mechanistically, the results presented from this research provide the basis for further investigations. As has been shown from the TRDPIV data, the behavior of the ferrofluid

aggregates varies widely based on the concentration of the ferrofluid in a water solution. Moreover, the dimensionless parameters utilized herein to describe the aggregate physics do not appear to capture the full range of motion for the aggregate mechanics. Therefore, towards developing a universal parameter or parameters describing the aggregate behavior, the exact relationship between the concentration of ferrofluid and aggregate retention and stability must be quantified. An additional direction that could be pursued towards the development of a more global description of the aggregate behavior would include a model force balance between the aggregate and the magnetic body force known as the Kelvin force, coupled along with the circulation effect that was observed in the TRDPIV data.

Although many non-linear stability formulations have been analytically developed, these models have not been compared to any experimental data. A next step in the research of the Kelvin-Helmholtz instability in ferrofluids would include comparisons of the shadowgraph data from the ferrofluid aggregate dispersion to these non-linear stability criteria to develop a comparison between experimental data and analytical results. Describing the stability of ferrofluid interfaces would provide a means to discern *a priori* whether the ferrofluid aggregate would remain stable.

Towards the translation of these results in applications, the MDT application requires a full characterization of the location of organs in the body as well as the engineering of magnetic field gradients to best target drug delivery into these regions. Although the behavior of ferrofluid aggregates has been characterized over a large range of conditions in the present work, medically, an additional set of experiments should be performed to correlate the retention of the ferrofluid with the effective absorption of the drug. This effort would combine both physics and biology to develop a full-circle view of how the degree of retention and stability of the ferrofluid in different parts of the body affect the delivery and efficacy of the drug. The efficacy of the drug would be tested by measuring the change in size of a tumor in a mammal model such as a mouse after the application and retention of MDT, while the retention of the drug could be roughly measured by means of an MRI [1]. In this way, both the physics of the Magnetic Drug Targeting process as well as the relevant biological impact on the nearby tissue would be addressed.

An effort to translate the initial studies presented in this dissertation to more clinically-relevant environments is underway. A ferroparticle-based study is currently being conducted in bulk flows with both physiologically-relevant flow rates and waveforms to determine the

particle trajectories as they are introduced into the bloodstream as well as the corresponding influence of the magnetic field. Results obtained from this research will extend the physical intuition of the MDT procedure in the hopes of developing a process that will prove consistently safe and effective.

8.3 ACKNOWLEDGMENTS

The National Science Foundation Graduate Research Fellowship and CAREER award are gratefully acknowledged for support of this research.

8.4 REFERENCES

-
1. Goodwin, S., et al., *Targeting and retention of magnetic targeted carriers (MTCs) enhancing intra-arterial chemotherapy*. *Journal of Magnetism and Magnetic Materials*, 1999. 194(1-3): p. 132-139.